UNIVERSIDADE DE LISBOA
FACULDADE DE CIÊNCIAS
DEPARTAMENTO DE ENGENHARIA GEOGRÁFICA, GEOFÍSICA E ENERGIA

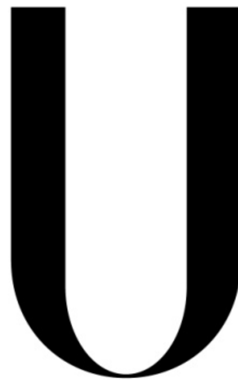

EMPIRICAL OPTIMIZATION AND IMPLEMENTATION OF A BORON EMITTER ON N-TYPE SILICON SOLAR CELLS USING A BBR_3 LIQUID SOURCE

RODRIGO AMARO E SILVA

Dissertação de Mestrado
Mestrado Integrado em Engenharia da Energia e do Ambiente

2014

UNIVERSIDADE DE LISBOA
FACULDADE DE CIÊNCIAS
DEPARTAMENTO DE ENGENHARIA GEOGRÁFICA, GEOFÍSICA E ENERGIA

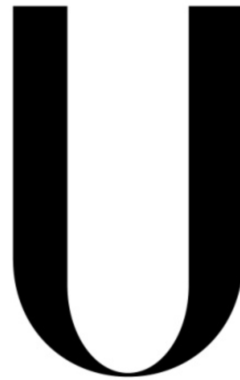

EMPIRICAL OPTIMIZATION AND IMPLEMENTATION OF BORON EMITTER ON N-TYPE SILICON SOLAR CELLS USING BBR_3 LIQUID SOURCE

Rodrigo Amaro e Silva

Trabalho realizado sob a supervisão de

Carlos del Cañizo Nadal (IES/ETSIT-UPM)

José Almeida Silva (IDL/FCUL)

Dissertação de Mestrado
Mestrado Integrado em Engenharia da Energia e do Ambiente

2014

Abstract

The present work focus on the study and optimization of a BBr_3 diffusion process for a p^+ layer formation on n-type Si wafers, as it is currently one of the main limitations for the implementation of cheap high-efficiency solar cells based on this material with a boron emitter.

A state of the art review is presented, covering the following topics: n-type silicon properties and its historical context; p^+ layer metallization and passivation; boron emitter properties and boron diffusion based on a BBr_3 liquid source.

Next, an experimental study of several diffusion process parameters and their impact on the resulting emitter is presented, being the parameters: BBr_3 bubbler temperature (and desirable stability); N_2 flow; N_2-BBr_3 flow; wafer spacing in the boat structure and predeposition step duration.

For each experiment it was verified the presence of a BRL while evaluating the diffusion homogeneity through a visual evaluation of the formed oxide and sheet resistance measurements. Afterwards, a selected single-wafer process was tested for batch process conversion, which then required a parameters optimization. The removal of the BRL through both chemical and thermal oxidation was also tested.

In conclusion, it was verified that a good control of the bubbler temperature is required and that it should be at least at 20 ºC in order to obtain an effective doping. All other parameters showed to have an impact in the formed emitter and resulting oxide, although no homogeneous doping nor oxide thickness were achieved. The formation of a homogeneous oxide is a crucial requirement as it can indicate a good homogeneity in both the doping and BRL formation, impeding an effective removal of this recombination-inducing layer. This was verified as both oxidation techniques tested resulted in only a partial removal of the BRL. It was also verified that a single-wafer process is not immediately convertible into a batch process as an ineffective doping was obtained, therefore requiring further parameter optimization.

Finally, future work lines are suggested in order to go on with the present work.

Keywords: n-type Si; p^+ layer; BBr_3 liquid source; BSG; BRL

Resumo

O presente trabalho aborda o estudo e optimização de um processo de difusão com fonte líquida de BBr_3 para a formação de uma camada p^+ em substrato de silício de tipo-n, sendo este passo uma das maiores limitações actuais para a implementação de células solares de alta eficiência de custo acessível baseadas neste material e com emissor de boro.

Uma revisão do estado da arte é apresentada, com os seguintes tópicos: propriedades do silício de tipo-n e seu contexto histórico; metalização e passivação de camadas p^+; propriedades de um emissor de boro e difusão de boro baseada numa fonte líquida de BBr_3.

De seguida, um estudo experimental de diversos parâmetros do processo de difusão e o seu impacto no emissor obtido, sendo os parâmetros: temperatura do borbulhador de BBr_3 (e desejável estabilidade); fluxo de $N_{2;}$ fluxo de N2-BBr_3; espacamento entre bolachas na estrutura de suporte e a duração da etapa de pré-depósito.

Para cada experência procurou-se verificar a presença de uma capa rica em boro (BRL) e avaliar a homogeneidade da difusão através de uma avaliação visual do óxido formado e medidas de resistividade de capa. Posteriormente, um processo de difusão em que apenas era dopada uma bolacha foi testado para dopar diversas bolachas num só processo, tendo depois exigido uma optimização dos parâmetros de difusão. A remoção da BRL foi testada através de uma oxidação química e de uma oxidação térmica.

Concluindo, verificou-se que um bom controlo da temperatura do borbulhador é um requisito e que esta deveria estar a pelo menos 20 ºC de forma a se obter uma dopagem eficaz. Todos os outros parâmetros mostraram ter impacto no emissor obtido e no óxido formado apesar de não se ter obtido nenhuma dopagem nem óxido que fossem homogéneos. Obter um óxido homogéneo é um requesito crucial já que pode indicar tanto uma dopagem como a formação de uma BRL também homogéneas, permitindo uma remoção eficaz da camada que induz recombinação tendo sido verificado que para os óxidos heterogéneos obtidos, tanto a oxidação química como térmica apenas resultaram numa remoção parcial da BRL. Verificou-se ainda que um processo de difusão estudado para uma única bolacha não é imediatamente conversível para dopar várias bolachas num só processo já que uma dopagem ineficaz foi obtida e portanto requerindo uma optimização de parâmetros adicional.

Finalmente, são ainda sugeridas linhas de trabalho futuro de forma a dar sequência ao presente trabalho.

Palavras-chave: Si tipo-n; camada p^+; fonte líquida de BBr_3; BSG; BRL

Table of Contents

1. Introduction ... 17
2. Motivation ... 18
3. State of the Art ... 19
   3.1. N-type Silicon ... 19
   3.2. P^+ layers metallization ... 20
   3.3. Surface passivation for boron emitters ... 21
   3.4. Boron emitter gettering ... 26
   3.5. Comparison between a boron p^+ region and a classical Al one ... 30
   3.6. Boron emitter fabrication with BBr_3 as a liquid source ... 34
   3.7. BRL Characteristics ... 38
4. Materials and methods ... 48
   4.1. Open-tube furnace and flow meters ... 48
   4.2. Chemical solutions ... 54
   4.3. Wafer characteristics ... 55
   4.4. Wafer preprocessing ... 55
   4.5. Wafer post-processing ... 55
5. Experimental results ... 56
   5.1. Desirable BBr_3 bubbler temperature range ... 56
   5.2. Bubbler Temperature Sensitivity ... 58
   5.3. BBr3-N_2 Gas Flow ... 62
   5.4. Nitrogen Flow ... 64
   5.5. Wafer spacing in the wafer support structure during the doping process ... 68
   5.6. Predeposition Time ... 71
   5.7. Batch Process Homogeneity ... 74
   5.8. Overdoped Barriers Removal ... 78
   5.9. Batch Process Optimization ... 80
   5.10. Predeposition + Thermal Dry Oxidation Process ... 84
   5.11. Predeposition + Chemical Oxidation Process ... 87
   5.12. Oxide Thickness Visual Assessment Method Validation ... 88

6. Conclusions and Future Work Lines 89
7. Attachments 92
7.1. Attachment 1: Color Char for Thermally Grown SiO2 92
8. Bibliography 94

List of Figures

Figure 1 - Schematic of a bowing Si solar cell due to the backside metal contact 31
Figure 2 - Bifacial front junction solar cells with opposite substrate doping schematic 31
Figure 3 - PV module with bifacial cells and diffuse back reflector 32
Figure 4 - Interconnection of p-type solar cells in a standard module (top) and of p- and n-type cells in a pn-module (bottom).. 32
Figure 5 - Scheme of alternate interconnection of p- and n-type solar cells in a 2×3 pn-module 32
Figure 6 - BBr_3 diffusion setup coupled to a tube furnace 34
Figure 7 - Schematics of a BRL formation: (a) B_2O_3 layer already formed and doping the substrate, (b) the boron atoms start to "pile-up" at the interface forming the BRL, (c) the BSG is removed by HF dip 36
Figure 8 - Micrograph of the two-phase layer system 20 μm from the wafer top of the sample, showing a 300 nm BSG and a 90 nm BRL... 39
Figure 9 - HREM images obtained from a symmetric NAO/SiNx passivated boron emitter (SiN_x-NAO-p^+-n-p^+-NAO-SiN_x) structure: (c) with BRL, (d) with BRL removed 40
Figure 10 - BSG distribution on a 156x156 mm^2 wafer after diffusion with 200% and 50% (right) relative BBr_3 flow.. 42
Figure 11 - Scheme of the used setup, consisting in an open tube furnace and its gas channels/sources and a liquid BBr_3 source 48
Figure 12 - Scheme of a ellipsometry process.. 51
Figure 13 - Scheme of four-point probe measurement 52
Figure 14 - Scheme of four-point probe measurement for sheet resistance of an emitter...... 54
Figure 15 - Oxide coloration after a doping process with a bubbler temperature of 20ºC..... 57
Figure 16 - Oxide coloration after each doping process. For the first two, a) and b), $T_{bubbler}$=25 ºC while for the third, c), $T_{bubbler}$=26 ºC. 59
Figure 17 - Doped wafer after an HF dip. It is visible the presence of an hydrophobic behavior in the central region, while the borders are hydrophilic... 60
Figure 18 - Resulting oxide coloration pattern for the 0.08 slm BBr3-N_2 gas flow process. 62
Figure 19 - Doped wafer after an HF dip. The presence of a completely hydrophobic surface is visible 63
Figure 20 - Obtained oxide coloration after each doping process. The N_2 flows are 3.53, 5.92 and 8.82 slm respectively 65

Figure 21 - Doped wafer after an HF dip. The presence of hydrophilic behavior in the center and lower regions is visible, while the borders are hydrophobic. 66
Figure 22 - Oxide coloration after each doping process. The wafer spacings are 4.0, 6.5 and 9.0 mm respectively 68
Figure 23 - Oxide coloration after each doping process. The predeposition duration is 15 and 30 min respectively. 71
Figure 24 - Reference single-wafer process, with a N_2 flow of 8.82 slm identical to Figure 20 c) 74
Figure 25 - Oxide coloration, on the side turned to the gas inlet,. 75
Figure 26 - Oxide coloration, on the side turned to the furnace exit 76
Figure 27 - Oxide coloration after the doping process. A overdoped and undoped barriers are used, respectively 78
Figure 28 - Oxide coloration for the reference batch process 80
Figure 29 - Oxide coloration with higher spacing and undoped barriers 81
Figure 30 - Oxide coloration with higher bubbler temperature and lower N_2 flux 81
Figure 31 - Surface coloration after the doping process and an etch-back 87

List of Graphs

Graph 1 - Surface charge density passivating effect for n-type and p-type emitters (R_{sheet} ~140 Ω/□) passivated with a thermal SiO_2 22

Graph 2 - Solar cell measured and simulated IQE curves for a solar cell with and without an applied high density of negative charges 23

Graph 3 - Simulated SRV for boron emitters passivated with SiO2 (for different charge densities), SiNx and a-Si/SiNx and a phosphorus emitter passivated with SiO2 as a function of dopant density 24

Graph 4 - Implied V_{OC} of a sample with a boron emitter as a function of the R_{sheet} passivated with SiN films for different annealing times 24

Graph 5 - Relationship between surface passivation, represented by the emitter J_{0e} and Si-N bond density for boron-diffused emitters 25

Graph 7 - Fe concentration remaining in bulk Si after annealing at 600 ºC for different periods as a function of initial Fe concentration 27

Graph 8 - Fe gettering model in p^+ samples having low-level Fe contamination 27

Graph 9 - Depth profiles of Fe concentration in p^+ and no p^+ samples annealed at 600 ºC for 20 minutes after low-level contamination at 850 ºC 27

Graph 10 - Simulated J_{0e} as a function of SRV for a boron emitter with two different doping levels, with and without Fe contamination 29

Graph 11 - Internal quantum efficiency and reflectance of a PERC cell (blue) and a reference cell (red) 33

Graph 12 - Reflectivity measurements in wafers with Al BSF fired at different temperatures 33

Graph 13 - R_{sheet} deviation reduction (from 21% to 10%, left to right) by adding water vapor during the drive-in step 35

Graph 14 - Rsheet (left) and BRL thickness (right) in terms of the deposition step duration for different processes 37

Graph 15 - Carrier lifetime as a function of BRL layer thickness 38

Graph 16 - BRL and BSG thickness assessed through SEM and optical measurement methods 40

Graph 17 - Measured depth profile of boron concentration for different BBr_3 flow 41

Graph 18 - R_{sheet} distribution on a 156×156 mm^2 wafer after diffusion with 100% (left) and 25% (right) relative BBr_3 flow 42

Graph 19 - Dependence of R_{sheet} on t_G at 800 ºC, 900 ºC and 1100 ºC for a B_2H_6-O_2 gas system [52] 44
Graph 20 - Overall BSG/BRL layer thickness, on silicon wafer surface as a function of position, where the reference diffusion took 30 mins, the diffusion 1a 10 mins and the diffusion 1b 60 mins [47] 45
Graph 21 - Line scan of the bulk carrier lifetime and doping mapping for a reference diffusion (left) and another diffusion with a longer duration (right) [47] 45
Graph 22 - R_{sheet} distribution on a 156 x 156 mm^2 wafer measured by four-point probe method for different diffusion temperatures 46
Graph 23 - Depth profile of boron concentration measured for different diffusion temperatures 46
Graph 24 - Measured diffusion profiles of boron emitters with and without BRL 47
Graph 25 - BBr_3 pickup rates at different bubbler temperatures 50
Graph 26 - Oxide thickness profiles, measured in a vertical line that crosses the wafer center 59
Graph 27 - R_{sheet} measured along a vertical line that crosses the wafer center. 60
Graph 28 - R_{sheet} along a vertical line that crosses the wafer center for two doping processes where the BBr_3-N_2 is varied 63
Graph 29 - Visually assessed oxide thickness profiles along a vertical line that crosses the wafer center for different N_2 flows 65
Graph 30 - R_{sheet} measured along a vertical line that crosses the wafer center for the three doping processes where the N_2 flow is varied. 66
Graph 31 - Visually assessed oxide thickness profiles along a vertical line that crosses the wafer center for different wafer spacings 69
Graph 32 - Measured R_{sheet} along a vertical line that crosses the wafer center for three doping processes where the wafer spacing is varied 69
Graph 33 - Visually assessed oxide thickness profiles along a vertical line that crosses the wafer center for different predeposition times. 72
Graph 34 - R_{sheet} measured along a vertical line that crosses the wafer center for two doping processes analyzed 72
Graph 35 - R_{sheet} measured along a vertical line that crosses the wafer center for the defined single-wafer reference process 75
Graph 36 - R_{sheet} measured at each wafer's center 76

Graph 37 - R_{sheet} measured along a vertical line that crosses the wafer center for the two doping processes analyzed.. 79
Graph 38 - R_{sheet} measured at each wafer's center for the three tested processes................... 82
Graph 39 -R_{sheet} measured along a vertical line that crosses the wafer's center for three wafers doped in the optimized batch process 82
Graph 40 - R_{sheet} measured along a vertical line that crosses the wafer center for different doping processes tested.. 85
Graph 41 - Comparison between BSG thicknesses visually assessed and measured with spectroscopic ellipsometry.. 88

List of Tables

Table 1 - Flow ranges for the used flow meters 49
Table 2 - Silicon wafers properties 55
Table 3 - Doping process conditions, varying only the bubbler temperature 56
Table 4 - R_{sheet} measurements done in three regions of the wafers, for a process with 4 ºC of bubbler temperature and another with 20 ºC 57
Table 5 - Doping processes conditions. 58
Table 6 - Process conditions, where only the BBr3-N2 flow is varied 62
Table 7 - Doping process conditions, where only the N2 flow was varied 64
Table 8 - Doping process conditions, where only the wafer spacing was varied 68
Table 9 - Doping process conditions 71
Table 10 - Doping process conditions of the single-wafer process selected to be tested in batch conditions 74
Table 11 - Doping process conditions, for the processes under test 78
Table 12 - Doping processing conditions, where an homogeneous batch process was sought 80
Table 13 - Doping process conditions for different processes tested. 84
Table 14 - Doping process conditions 87

List of Symbols and Acronyms

Symbol	Meaning
Al	Aluminum
Ag	Silver
Al_2O_3	Aluminum Oxide
B_2O_3	Boron Trioxide
BBr_3	Boron Tribromide
Br_2	Bromine
BRL	Boron-rich Layer
BSF	Back-Surface Field
BSG	Boron-Silicate Glass
CH_3CO_2H	Glacial Acetic Acid
Cz	Czochralski
Fe	Iron
FZ	Float Zone
H_2Odi	Deionized Water
HF	Hydrofluoric Acid
HNO_3	Nitric Acid
HREM	High-resolution Electron Microscopy
J_{0e}	Emitter saturation current
K	Extinction Coefficient
LID	Lightn-Induced Degradation
m_{BBr3}	Boron Tribromide pickup rate
MV	Molar volume
MW	Molecular Weight
N	Refraction Index
ρ	Resistivity
$P_{bubbler}$	Pressure at the bubbler
P_{vap}	Vapor pressure
P_2O_5	Phosphorus Pentoxide
$POCl_3$	Phosphoryl Trichloride
PV	Photovoltaic
mc	Multicrystalline
MV	Molar Volume

MWPCD	Microwave Photoconductance Decay
N_2	Nitrogen
NAO	Nitric Acid Oxidation
O_2	Oxygen
R_{sheet}	Sheet resistance
Slm	Standard Liter per Minute
Si	Silicon
SiO_2	Silicon Dioxide
SiN_x	Silicon Nitrate
SEM	Scanning Electron Microscope
SRV	Surface Recombination Velocity
SWOT	Strengths-Weaknesses-Opportunities & Threats
$T_{bubbler}$	Bubbler’s temperature
W	Wafer Thickness

1. Introduction

The present work presents the study of the fabrication process of boron emitters in n-type Silicon, a research that can have an impact in either p-type material Back-Surface Field (BSF) or even high-efficiency n-type bifacial solar cell concepts.

After presenting the motivation for this work in the second chapter, the information obtained after an extensive bibliographic review is presented in the third chapter. First, the historical context of n-type Silicon (Si) solar cells is approached, and its advantages and challenges when compared with p-type Si solar cells, are also mentioned. Then, boron doping is compared with the aluminum (Al) one (the standard for p-type cells' BSF). Afterwards Boron Tribromide (BBr_3) liquid source doping method is studied and the following topics are approached: description of the doping process, formation and characterization of what is designated as a Boron-Rich Layer (BRL) which is characteristic of heavy boron doping processes, and the passivation and gettering techniques related to this type of emitter.

The fourth chapter represents the experimental component of the present work. The equipments and techniques used for both the doping process and for the characterization of the doped wafers are presented, followed by the properties of the Si wafers used as substrates and the applied predoping treatment processes. Next, the obtained results are presented in a structure where for each experiment the implemented process is explained, the comparison of the color of the wafers' surface after the doping process with the Silicon Dioxide (SiO_2) color chart, the thickness of the deposited layer is estimated. Further, to inspect the presence of a BRL, after removing the superficial Boron Silicate Glass (BSG), the wafers' surface behavior when in contact with water was analyzed. The sheet resistance (R_{sheet}) measurements are also presented. All results obtained are thoroughly analyzed and discussed.

Finally, the conclusions from the present work and future topics of study are presented.

2. Motivation

Until recently, the generation of electricity using PV solar energy has presented a remarkable growth, mainly due to the improvement of the PV modules efficiency and, simultaneously, the reduction of their production costs.

A field of investigation that has been getting some notice in recent years is the fabrication of solar cells based on n-type Si with a boron emitter using a BBr_3 liquid source. This material possesses several properties that are quite advantageous for the production of cheap high-efficiency solar cells such as: higher tolerance to the contamination that is inherent, and unavoidable, in the industrial context which results in considerably high bulk lifetimes; compatible with the use of thinner substrates, a key factor for the cells' cost reduction, without any bowing or cracking problems; based in processes and equipments that are already present in the current industry; allows an almost immediate application of interesting concepts such as bifacial solar cells or alternate cell type connection.

However, this type of solar cells presents several challenges such as: significant bottom-to-top doping variation that occurs in the fabrication of n-type ingots; lack of a low-cost and industrially applicable passivation technique for boron emitters; need to modify the now-light receiving p^+ layer metallization, as in p-type cells this layer is fully covered by an opaque aluminum metallic contact.

Nevertheless, one of the main limitations is the inexistence of an affordable BBr_3 doping process that allows an homogeneous and controlled level of doping and an effective removal of the emitters' characteristic BRL, which is known to induce high recombination. Therefore, the purpose of the present work is the study and optimization of a BBr_3 doping process using n-type Si as the substrate material.

3. State of the Art

3.1. N-type Silicon

According to Gangopadhyay et al. [1], n-type Si material shows an excellent tolerance to the metal impurities commonly present in Si, which potentially results in higher charge carrier lifetimes and can even enable the use of feedstock of lower quality. In an industrial context, this material also shows a higher tolerance to introduced defects, which up to a certain degree are unavoidable. Also considering an industrial context, Cotter et al. [2] mention that not only the fabrication cost of n-type wafers is not significantly higher than standard p-type ones but also that the whole production chain from wafer to module manufacturing and the photovoltaic (PV) system strategies should be able to integrate n-type solar cells.

Gangopadhyay et al. [1] also presented a very interesting SWOT (Strengths-Weaknesses-Opportunities, & Threats) analysis for n-type crystalline Si, where the authors concluded that this material was particularly interesting for the high-efficiency solar cell production, having the potential to surpass other Si technologies in terms of cost-benefit.

Additionally, a phenomenon designated as Light-Induced Degradation (LID), studied for example by Schmidt et al. [3] and Sopori et al. [4] is responsible for degrading p-type Si solar cells performance after light exposure. Schmidt mentions that for high-efficiency solar cells in a laboratory context a 10% relative efficiency degradation has been observed while for an industrial context the loss was around 3-7%. Since it is believed that this phenomenon results from the formation of boron-oxygen complexes in the material, and a strong correlation between LID intensity and the concentration of these two elements has been reported by Glunz et al.[5], n-type Si seems to be immune, or at least, much more tolerant to this phenomenon.

Even though n-type Si had an early appearance in the PV context, as it was the substrate used for the first Si solar cell [6], until recently the great majority of Si solar cell producers use p-type semiconductor material as solar cell substrate. According to Mihailetchi et al. [7], the n-type Si solar cell processing, despite its advantages, was not sufficiently mature to be implemented industrially, mainly due to the absence of an industrial low-cost technique for the passivation of boron emitters.

Another possible explanation for the predominance of p-type Si is that electrons have a higher mobility compared to holes (which are the minority carriers for p and n-type Si, respectively), by a factor of about 3, which should lead to a higher bulk lifetime [2]. However, according to Gangopadhyay et al. [1], this is an oversimplified analysis since n-type Si has other advantages that can balance and even overcome the mobility issue.

On a different perspective, the most probable reason for this underdevelopment is historical as in the early days of commercial Si solar cell space applications dominated the market.

When Smith et al. [8] examined both n and p-type solar cells performance when irradiated with extraterrestrial radiation it was observed that even though the n-type material initially performed better, its performance degraded faster than the p-type material having a worse "end-of-life" productivity. This observation contributed to make p-type solar cells the main topic for PV energy research, helping to create and develop the foundations of the Si solar cells industry know-how.

Nowadays the terrestrial applications represent the large majority of the Si solar cell market, so the impact of high-energy radiation is not an issue anymore. Therefore, as the n-type material is once again considered an interesting option, to be used as solar cell substrate the main challenges regarding the industrial deployment of this type of solar cells, according to Cotter et al. [2] and Gangopadhyay et al. [1] are the relatively large segregation of phosphorus that leads variations in doping during n-type Si crystal growth and in terms of the boron emitter formation technology and the associated metallization technology.

When the substrate material is directionally-solidified, such as for Czochralski (Cz), Floatzone (FZ) or multicrystalline (mc) Si, the segregation coefficient of the dopant leads to a spatial variation in the doping level across the solidification direction. According to MacDonald, D. [9], for p-type Si a factor of 3 is typically found for the doping density variation from bottom to top of the ingot, which is considered tolerable in an industrial context. However, for the n-type material this variation reaches a factor of 10 and can significantly reduce the ingot production yield. To tackle this problem, solar cell designs that are tolerant to considerable resistivity variations and processes as melt-replenishment and dopant engineering are mentioned as possible solutions.

3.2. P^+ layers metallization

Another important aspect for boron emitters implementation is the metallization step. When talking about the metal contacts in a solar cell there are typical parameters such as: the contact resistivity between the contact and the emitter, the line resistance of the contacts (which influences the series resistance of the solar cell), the aspect ratio and the shadow factor. All these parameters are to be minimized, through the structure of the contacts, the dimensions of the fingers and busbar and the metal composition, as they imply either the blocking of light that would be absorbed by the cell or the energy dissipated by the metal or in the metal/semiconductor interface.

Al is the standard metal used with p^+ layers as it makes a good ohmic contact with highly p-doped Si. However, this metal is not such a good electric conductor. For p-type monofacial structures this setback is compensated by applying a metallic layer that fully covers the cell surface, reducing the contacts resistance. Nevertheless, this is not applicable for n-type Si where the p^+ layer is where the sunlight penetrates the cell.

Therefore, the alternative would be to use local Al contacts which makes its low conductivity an issue to be dealt with. One solution is the use of mixed Al/silver (Ag) pastes for screen-printing contacts, where there has to be a trade-off between the good ohmic contact of Al and the good electric conductivity of Ag depending on the quantity of each metal [10].

Silva et al. [11] studied a different metallization method which, even though not quite adequate for an industrial context, is based in an interesting concept denominated as "two-layer" contact, where an Ag/Al (mostly Al) paste is overlaid by a electrochemically deposited Ag layer paste. This way, the contact resistance and the metal conductivity can be optimized almost independently. An important conclusion regarding the mixed paste was that although the same grid was used for both frontal (Al/Ag) and back (Ag) contact, significantly wider fingers were obtained in the front contact (around 190 μm) when compared with the back one (around 110 μm). Also, the front contact by itself showed non-homogeneous fingers width (between 140 and 200 μm), being both situations due to the change in the paste's viscosity resulting from the Al/Ag mix.

In respect to the back contact, the same grid structure as for p-type solar cell is used as Ag is quite a good conductor and, at the same time, too expensive to cover the whole surface. Consequently, the bowing problem mentioned previously (when Al and boron BSF's are compared) is non-existent.

Edler, A. et al. [12] show experimentally that for n-type bifacial solar cells that the main cause for V_{OC} loss is the contacting of the boron emitter with the Ag/Al metal paste and that a possible solution is the use of selective emitters where thick emitters are formed under the contacts and thin ones under the remaining, and passivated, area.

3.3. Surface passivation for boron emitters

Surface passivation is a crucial step in solar cell design and fabrication, since the application of a passivation layer over the solar cell surface has the ability to greatly reduce the SRV of the defect-rich zones which, are a crucial limiting factor in the efficiency of solar cells [13].

Reduction the SRV can be achieved by the combination of a chemical and field effect passivation[13]. While the chemical passivation is related to the reduction of the dangling bonds in the cell's surface and the bulk (when an hydrogenated SiN_x is used, the passivation provided by the H atoms present in this layer and that diffuse into the bulk), materials like SiO_2, Silicon Nitride (SiN_x) and Aluminium Oxide (Al_2O_3) possess a built-in fixed charge density that, depending on the charge signal and the surface's doping type, can repel the minority carriers from the surface (similarly to the a BSF). Both SiO_2 and SiN_x have positive fixed charges while Al_2O_3 has negative fixed charges.

In standard n-type emitters the most frequent passivation layers used are SiN_x or a stack of SiO_2-SiN_x. The first material not only creates a good field-effect passivation, due to the high density (higher than for SiO_2) of positive fixed charges, but can also be an H source and

work as an anti-reflection (AR) layer. Nevertheless, as SiO_2 offers a better chemical passivation, in high efficiency solar cells, a stack of these two materials is used in order to obtain a compromise between chemical/field effect passivation and AR properties.

Regarding boron emitter's passivation, studies reported by Libal et al. [14] and Benick et al. [15] mention that these two materials do not perform so well in passivation of boron emitters, pointing out the positive fixed charges in both dielectric materials and the boron segregation in the case of SiO_2 as the probable causes. The first study even reported that the presence of a SiN_x layer lead to an average 12 mV implied V_{OC} decrease, which indicates a higher SRV, when compared to a non-passivated surface.

After these observations, studies started to point out Al_2O_3 as a good option for boron emitters surface passivation due to its negative fixed charges. Hoex et al. [16] measured J_{0e} values below 10 $fA.cm^{-2}$ on highly doped p-type c-Si surfaces of non-metalized samples while Benick et al. [15] obtained V_{OC} values up to 703.6 mV and an efficiency of 23.2%. Moreover, Benick et al. [15] showed that such a layer could lead to an increase of more than 40 mV of implied V_{OC} (Graph 1) and up to a 3% absolute increase in efficiency, verifying through Internal Quantum Efficiency (IQE) measurements, that this gain was respective to the front-side boron emitter region, as the improvement was only observed for low wavelength photons (Graph 2).

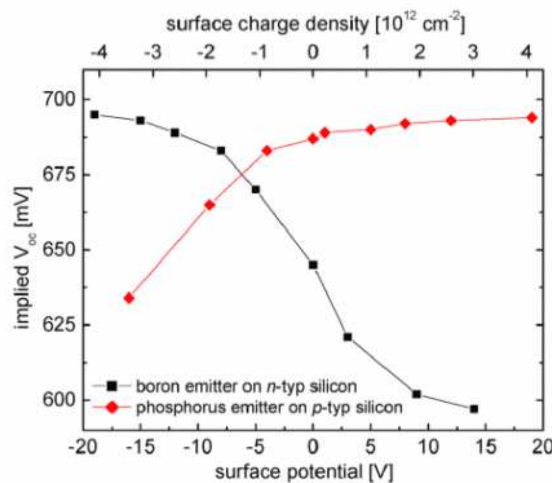

Graph 1 - Surface charge density passivating effect for n-type and p-type emitters (R_{sheet} ~140 Ω/□) passivated with a thermal SiO_2 [15]

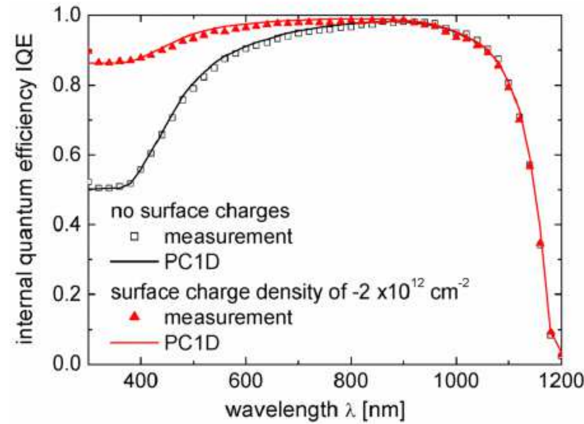

Graph 2 - Solar cell measured and simulated IQE curves for a solar cell with and without an applied high density of negative charges [15]

As an alternative, a local overcompensation with P is proposed by Benick et al. [17], where the inversion of the surface doping from *p*-type to *n*-type allows the use of standard technologies, resulting in a J_{0e} of 40 $fA.cm^{-2}$ on SiO_2 passivated samples. As mentioned previously, according to Phang et al. [18] this option can also lead to an enhanced gettering of the solar cell.

An interesting study was reported by Altermatt et al. [19] where it was verified through simulations the ineffectiveness of the SiN_x for boron emitters passivation and the weaker passivation quality of SiO_2 when compared with phosphorus emitters (Graph 3). This study excluded the fixed charge explanation for the insufficient passivation, as different charge densities were simulated and it was verified that for emitters with dopant densities of at least 10^{18} cm^{-3} the SRV was hardly affected by this parameter. For the authors, a more reasonable explanation would be that the recombination sites at the Si-SiO_2 interface have capture cross-sections that are more "harmful" for electrons than for holes.

This reasoning was, in a way, verified by Chen et al. [20] as the authors showed that if a post-deposition low temperature (450 ºC) thermal step was applied to a SiN_x layer, this material would perform and adequate passivation for boron emitters with sufficiently high R_{sheet} and that the longer the annealing step the better was the passivation (Graph 4).

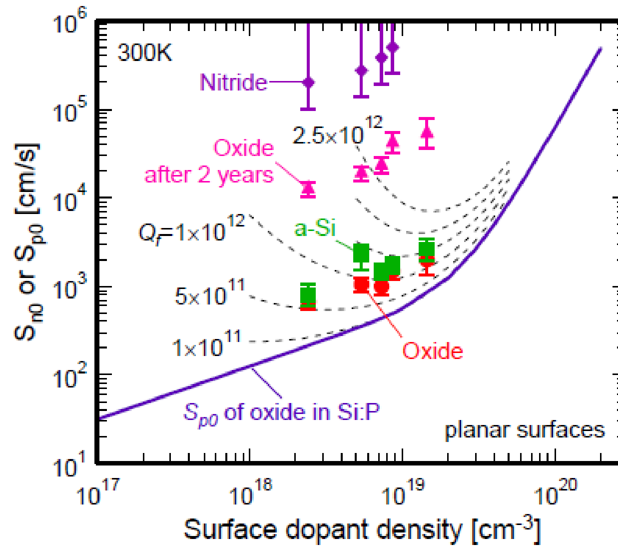

Graph 3 - Simulated SRV for boron emitters passivated with SiO2 (for different charge densities), SiNx and a-Si/SiNx and a phosphorus emitter passivated with SiO2 as a function of dopant density [19]

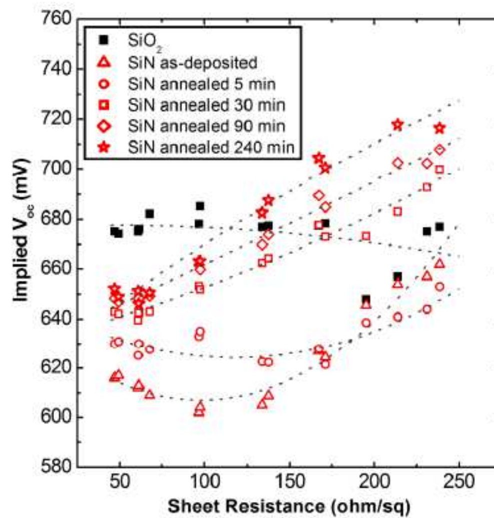

Graph 4 - Implied V_{OC} of a sample with a boron emitter as a function of the R_{sheet} passivated with SiN films for different annealing times [20]

In a later study, Chen et al. [21] re-stated the importance of the firing step (Graph 5) and also pointed out that the SiN_x film composition was an important parameter to be considered in order to optimize the boron emitter's surface passivation.

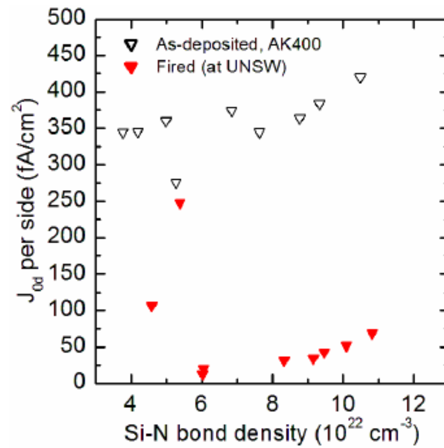

Graph 5 - Relationship between surface passivation, represented by the emitter J_{0e} and Si-N bond density for boron-diffused emitters [21]

Mihailetchi et al. [7] proposed a chemical passivation technique based in a stack composed by an ultra-thin chemical SiO_2 and a SiN_x layer as an alternative to thermal oxidation, which resulted in a J_0 of 23 fA.cm^{-2}. The technique's simplicity, effectiveness, cost-benefit and its scalability to large scale production were considered its main advantages. Ryu et al. [22] presented a chemical SiO_2 passivation, preceded by a chemical etch of the BRL that lead to a 100 fA.cm^{-2} J_{0e}.

More recently, Duttagupta et al. [23] proposed a PECVD low temperature grown SiO_x-SiN_y stack optimized for highly doped boron emitters that resulted not only in a good AR performance (only 2% effective reflection at the front surface) but also a J_{0e} of 25 fA.cm^{-2}. It is interesting to note that this value is quite close to the 15 fA.cm^{-2} obtained with Al_2O_3 passivation (Graph 6), a material that although passivates best, due to its negative charges and therefore good field effect passivation, would require the acquisition of new equipments for most of the industry. The authors obtained the J_{0e} values by fitting measurements of the Auger-corrected inverse effective lifetime as function of the injection level.

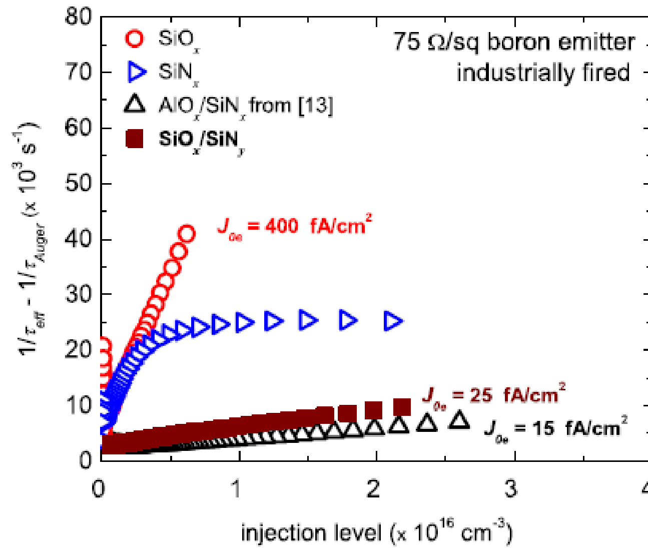

Graph 6 - J_{0e} values for p^+np^+ samples symmetrically passivated wih different passivation films [23]

3.4. Boron emitter gettering

Joge et al. [24] verified that submitting bifacial p-type cells, with a phosphorus emitter and boron BSF already formed, to a low-temperature (600 ºC) annealing process led to a significant increase of the bulk lifetime. The authors also proposed a model in which the p^+ layer acted as a gettering site. This gettering would then greatly compensate the lifetime degradation observed after a heavy boron diffusion.

Terakawa et al. [25] did a more developed study of the impact of such low temperature annealing process, comparing wafers with and without the p^+ layer and verified that this layer is mostly important for lower or medium level iron (Fe) contaminations up to concentration values around 10^{13} cm^{-3} (Graph 7). It was also reported that only a very thin superficial portion of the p^+ layer acted as a gettering site, as the formation of a Fe-rich superficial layer was observed.

The authors also proposed a new model for the Fe gettering mechanism (Graph 8). According to this model the Fe contamination level above which the Fe atoms start to precipitate is considerably lower in the p^+ layer than in the p-type bulk, leading to the diffusion of the supersaturated Fe atoms in the bulk material into the surface due to the contamination gradient (Graph 9).

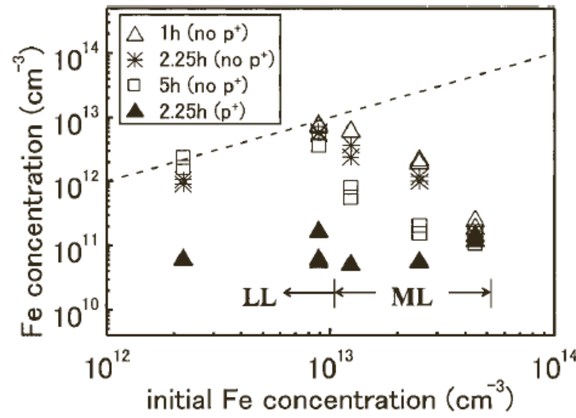

Graph 7 - Fe concentration remaining in bulk Si after annealing at 600 ºC for different periods as a function of initial Fe concentration [25]

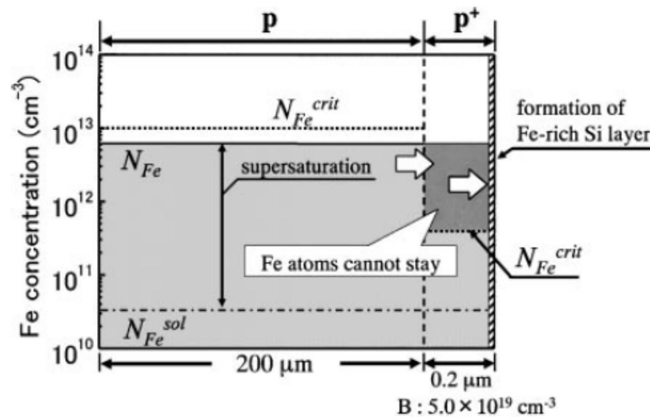

Graph 8 - Fe gettering model in p^+ samples having low-level Fe contamination [25]

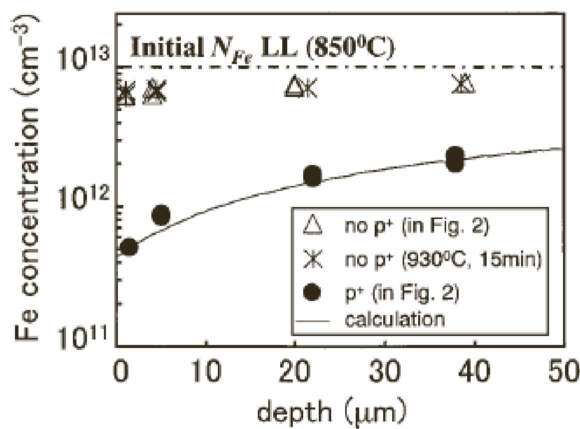

Graph 9 - Depth profiles of Fe concentration in p^+ and no p^+ samples annealed at 600 ºC for 20 minutes after low-level contamination at 850 ºC [25]

Such reasoning seems to be in agreement with the study reported by Tobe et al. [26], where it is mentioned that the Fe segregation in n-type wafers with boron emitters occurs due to the difference in Fe solubility between the deeper, and less doped, p region and the more superficial, and highly doped, p^+ region of the emitter.

Phang et al. [27] verified, through both experimental and simulation results, that boron doping at diffusion temperatures above 850 ºC leads to a completely ineffective gettering, which would mean that a low temperature step afterwards would be required. Low temperature tails, where the diffusion process is extended for a certain duration but at low temperatures, between 600-650 ºC were also tested, by ramping down the furnace temperature after emitter formation leading to a slightly effective gettering and an ineffective surface precipitation. This does not agree with the results obtained by Terakawa et al. who in similar conditions observed a very effective gettering and surface precipitation [25].

Weber et al. [28] reported the ability of the SENTAURUS PROCESS software to reproduce previous gettering experiments with good precision. In this work, it is stated that the interstitial Fe present in the boron emitter is positively charged and is therefore attracted by the negatively charged dopant, leading to the formation of the FeB complex which acts as a very effective recombination center, as it has a capture cross section for minority carriers three orders of magnitude higher than that of interstitial Fe phosphorus-diffused regions. Meaning that when Fe atoms are segregated to the boron emitter surface, where the dopant concentration is higher, the formation of the FeB complex is also enhanced. It is also stated that in the highly boron-doped region the Fe ions accumulate in the region of highest dopant concentration, due to the electrical potential, indicating that the gettering ability of the emitter is not simply proportional to the total number of dopant atoms in the emitter, but proportional to the integral of the square of boron concentration over the depth. This idea was also supported by the fact that Fe gettering showed to be more effective immediately after the boron in-diffusion, when the emitter is still very shallow and heavily doped, but worse after the oxidation step where the doping profile becomes broader but surface concentration is reduced.

In order to evaluate the impact of such gettering in cell's performance, a p^+np^+ structure was simulated, and the emitter's saturation current density (J_{0e}) as a function of the surface recombination velocity was determined. To obtain the upper limits of J_{0e} it was assumed that the iron was completely gettered by the boron diffusion (Graph 10). It was observed that for heavy dopings (higher than 5×10^{19} cm-3) the Fe present in the emitter doesn't affect the value of J_{0e}, since the SRV is the dominant recombination process, but the lighter is the doping the more important is the negative impact of the iron contamination.

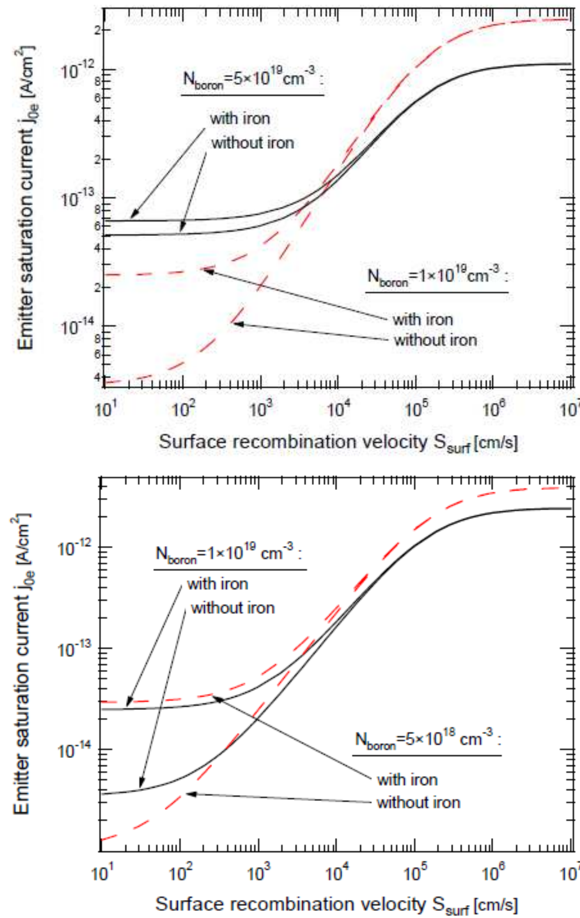

Graph 10 - Simulated J_{0e} as a function of SRV for a boron emitter with two different doping levels, with and without Fe contamination [28]

Phang et al. [18] tested the implementation of a light phosphorus diffusion on both sides of a wafer after a boron emitter had already been formed, simultaneously creating an n^+ region on one side and applying a light n^+ layer on an underlying p^+ layer on the other. This step was meant to evaluate if a light phosphorus doping in the p^+ layer would improve the region's impurity gettering effectiveness. Furthermore, the gettering effectiveness of low surface concentration phosphorus diffusions was evaluated as it can lead to a reduced recombination in both n^+ and p^+ regions [29].

It was experimentally observed that part of the p^+ regions are overdoped by phosphorus, leading to an inversion region of nearly 50 nm thickness, this region's gettering effectiveness is not affected. It was shown that even a P diffusion of 140 Ω/□ resulted in gettering more than 99.7% of the interstitial Fe, especially when a low temperature tail was implemented, being comparable to a situation with no underlying boron emitter.

Finally, it was also observed that this method leads to an enhanced drive in of the boron emitter due to the emitter "push effect"[30, 31, 32], and with that drive in the phosphorus diffusion reverses the gettering effectiveness as it depends on the electrically active dopant concentration.

3.5. Comparison between a boron p^+ region and a classical Al one

In typical p-type solar cells, after the emitter (n^+ layer) is formed an Al layer is deposited (by screen-printing or sputtering for example) in the back surface of the cell and then subjected to a high-temperature step.

The metallic layer then acts as a p-type dopant source and a high-low junction is formed as a p^+ layer is now "present". This junction possesses a built-in potential barrier that greatly reduces the surface recombination of minority carriers of the cell, due to which this p^+ region is designated as Back-Surface Field.

This process is already fully implemented in an industrial fabrication process and offers other advantages as a gettering effect and a good ohmic contact of the screen-printed contact layer with the back surface. However, the use of Al as a dopant source has, as well, its limitations. And that is where boron diffusions for the formation of the p^+ layer comes into play.

First, as it is mentioned by Slade [33], in theory, the surface recombination velocity (SRV) of an emitter below a metal contact depends on the level of doping of such emitter. The higher the doping the lower the SRV and therefore the higher the cell's efficiency. Using computer modeling, the same author verified that for an effective BSF the doping level in the rear layer should be high (over 10^{19} cm^{-3}) and the depth of the layer should be of several microns. However the solid solubility of Al in Si is quite low [34], in the order of 5×10^{18} cm^{-3} for processing temperatures over 600 ºC, so this kind of BSF would be impossible to obtain using Al as a dopant source. On the other hand, boron's solid solubility at the diffusion's range of temperature is around 1×10^{20} cm^{-3} [35].

Additionally, it is well known that in order for the Si solar cells to attain an important share of the global energy market, cost reductions are necessary and reducing the thickness of the solar cell substrate is one of the possible paths to attain this objective [36]. Naturally, for thinner wafers the surface recombination acquires a greater importance and, consequently, the role of BSF becomes more relevant. This being considered, special attention should be given to the enhanced field that a boron p^+ layer could provide [37].

Another limitation of an Al BSF is that when used for thinner wafers this metallic layer can result in solar cell bowing and micro-cracks formation. Thinner substrates imply less toughness and below a certain thickness they become vulnerable to breakages during the several steps involved in the solar cell manufacture chain [38] or even simply in its handling. The most critical processing step for screen-printed cells is the firing process, during which the screen printed Al and silver (Ag) layers are simultaneously annealed in order to form

ohmic contact between the metallic pastes and the substrate. Residual stresses are generated within the cell due to the mismatch of the thermal expansion coefficients and the consequently different mechanical behavior of Si and the materials used in the metallic contacts, which can result in bowing (Figure 1, where δ represents the deflection, t_t and t_b the thickness of the top and bottom components, respectively) and handling problems and therefore lead to cracking and to high yield losses. Power losses of nearly 10% in c-Si based PV modules due to micro-cracks were reported by Köntges [39].

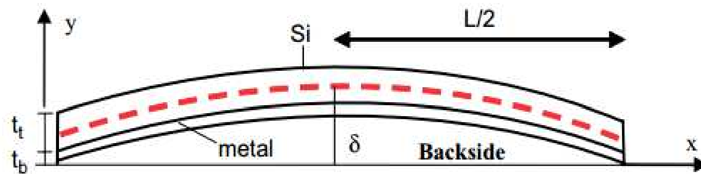

Figure 1 - Schematic of a bowing Si solar cell due to the backside metal contact [40]

These problems can be avoided if the amount of Al paste is reduced or if the paste chemistry and its firing conditions are altered. Nevertheless, the studies reported by Huster [41, 42] and Kim et al. [43], indicate that if the Al paste use is reduced under a certain limit, a non-uniform BSF layer is formed and a worse solar cell is produced. Therefore, if the BSF is formed by boron diffusion, a metallic paste that only makes a good contact can be used, avoiding the bowing/cracking problems.

Finally, if an Al BSF is spanned over all the n-type solar cell area, the whole rear surface is covered by a metallic layer. This fact brings three consequences: as Al is opaque, concepts as bifacial solar cells (Figure 2 and Figure 3), where both sides would receive light, and even concepts as module interconnection (Figure 4 and Figure 5) where the connected cells alternate between n and p-type solar cells, as suggested by Kopecek et al. [44] are not feasible.

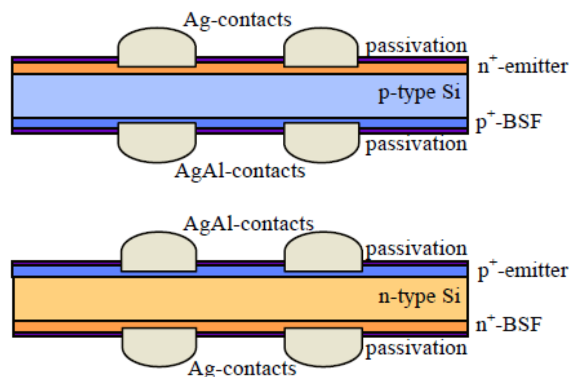

Figure 2 - Bifacial front junction solar cells with opposite substrate doping schematic [44]

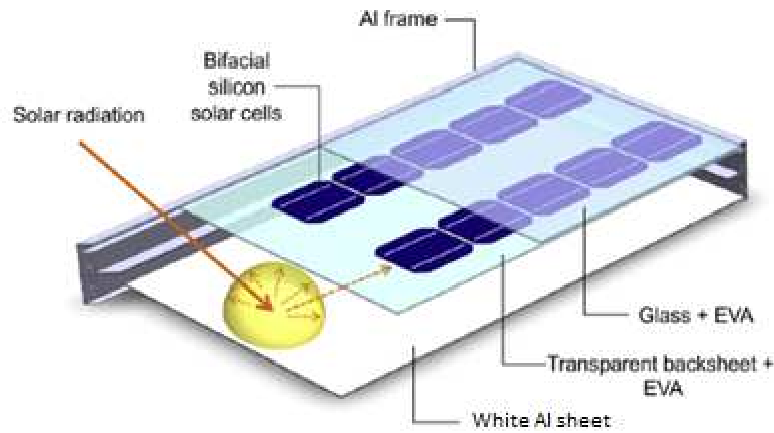

Figure 3 - PV module with bifacial cells and diffuse back reflector [45]

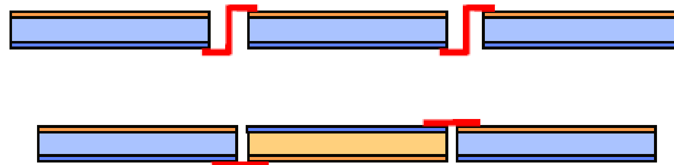

Figure 4 - Interconnection of p-type solar cells in a standard module (top) and of p- and n-type cells in a pn-module (bottom) [44]

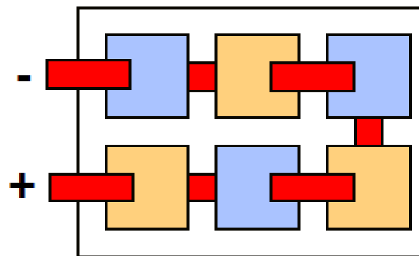

Figure 5 - Scheme of alternate interconnection of p- and n-type solar cells in a 2×3 pn-module [44]

On the other hand, the Al BSF also forbids the use of a dielectric as a passivating layer, which would further reduce surface recombination. Additionally, a bare Si surface that is covered by a dielectric layer offers a better internal reflectivity than a Si surface covered by Al. In an interesting study reported by Wijekoon et al. [46] it was shown that the internal reflectivity of a textured surface that is covered by a dielectric layer (or Passivated Emitter and Rear Cell, PERC) was of about 93% while for the Al covered one it was of only 73% adding to the fact that, naturally, the first case SRV was considerably lower (53 $cm.s^{-1}$ compared with 300 $cm.s^{-1}$) as can be seen in Graph 11.

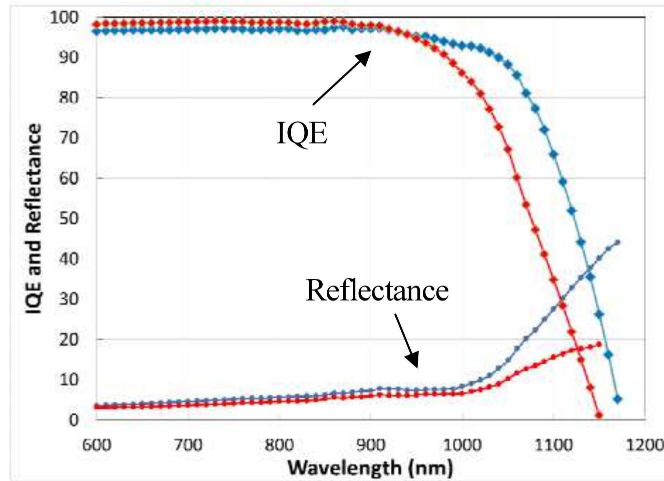

Graph 11 - Internal quantum efficiency and reflectance of a PERC cell (blue) and a reference cell (red) [46]

However, the back reflectivity of an Al layer can be even lower [37], as the high temperature firing step worsens this parameter that can get as low as 40% (Graph 12). Using boron as a dopant, a full area BSF can be achieved while using local metallic contacts and therefore a passivating dielectric layer.

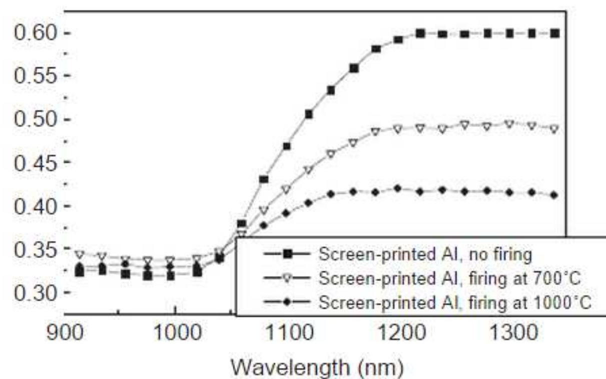

Graph 12 - Reflectivity measurements in wafers with Al BSF fired at different temperatures [37]

3.6. Boron emitter fabrication with BBr_3 as a liquid source

BBr_3 boron doping processes consist in the use of gaseous Nitrogen (N_2) as a carrier gas, as it enters the liquid BBr_3 bubbler and carries the doping source into the open-tube furnace (Figure 6). In addition to the "BBr_3 carrier", a flow of gaseous N_2 and Oxygen (O_2) is also introduced in the furnace.

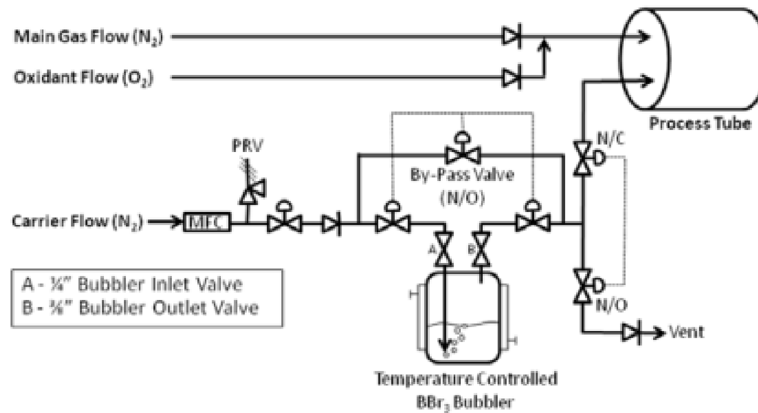

Figure 6 - BBr_3 diffusion setup coupled to a tube furnace[47]

When the gaseous mixture enters the furnace, the BBr_3 reacts with the O_2 and forms Boron Trioxide (B_2O_3) and Bromine (Br_2) as is shown in the following equation [48],

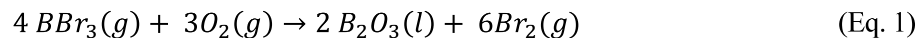

$$4\,BBr_3(g) + 3O_2(g) \rightarrow 2\,B_2O_3(l) + 6Br_2(g) \quad \text{(Eq. 1)}$$

One of the main differences between BBr_3 and Phosphoryl Trichloride ($POCl_3$) (also a liquid source which is the standard for p^+ layers formation) doping processes is that the doping agent which is formed after the source interacting with the O_2 present in the furnace (B_2O_3 and Phosphorus Pentoxide (P_2O_5), respectively) evaporates at quite different temperatures. While P_2O_5 is completely evaporated at the diffusion process temperature, for B_2O_3 that only happens at 1860 ºC at 1 atm [49]. Being BBr_3 processes temperature between 950-1100 ºC, B_2O_3 the dopant is majorly liquid during the diffusion.

The liquid B_2O_3 then condenses on the wafer's surface and reacts with the Si itself, simultaneously originating Silicon Dioxide (SiO_2) and introducing elemental boron in the wafer (Equation 2). As the solid SiO_2 is partly dissolved in the liquid B_2O_3, the then formed Borosilicate Glass (BSG) consists in a mixed-phase system [48],

$$2B_2O_3(l) + 3Si(s) \rightarrow 4B(s) + 3SiO_2(s) \quad \text{(Eq. 2)}$$

According to Zhou et al. [49], the fact that a liquid B_2O_3 flows on the substrate surface induces a non-homogeneous doping both at a wafer-to-wafer or in-wafer scale. For open-tube furnaces a mentioned solution is the use of a vacuum pump which regulates the equipment's inner pressure so that the B_2O_3 boiling point is reduced to 950 ºC. Another solution is the use of a gaseous boron source to act as a buffer agent for B_2O_3 vapor which can be formed either by using spin-on boric acid [50], using water vapor instead of O_2 as oxidant [51] or a mix of water vapor and O_2 as oxidants [49].

When water vapor is used as an oxidant, the following chemical reaction is observed [49],

$$BBr_3(g) + 2H_2O(g) \rightarrow HBO_2(g) + 3HBr(g) \qquad \text{(Eq. 3)}$$

Then, when the Oxoborinic acid (HBO_2) is heated at a temperature beyond 250 ºC, B_2O_3 starts to form [49],

$$2HBO_2(g) \rightarrow HO_2(g) + B_2O_3(g) \qquad \text{(Eq. 4)}$$

The formed HBO_2 acts as a buffering agent for B_2O_3 vapor. The BBr3-H2O system, instead of the traditional BBr3-O2 system, allows control of much lower concentration boron diffusion in Si [52].

The method suggested by Zhou et al. [49] lead to great improvements in doping homogeneity in terms of in-wafer and wafer-to-wafer, where uniformities within 10% were achieved (Graph 13).

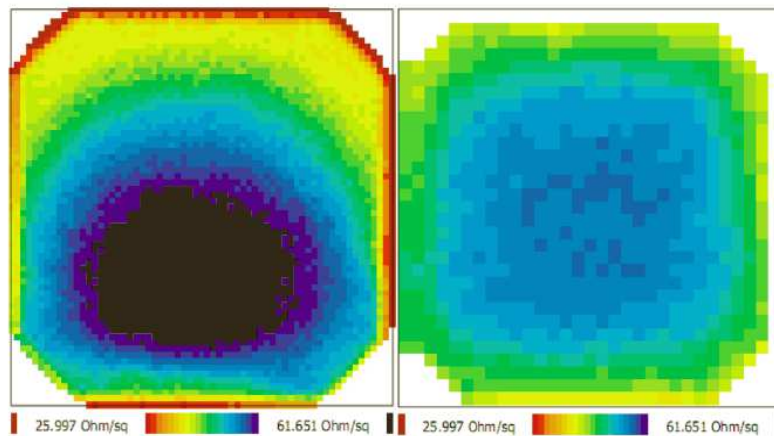

Graph 13 - R_{sheet} deviation reduction (from 21% to 10%, left to right) by adding water vapor during the drive-in step [49]

The elemental boron present at the wafer-glass interface then diffuses into the wafer forming the emitter. If the boron diffusion rate is lower than the formation rate of elemental boron then an accumulation of the doping element occurs at such interface, which is designated as "pile-up". When the amount of a piled-up boron is higher than its solid solubility limit in Si the dopant reacts with the wafer's surface and forms a Si-B compound, as is described by Equation 5 [53] and can be seen in Figure 7.

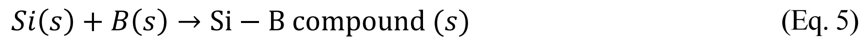

$$Si(s) + B(s) \rightarrow \text{Si} - \text{B compound } (s) \quad \text{(Eq. 5)}$$

Several Si-B compound structures have been suggested, such as SiB_4, SiB_5 [53, 54] or SiB_6 in more recent studies [53, 55, 56]. The Si region containing the Si-B compounds is usually named Boron-Rich Layer but it can also be identified as Boron-Silicon Layer, or Boron Stain [48, 53, 57].

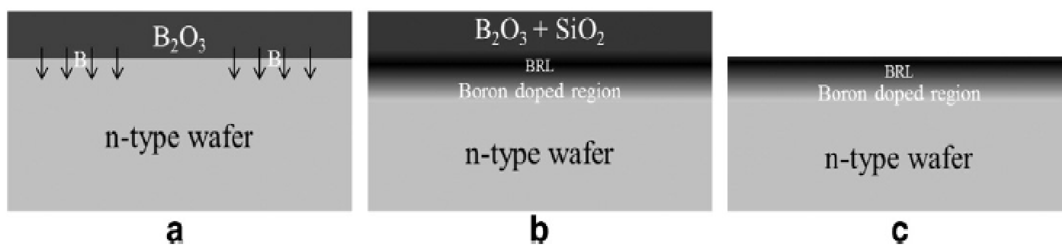

Figure 7 - Schematics of a BRL formation: (a) B_2O_3 layer already formed and doping the substrate, (b) the boron atoms start to "pile-up" at the interface forming the BRL, (c) the BSG is removed by HF dip [58]

More recently, a study by Kim et al. [58] identified the BRL as an amorphous structure composed by boron, Si and O_2. The O_2, from the SiO_2 formed during the doping process (Equation 2) is considered the probable cause for the amorphous structure.

Arai et al. [53] reported that the BRL is insoluble in hydrofluoric acid (HF) and studied the BRL growth conditions and the resulting R_{sheet}/doping profiles, as a function of the boron source used and the N_2 and O_2 gas flows. In particular for deposited boron doped oxide, it was found that when a pre-deposition process occurs at 950 ºC in an exclusively N_2 atmosphere the thickness of the BRL increases rapidly with time up to 1 hour and saturates beyond it while for an O_2 atmosphere not only this layer is too thin to be measured but also after a certain process duration the layer is no longer present. Meaning that the growth rate of this compound is reduced as the O_2 concentration in the atmosphere increases.

This occurs due to diffusion of the O_2 present in the furnace tube through the BSG, which compared to a standard SiO_2 or Phosphorus Silicon Glass (PSG), is very permeable to O_2, reacting with either the BRL or Si (if the first is not present) leading to two possible reactions [53] ,

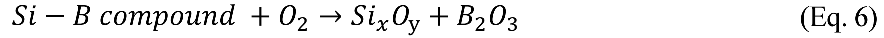

$$Si - B\ compound\ + O_2 \rightarrow Si_xO_y + B_2O_3 \quad \text{(Eq. 6)}$$

$$Si\ + O_2 \rightarrow SiO_2 \quad \text{(Eq. 7)}$$

Additionally, it was observed that when doping in a N_2 atmosphere, the bigger the growth rate of the BRL the lower the boron doping rate [53] (Graph 14). In the case of an O_2 atmosphere, until a certain process duration lower R_{sheet} values are obtained (heavier doping) in comparison with the N_2 situation. However, after a duration limit the doping rate starts to slow down and eventually the R_{sheet} starts to increase. Such effect is related with the degradation and removal of the BRL (Graph 14). This can be explained by the fact that as soon as the BRL disappears, the wafers are in direct contact with the SiO_2 layer which induces boron segregation from the emitter.

Significantly thick SiO_2 layers resulted from all doping processes [53]. At 900 ºC. doping processes made on a dry O_2 atmosphere lead to SiO_2 films 3 times as thick as the ones obtained in an N_2 atmosphere and 70 times thicker the oxide films grown with a standard dry Si oxidation. Additionally, it was observed that the oxide growth was proportional to the square root of the heat-treatment time for the studied process. This fast growth is explained not only by the existence of an additional O_2 source, other than B_2O_3 (as SiO_2 is produced when B_2O_3 reacts with Si) but also due to an enhanced oxidation due to the high permeability of the BSG to O_2, oxidizing either the BRL or the Si.

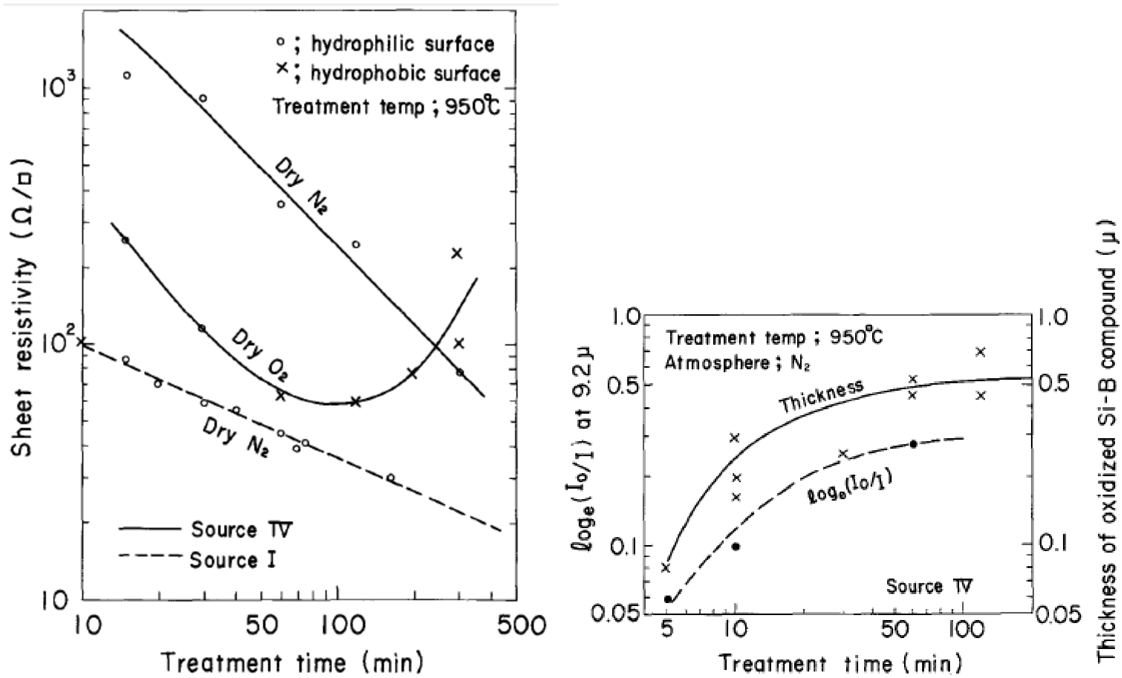

Graph 14 - Rsheet (left) and BRL thickness (right) in terms of the deposition step duration for different processes [53]

3.7. BRL Characteristics

The BRL possesses several characteristics that need to be understood in order to design any solar cell fabrication process. It is usually considered that as long as the BRL layer is present, the doping process is based on an infinite doping source, where the doping process is more tolerant to environment variations [53]. This means that as long as a minimum BRL covers completely the wafer's surface, a uniform doping should be obtained, as it is only dependent on the layer presence and not on its thickness.

It is also known that the high SRV resulting from a BRL is due to inactivate B, segregated metal impurities and structural defects [22]. All these factors impede an effective surface passivation and lead to lifetime degradation.

Regarding the structural defects, Prussin et al. [59] reported that the presence of a BRL induces mechanical tension that results in the generation of dislocations within the emitter region, while Ning [60] demonstrated that such dislocations can glide past the diffusion junction into the bulk region, resulting in a reduced bulk lifetime, as was reported by Cousins et al. [61]. All authors were in agreement regarding the fact that the tension induced by this layer is proportional to the amount of dopants present, meaning that it is a function of the surface concentration of the dopant and the junction depth.

A clear correlation between BRL thickness and bulk lifetime degradation was observed by Kessler et al. [48], as can be seen in Graph 15, where a layer with at least 10 nm thickness seems to have a significant impact.

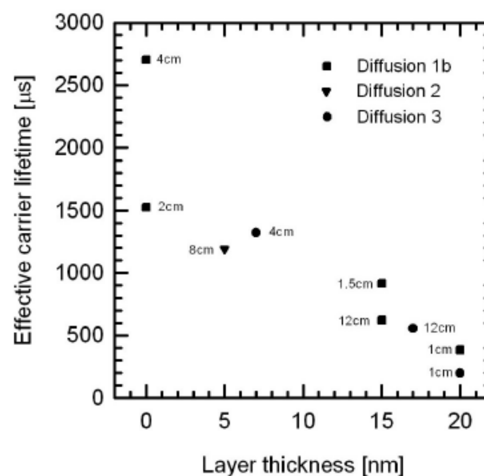

Graph 15 - Carrier lifetime as a function of BRL layer thickness [48]

In terms of optical properties, the BRL showed to be responsible for an increase of reflectance in the UV region, resulting in a decrease of about 0.05 $mA.cm^{-2}$ in J_{SC} [58]. However, when the full spectrum is considered, the refractive indices measured by ellipsometry showed that in fact the BRL acts as a anti-reflecting coating worse than SiN_x

but better than standard crystalline silicon. Additionally, a BRL with a high boron concentration, which can depend on the process conditions, can offer a low-contact resistance (as low as 0.8 $m\Omega.cm^{-2}$) making this layer applicable for high efficiency n-type concepts, mainly selective emitter structures, as it would lead to a fill factor increase.

3.7.1. Identification and thickness Measurement of a BRL

One of the characteristics of a BRL is that it is hydrophilic while Si is hydrophobic. Therefore, the presence of a BRL is verified by removing the BSG layer in an HF bath, exposing the BRL surface (which does not react with the acid), and then bathing the doped wafer in a deionized water (H_2Odi) bath in order to verify if any hydrophilic region is present.

Regarding the measurement of BRL and BSG layer's thickness, several techniques have been reported so far. Kessler et al. [48] suggest the use of Secondary Electron Microscopy (SEM) images of the cleaved edge of the Si wafers as a possibility, as shown in Figure 8, while Schiele et al. [62] suggest the use of Atomic Force Microscopy (AFM) and Kim et al. [58] propose the use of Transmission Electron Microscopy (TEM) images.

Additionally, Ryu et al. [22] reported that high resolution electron microscopy (HREM) images allowed the identification of the BRL and the measurement of its thickness, as the authors used these to evaluate the potential of Nitric Acid Oxidation (NAO) for the removal such layer (Figure 9).

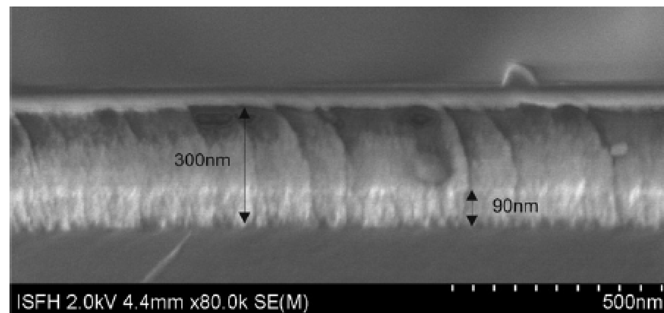

Figure 8 - Micrograph of the two-phase layer system 20 µm from the wafer top of the sample, showing a 300 nm BSG and a 90 nm BRL [48]

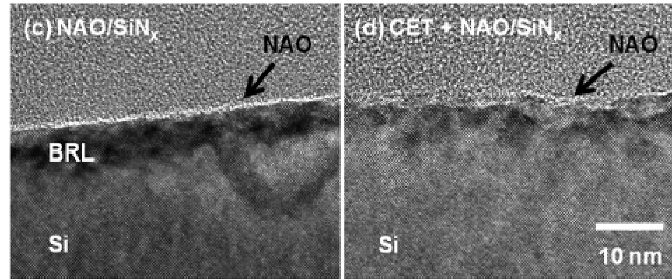

Figure 9 - HREM images obtained from a symmetric NAO/SiNx passivated boron emitter (SiN_x-NAO-p^+-n-p^+-NAO-SiN_x) structure: (c) with BRL, (d) with BRL removed [22]

Finally, the determination of the thickness of the layer, which comprises both BSG and BRL, can be made through visual observation of the doped wafer and comparison of the surface color with a thermally grown SiO_2 color chart presented as Attachment 1: Color Char for Thermally Grown SiO2 [63]. Such method, which does not require any special kind of equipment, was suggested by Kessler et al. [48]. Schiele et al. [62] also reported a correlation between wafer surface's color and respective BSG thickness where, as an example, a 10 nm and a 150 nm thick BSG correspond to a transparent and light blue color, respectively, where the last value agrees with the SiO_2 color chart.

This method was based in an initial assumption that the optical properties of the BSG-BRL layer were similar to that of a pure SiO_2 layer. After comparing the results obtained using such method with measurements based on SEM images (Graph 16) it was observed that this method results in a constant overestimation of the film thickness no larger than 20% [48].

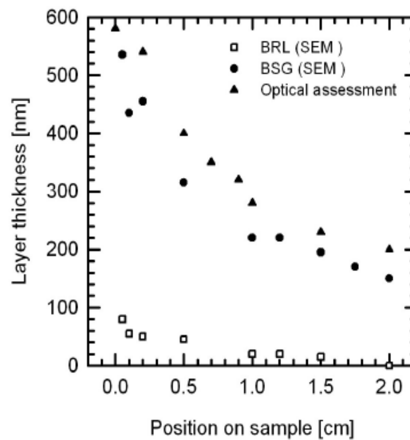

Graph 16 - BRL and BSG thickness assessed through SEM and optical measurement methods [48]

3.7.2. Parameters impact on BRL formation and wafer properties

Several works have been presented that investigate the impact of different experimental parameters on the BRL formation and the wafer properties, during a BBr_3 doping process in open-tube furnace.

Kessler et al. [48] studied the phenomenology of the BRL formation and analyzed how parameters like BBr_3 flow, O_2 flow and deposition time affected the growth of this layer , the properties of the wafer (R_{sheet} and bulk lifetime) and these parameters spatial uniformity. Using 125×125 mm^2 n-type Cz Si wafers with 6-8 Ω.cm as base material for lifetime measurements and 3-4 Ω.cm for R_{sheet} measurements, the diffusion process implemented consisted in a BBr_3 predeposition using BBr_3, N_2 and O_2, followed by a drive-in N_2 or O_2 atmosphere. Finally after the diffusion process, the BSG layer was removed in diluted HF.

Schiele et al. [62] studied the impact of temperature, BBr_3 and N_2 flows, and deposition time, in the resulting doping profile along the wafer thickness, minority carrier lifetime of the substrate and BSG layer thickness. Using 156×156 mm^2 n-type Cz Si wafers with 2-5 Ω.cm resistivity as base material, the diffusion process implemented consisted in four different steps: heating-up/stabilization (with only N_2 and O_2); BBr_3 predeposition (with BBr_3, N_2 and O_2); drive-in (N_2 and O_2) and cooling-down (only N_2). Finally, after the diffusion process, the BSG layer was removed in diluted HF.

3.7.2.1. BBr3 flow during predeposition step

Schiele et al. [62] verified that for a wide range of BBr_3 flow values during the predeposition step no significant changes in R_{sheet}/doping profile were observed. However, when the BBr_3 flow is below that range, a significantly worse doping is obtained (Graph 17), suggesting that for BBr_3 flow rates higher than a certain value, the resulting emitter is the same. This may be explained by the formation of a BRL, which would imply an infinite source doping process, which is in agreement with the results obtained by Arai et al. [53].

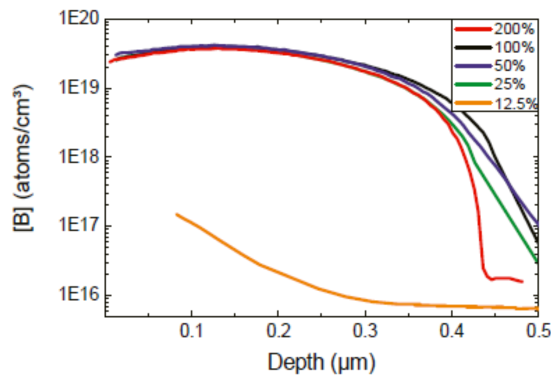

Graph 17 - Measured depth profile of boron concentration for different BBr_3 flow [62]

It was observed that even if, for the mentioned range, the doping in one point does not vary with the BBr_3 flow, the R_{sheet} homogeneity diminishes when the dopant flow increases. This behavior was also correlated with the BSG layer thickness, it was observed that the higher is the BBr_3 flow, the thicker is the BSG layer and the lower is spatial uniformity (Graph 18). The anisotropy of R_{sheet} can also be observed in the BSG thickness as it can be seen be the variability of the wafer surface color (Figure 10). It is also suggested that up to a certain BRL thickness, the layer grows uniformly possibly due to the fact that the occurring chemical reactions are controlled by the reaction activity of the reactants, but as the resulting SiO_2 interface layer gets thicker the reactions seem to be increasingly influenced by local variability of experimental parameters such as gas flow or temperature.

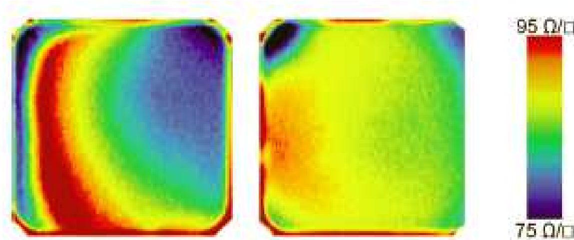

Graph 18 - R_{sheet} distribution on a 156×156 mm^2 wafer after diffusion with 100% (left) and 25% (right) relative BBr_3 flow [62]

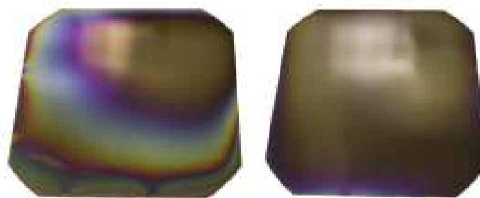

Figure 10 - BSG distribution on a 156x156 mm^2 wafer after diffusion with 200% and 50% (right) relative BBr_3 flow [62]

Finally, a degradation of the minority carrier lifetime up to 66.6% was observed for an increasing BBr_3 flow, suggesting that defects and/or contamination may originate from the BBr_3 itself, possibly due to products of chemical reactions, electrically inactive boron atoms or even from the strain caused by thick BSG layers.

Kessler et al. [48] increased the BBr_3 flow comparably to a reference doping process where a BRL was formed, but that did not cover the entire wafer surface. This increase resulted not only in a thicker BSG layer but also in a BRL that completely covered the wafer surface. Additionally, it was observed that, in comparison with the reference process, this flow increase lead to a decrease of the average bulk lifetime of the wafer from 3.35 ms to 0.65 ms, where the higher values correspond to the regions with a thinner BSG layer or without BRL.

3.7.2.2. O_2 flow during predeposition step

Increasing the O_2 flow during the predeposition step, induced the formation of a slightly thicker BSG layer that completely covered the wafer surface thickness [48]. However, it also led to a 15% increase in the wafers average R_{sheet}, suggesting that the oxygen increase led to an additional oxidation of the elemental boron present in the BSG and therefore a reduction of the dopant supply to the Si surface.

3.7.2.3. N_2 carrier gas flow during predeposition step

Schiele et al. [62] observed that varying the N_2 carrier gas flow during BBr_3 deposition did not lead to a change in R_{sheet}, except for significantly high flows where the boron content in the diffusion tube is highly diluted. This may be related with the absence of formation of a BRL, which would also explain the low impact small changes in the N_2 flow. This situation is similar to a low BBr_3 flow predeposition where the boron deposited is also meager and a low level of doping is obtained.

3.7.2.4. Predeposition step

It was shown that an increase in the predeposition time results in a deeper doping profile and for longer periods it might also result in a higher surface doping [62]. It was also found that an increase of the deposition time worsens the doping uniformity, being this effect correlated to an also non-uniform BSG layer growth. This result is similar to the non-uniformity found for higher BBr_3 flows where the BSG layer was thicker as well.

Arai et al. [53] carried out an experiment where boron was diffused using a B_2H_3-O_2 gas system in a 30 minutes doping process. This duration included both a predeposition step (with N_2, the doping source and O_2) and a drive-in step (with only N_2) and different time distributions between these two steps were tested. It was observed that for temperatures over 900 ºC, after a predeposition time shorter than 3 minutes carrying either with the predeposition or following with a drive-in for the remaining 27 minutes resulted in almost an identical R_{sheet} (Graph 19). This would mean that after those 3 minutes even though a doping atmosphere is present, the wafers are no longer being doped.

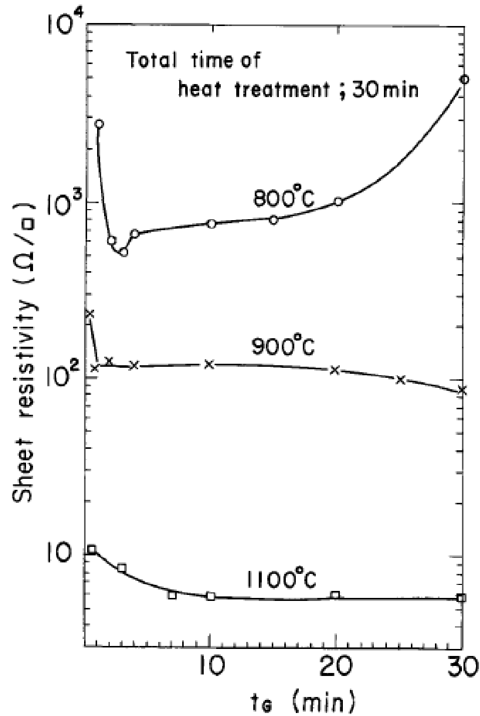

Graph 19 - Dependence of R_{sheet} on t_G at 800 ºC, 900 ºC and 1100 ºC for a B_2H_6-O_2 gas system [53]

Additionally, it was verified that increasing the deposition time from 30 to 60 minutes results in a thicker BSG layer and a larger coverage of the wafer surface with BRL, while reducing to 10 minutes results in almost no BRL coverage (Graph 20). The increase to 60 minutes also lead to a decrease of the average bulk lifetime degradation from 3.35 ms to 0.98 ms when compared to the 30 minute process and by analyzing Graph 21 it is visible that the mentioned reduction is due to the region covered by the BRL. However, the authors also mention that reducing the diffusion duration to 10 minutes actually lead to a decrease from 3.35 ms to 3.01 ms [48]. Both duration changes resulted in no change of the emitter's R_{sheet}.

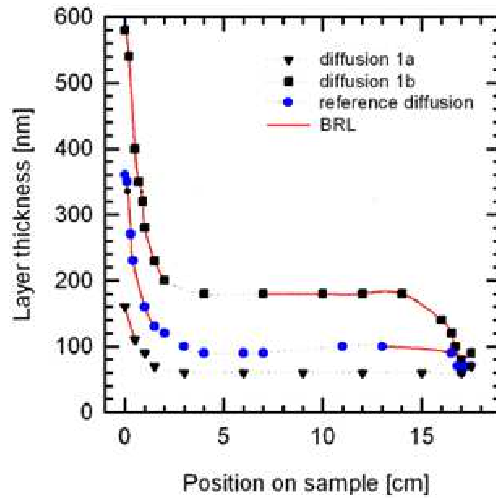

Graph 20 - Overall BSG/BRL layer thickness, on silicon wafer surface as a function of position, where the reference diffusion took 30 mins, the diffusion 1a 10 mins and the diffusion 1b 60 mins [48]

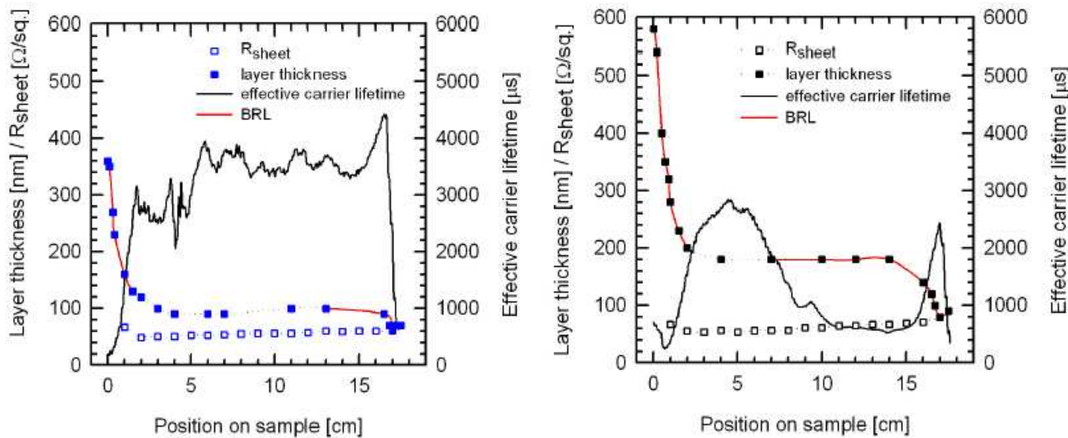

Graph 21 - Line scan of the bulk carrier lifetime and doping mapping for a reference diffusion (left) and another diffusion with a longer duration (right) [48]

3.7.2.5. Temperature

A variation of ± 20 ºC of the tube furnace temperature was studied by Schiele et al. [62] and a major influence on the R_{sheet} was found, as the boron diffusivity strongly depends on this parameter. While the temperature reduction led to a higher R_{sheet} and a lower spatial uniformity, the temperature increase had an opposite effect (Graph 22). This change is majorly caused by a deeper doping profile as the surface doping does not change significantly (Graph 23).

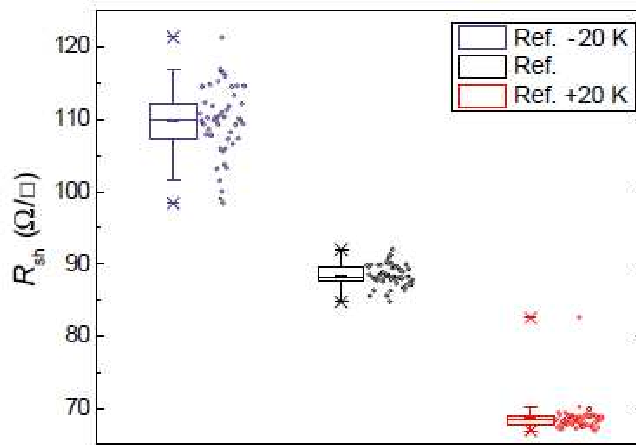

Graph 22 - R_{sheet} distribution on a 156 x 156 mm² wafer measured by four-point probe method for different diffusion temperatures [62]

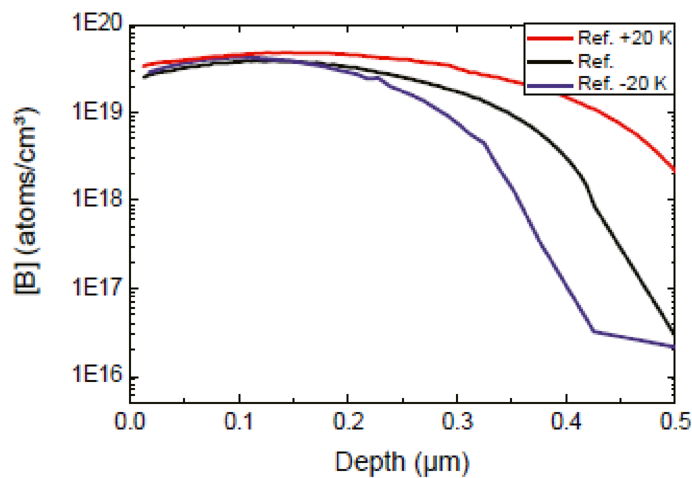

Graph 23 - Depth profile of boron concentration measured for different diffusion temperatures [62]

3.7.2.6. BRL Removal and Boron Segregation into SiO_2

As mentioned before the BRL is insoluble in HF and it seems to dissociate in the presence of O_2, forming SiO_2. Several methods for the BRL removal have been presented so far and all of them are based in either the chemical or thermal oxidation of this layer.

Busen et al. [64] and Arai et al. [53] suggest a sequential H_2Odi and HF dip after the doping process in order to remove respectively the unreacted B_2O_3 and the BSG, followed by a low-temperature oxidation. However, according to Buck et al. [65], this method leads to the depletion of boron from the emitter into the SiO_2. This phenomenon occurs due to the segregation of the dopant into the substrate and the oxide, forming what is called a depletion

region. This segregation effect can be avoided if the previous "BSG removal+thermal oxidation" process is replaced by an in-situ oxidation immediately after the predeposition. As the BSG and the BRL are kept on the wafer during the oxidation step the depletion is greatly attenuated (Graph 24).

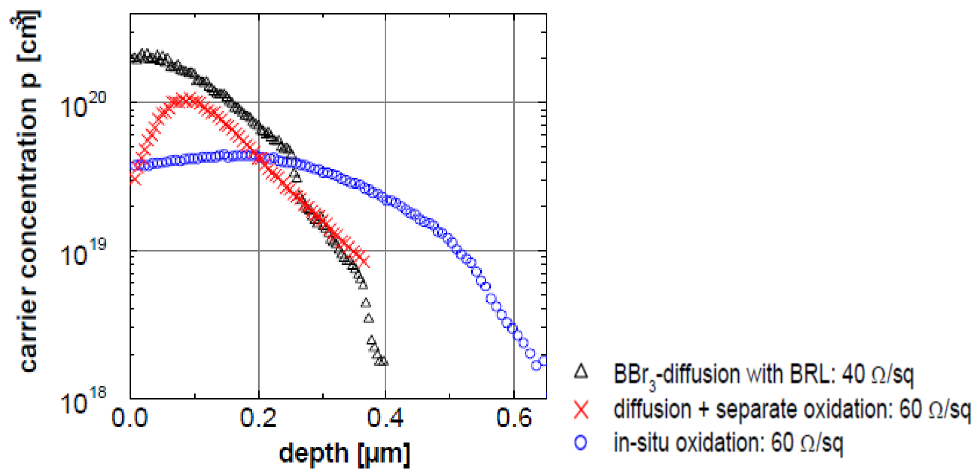

Graph 24 - Measured diffusion profiles of boron emitters with and without BRL [65]

Finally, the removal of the BRL by chemical etch with a solution of HNO_3, glacial acetic acid (CH_3CO_2H) and HF is suggested by several authors [22, 58].

These different methods have several implications in the whole fabrication process chain either in terms of gettering or passivation. Typically, a thermal oxidation leads to the formation of a high-quality oxide which results in a good chemical passivation. However, the high thermal budget of this process can result not only in higher costs but also lead to other issues such as boron depletion into the oxide, or even cancel the gettering effect induced by the emitter diffusion [18].

In terms of the emitter, there is yet another important technological disadvantage of the n-type silicon solar cells when compared to p-type silicon solar cells, which has to do with the simplicity and reproducibility of a phosphorus diffusion to form the n-type emitter in a p-type solar cell, typically done using a liquid Phosphoryl Chloride ($POCl_3$) source, which at the same time has the beneficial effect of gettering the metal impurities in the bulk if a surface doping of at least 5×10^{19} cm^{-3} is achieved [66]. From what has been reviewed in the present chapter, it becomes clear that diffusing a p-type emitter in a n-type substrate is one of the main challenges for the fabrication of high-efficiency solar cells, and therefore will be the main focus of the present work

4. Materials and methods

4.1. Open-tube furnace and flow meters

For the present work an open-tube furnace 1.83 m long and with a diameter of 0.145 m was used. Three equidistant resistances are placed at the start, center and end of such tube and the control of temperature in the furnace is the following: the absolute temperature at the central resistance is imposed by the controller and the temperature at the border resistances is defined according to this value, allowing interior temperatures between 400 ºC and 1200 ºC.

Connected to the furnace is a set of tubes and flow controllers through which the gases are introduced, a scheme of the whole setup is presented in Figure 11.

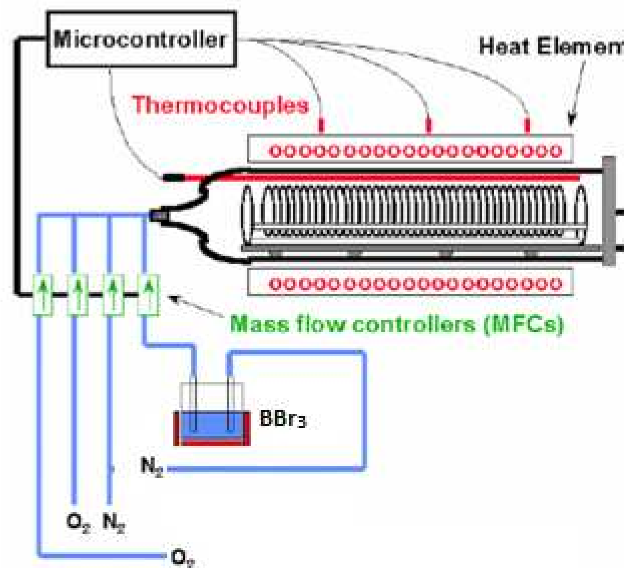

Figure 11 - Scheme of the used setup, consisting in an open tube furnace and its gas channels/sources and a liquid BBr_3 source [67]

The gas distribution setup consists in two O_2 channels, having different ranges of gas flows and two N_2 channels, one of which goes through the BBr_3 bubbler acting as a carrier gas and an individual N_2 channel that goes directly into the furnace tube.

The flow ranges allowed by the used flow meters are presented in the following table. In the present work, gas flows are expressed in units of standard liter per minute (slm), where reference conditions (temperature of 0 ºC and a 1 atm pressure) are assumed.

Flow meter	Flow range [slm]
Main N_2	1.03 – 17
N_2-BBr_3	0.01 - 0.09
High O_2	0.24 - 2.17
Low O_2	0.02 - 0.27

Table 1 - Flow ranges for the used flow meters

4.1.1. Furnace tube walls as doping source

In order to enhance boron diffusion, a long-run predeposition process with an empty furnace tube was performed. According to the bubbler documentation from the manufacturer [68], this would lead to a buildup of B_2O_3 in the furnace tube walls making it act as an additional doping source.

The same document mentions that this buildup occurs after a sequence of 30-50 runs of diffusion processes. Considering that each predeposition step is 20 minutes long (totaling 17 hours for the 50 runs case), two 10 hour processes were done before doing any experiment with wafers.

4.1.2. Bubbler theory

The BBr_3 pickup rate can be calculated as a function of the carrier gas (N_2) flow rate and the bubbler temperature, according to Equation 8 [47].

$$m_{BBr3} = \frac{P_{vap}}{P_{bubbler} - P_{vap}} \times Q_{N2} \times \frac{MW}{\mathrm{MV}} \times \frac{273}{T_{bubbler}} \quad [g.\mathrm{min}^{-1}] \qquad \text{(Eq. 8)}$$

where P_{vap} (Torr) is the BBr_3 vapor pressure, $P_{bubbler}$ (Torr) is the pressure in bubbler, Q_{N2} ($cm^3.min^{-1}$, at 273 K) the N_2 carrier flow, MW=250.54 $g.mol^{-1}$ is the BBr_3 molecular weight, MV=22414 $cm^3.mol^{-1}$ is the molar volume at standard temperature and pressure conditions (273 K and 1 atm) and $T_{bubbler}$ (K) is the bubbler temperature.

From a graph of the BBr_3 vapor pressure as a function of bubbler temperature [68] an empirical relationship between these two parameters with a coefficient of determination of 0.979 was established (Equation 9).

$$P = 1.1095 + 17.5591 \times \exp\left(\frac{T_{bubbler}}{20.2039}\right) [Torr] \qquad \text{(Eq. 9)}$$

Graph 25 shows an example of BBr_3 pickup rates for different N_2 carrier gas flows and for different temperatures.

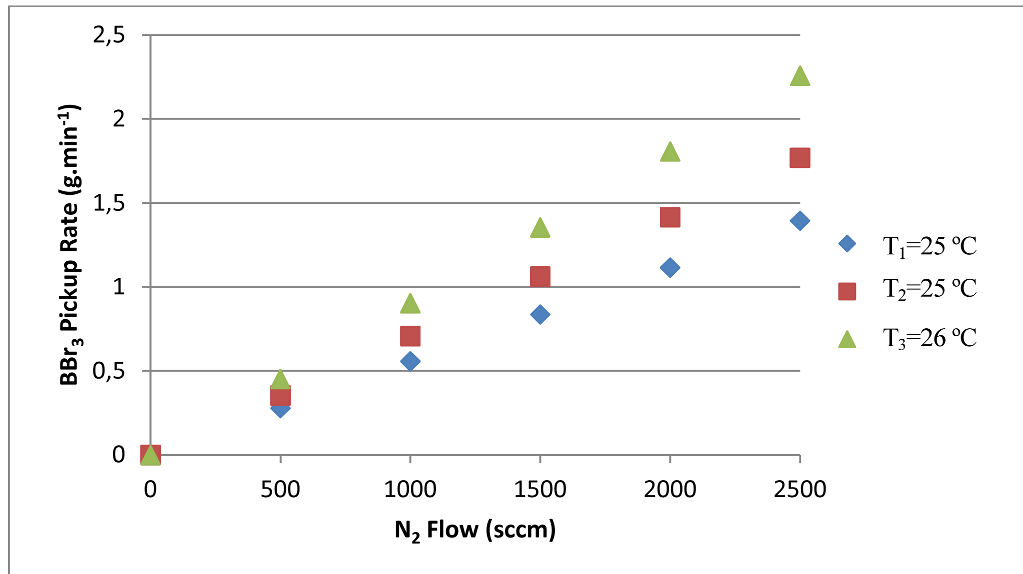

Graph 25 - BBr_3 pickup rates at different bubbler temperatures

In this section, the characterization procedures used in the present work are listed, adding a small description when not already mentioned previously.

4.1.3. Oxide thickness assessment

4.1.3.1. Spectroscopic ellipsometry measurements

This technique consists on measuring the variation of the polarization of electromagnetic radiation of different wavelengths when reflected in a plane surface (Figure 12), and using an appropriate theoretical model to determine the thickness and optical properties (refraction index *n* and extinction coefficient *k*) of thin layers.

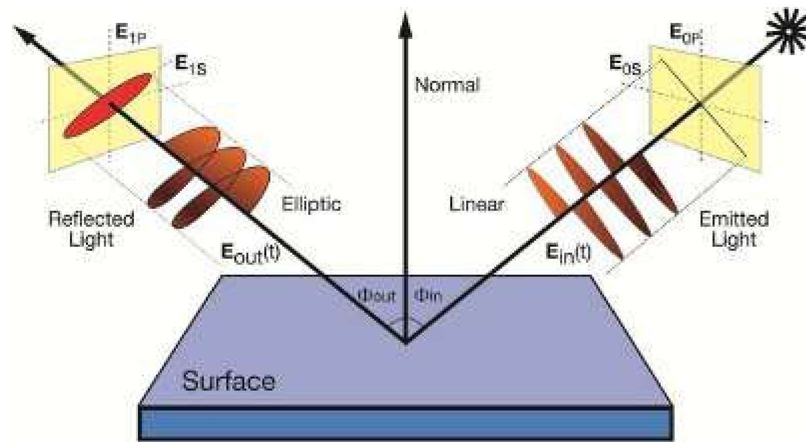

Figure 12 - Scheme of a ellipsometry process [69]

Spectroscopic ellipsometry has several advantages:

- high precision estimation of a superficial layer thickness;
- reproducible and non-destructive;
- does not require any wafer preprocessing;
- low time consumption;
- not sensible to light intensity fluctuations.

On the other hand, this method has some limitations:

- only thin layers can be analyzed, with thicknesses not exceeding 10 µm;
- only planar surfaces can be measured.
- it requires the use of complex theoretical model to treat the results.

The use of this technique for the evaluation of the BRL optical properties has been suggested [58], but for the present work it was only used to measure the thickness of the BSG/BRL stack, being its importance explained in more detail in the section below.

4.1.3.2. Oxide Thickness visual assessment

As already explained, during this work the thickness of the BSG-BRL layer was evaluated by comparing its color along a defined line with a SiO_2 color/thickness chart. These measurements were complemented with spectroscopic ellipsometry measurements of the BSG-BRL layers.

The ellipsometry measurements not only served as validation but also as a reference for the starting point, as the SiO_2 color chart has a periodical behavior which makes the visual evaluation difficult when done independently.

4.1.4. BRL presence assessment

As mentioned before, to identify the presence of a BRL in a boron emitter it simply requires dipping a wafer in diluted HF in order to remove the BSG, which exposes the wafer's surface, followed by a dip in H_2Odi. After having the glass removed, the water dip enables to verify if the surface has a hydrophilic nature, corresponding to the presence of a BRL, or hydrophobic one, corresponding to non-oxidized Si. Additionally, the measurement of the area of the wafer that is indeed covered by a BRL, has been suggested by Kessler et al. [48] in order to evaluate the impact of the different experimental parameters in the formation of this particular layer.

4.1.5. Resistivity assessment

According to equation 7, one can calculate the resistivity of a wafer from the concentration and carrier mobility measurements (Equation 10). However, these values are generally not known and in case of the mobility it even depends on the doping of the wafer. Therefore, the resistivity is usually measured and not calculated and it is used as an indicator of the wafers' level of doping.

$$\rho = \frac{1}{q \times (n \times \mu_e + p \times \mu_h)} [\Omega . cm] \qquad \text{(Eq. 10)}$$

The measuring technique used in the present work was the four-point probe method [70]. The method is based on the use of a probe which has four tips that connect four collinear and equidistant points (Figure 13). A current is applied between the two external points and measured with an ammeter, simultaneously the voltage then established is measured between the two interior points with a voltmeter.

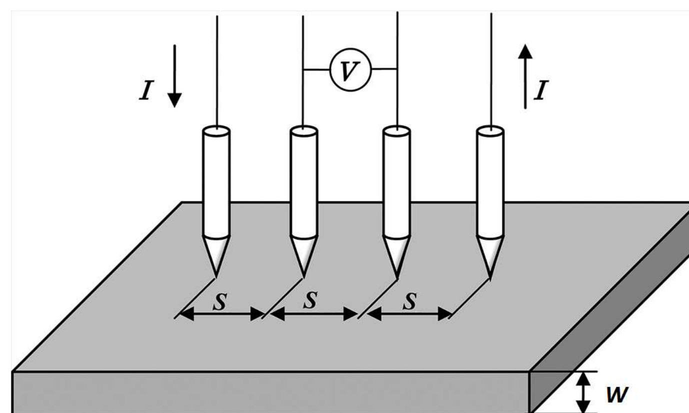

Figure 13 - Scheme of four-point probe measurement [71]

If the conditions in Equation 11 are observed, the resistivity can be measured using Equation 12.

$$W \leq \frac{s}{2};\ d \geq 4s \qquad \text{(Eq. 11)}$$

$$\rho = \frac{\pi}{\ln(2)} \times \frac{V_{measured}}{I_{applied}} \times Thickness\ [\Omega.cm] \qquad \text{(Eq. 12)}$$

where W is the wafer thickness, s the distance between each probe, d is the distance of probes to the wafer borders and I and V the measured current and voltage.

It is also interesting to mention that the results obtained with this method are absolute measurements, and do not require any calibration, unlike for instance the two point probe method measurements.

After obtaining the resistivity values, the calculation of the wafer doping levels was done with equation 10, after assuming an electron mobility of 1440 $cm^2.V$ which is a value considered acceptable for the range of doping expected [72],

$$N_{int} = \rho \times 1.6 \times 10^{-19} \times \mu_{minority\ carriers} = \\ = \rho \times 1.6 \times 10^{-19} \times \mu_{electrons}\ [cm^{-3}] \qquad \text{(Eq. 13)}$$

4.1.6. Sheet resistance assessment

To evaluate the doping level of an emitter is quite complicated as both its resistivity and thickness are unknown. To characterize the junction depth and doping level usually a parameter designated as sheet resistance is used, which can be obtained using equation 11. As the junction between the n and p -type regions behaves as an insulating layer, it guarantees that the current only flows in the emitter (Figure 14).

$$R_{\mathbf{sheet}} = \frac{\rho}{Thickness} = \frac{\pi}{\ln(2)} \times \frac{V_{measured}}{I_{applied}}\ [\Omega/\square] \qquad \text{(Eq. 14)}$$

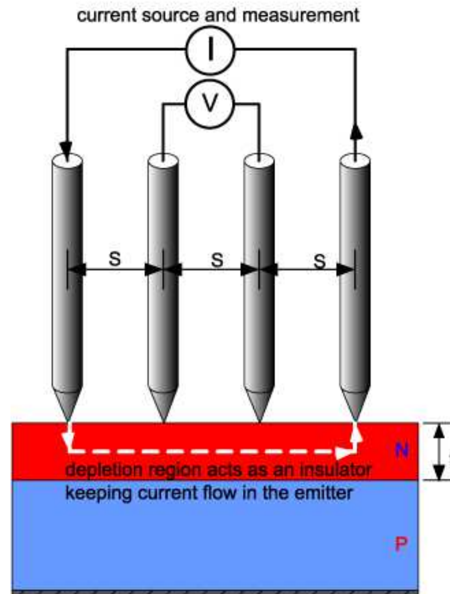

Figure 14 - Scheme of four-point probe measurement for sheet resistance of an emitter [73]

When several measurements are performed in different places of the wafer, this method also allows to evaluate the homogeneity of the doping process.

4.2. Chemical solutions

For the present work three solutions were used:

0.1% HF: composed of 720 mL of deionized water (H_2Odi) and 20 mL fluoridric acid (HF). The wafer is dipped in this solution until its native oxide or its BSG is completely removed, depending if it is a doped or undoped wafer.

Etch-back: composed of 50 mL H_2Odi,500 mL of nitric acid (HNO_3) and 0.5 mL HF. The doped wafer with BRL is dipped in this solution, while the container is bathed in water and ice. The chemical bath lasts for 10 minutes as this solution is used as a weak chemical etching for oxidizing the BRL.

CP4: composed of 350 mL HNO_3, 250 mL of glacial acetic acid (CH_3CO_2H) and 60 mL of HF. The doped wafer with BRL is dipped in this solution, while the container is bathed in water and ice, for a couple of minutes until the BRL is completely removed as this solution is as a strong chemical etching for oxidizing the BRL.

As all three solutions contain HF, plastic bottles must be used. Additionally, before each process the wafers are first dipped in H2Odi and after each process three consecutive cleaning steps with H_2Odi are applied.

4.3. Wafer characteristics

In the following table are presented the characteristics of the wafers used in all the experiments presented in this work.

Semiconductor material	n-type Si
Thickness [μm]	520±10
Resistivity Range [Ω.cm]	1-10
Measured Resistivity [Ω.cm]	4
Measured Intrinsic Doping [cm^{-3}]	$1.1x10^{15}$
Diameter [cm]	10

Table 2 - Silicon wafers properties

4.4. Wafer preprocessing

4.4.1. Cutting

In order to give a best use of the available wafers, and as the lab equipment was better prepared for smaller samples, each wafer was cut in 4 pieces each one being 4 cm long and wide. This cut was done manually with the use of a diamond scribe in order to avoid further contaminations during this process.

4.4.2. Cleaning

Before further processing all wafers were dipped in HF 0.1% for a couple of seconds in order to remove the native oxide. No further chemical cleaning was applied as at this stage, the main focus was performing the emitter formation (doping), rather than optimizing the carrier lifetime of the wafer.

4.5. Wafer post-processing

4.5.1. BSG removal

After the doping process an electrically insulating BSG layer is formed on the wafer's surface [74]. The BSG layer has to be removed in order to perform four-point probe measurements. Therefore, the doped wafers are first dipped in H_2Odi in order to remove possible unreacted BBr_3 and then dipped for 5 minutes in 0.1% HF in order to remove the BSG.

5. Experimental results

5.1. Desirable BBr_3 bubbler temperature range

Two doping processes with identical parameters except for the bubbler temperature were tested in order to know the desirable range of values for this parameter. Both processes conditions are presented in Table 3.

Parameter	4 ºC Process	20 ºC Process
Furnace tube temperature [ºC]	900	
Bubbler temperature [ºC]	4	20
Number of Wafers/Barriers	1/4	
Wafer spacing [mm]	4	
Predeposition/Oxidation Time [min]	30/10	
Predeposition: N_2/BBr_3-N_2/O_2 flow [slm]	2.50/0.08/0.76	
BBr_3 content [%]	0.08	0.18
Oxidation: N_2/O_2 flow [slm]	5.4/1.08	

Table 3 - Doping process conditions, varying only the bubbler temperature

5.1.1. Visual inspection

While for the 4 ºC bubbler temperature process the interior of the furnace tube showed a transparent atmosphere, the increase to 20 ºC lead to the formation of a rather dense white cloud near the furnace inlet.

In terms of wafer appearance after the doping process, in the first case no change was visually identified after the doping process, not even a slight darkening indicating an oxide formation. On the other hand, the second case showed an inhomogeneous coloration due to oxide formation as can be seen in Figure 15. In this and all the remaining figures where doped wafers are presented, the wafers are displayed just as they were placed inside the furnace tube during the doping process.

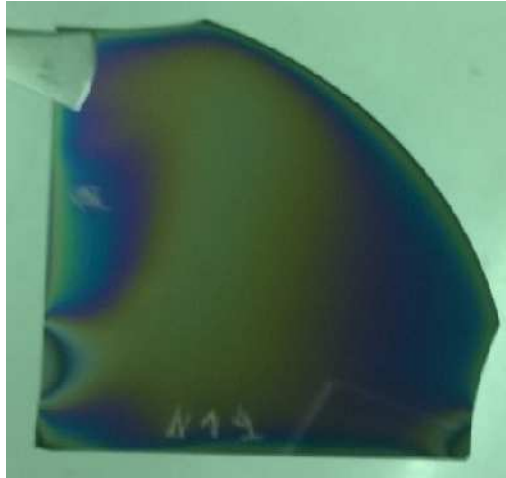

Figure 15 - Oxide coloration after a doping process with a bubbler temperature of 20ºC

5.1.2. Sheet resistance

In order to evaluate the R_{sheet} homogeneity, four probe measurements were made along a vertical line that crossed the wafer's center, measuring in three different points: in the top, center and bottom positions. Even though each batch contained four wafers, the only measurements presented are from a representative wafer per batch complemented by the batch average R_{sheet} ($\overline{R_{sheet}}$) and the batch standard deviation (σ), as each batch showed a similar behavior. The measured R_{sheet} values are presented in Table 4.

Wafer Region		Top			Center			Bottom		
Bubbler Temperature	Side	R_{sheet} [Ω/□]	$\overline{R_{sheet}}$ [Ω/□]	Batch σ [1]	R_{sheet} [Ω/□]	$\overline{R_{sheet}}$ [Ω/□]	Batch σ [1]	R_{sheet} [Ω/□]	$\overline{R_{sheet}}$ [Ω/□]	Batch σ [1]
4 ºC	Inlet	Not doped								
	Exit									
20 ºC	Inlet	82	96	35	Not doped			72	132	52
	Exit	390	293	148				227	270	93

Table 4 - R_{sheet} measurements done in three regions of the wafers, for a process with 4 ºC of bubbler temperature and another with 20 ºC

5.1.3. Discussion

In terms of visual inspection, the formation of a B_2O_3 white cloud related to the increase of the bubbler temperature points to an increased concentration of the doping source and may indicate the presence of a saturated atmosphere which envelopes the wafers, as would be desirable.

Although an inhomogeneous doping was obtained with the bubbler at 20 ºC, it can be concluded that the bubbler needs to be maintained at a temperature considerably higher than 4 ºC as otherwise no doping is achieved. This reasoning is in agreement with Simchi [74] and the bubbler documentation [68] where it is mentioned that the bubbler temperature is usually maintained at 20-25 ºC. In order to better understand the impact of this temperature variation, an increase from 4 ºC to 20 ºC would, theoretically, imply an increase of 125% in BBr_3 concentration inside the furnace tube.

5.2. Bubbler Temperature Sensitivity

Two doping processes with identical parameters were tested in order to evaluate the process repeatability, namely the accuracy of the bubbler temperature control. Additionally, a third process was tested with an increase of 1 ºC in the bubbler temperature. All processes parameters are presented in the following table.

Parameter	Two processes with identical $T_{bubbler}$	Doping process with a 1 ºC increase in $T_{bubbler}$
Furnace tube temperature [ºC]	1000	
Bubbler temperature [ºC]	25	26
Number of Wafers/Barriers	1/4	
Wafer spacing [mm]	4	
Predeposition Time [min]	30	
Predeposition N_2/BBr_3-N_2/O_2 flow [slm]	3.53/0.08/0.16	
BBr_3 content [%]	0.18	

Table 5 - Doping processes conditions.

5.2.1. Visual inspection

While the wafers doped with an identical bubbler temperature showed a relatively similar oxide coloration patterns (Figure 16), even though the wafer geometry may result in slight differences in the doping process, the applied temperature increase resulted in a smaller central white oxide region (Figure 32), which is the thinnest oxide region, being the reduction observed in the inferior region of the wafer. A comparison of oxide thickness profiles along a vertical line that crosses the center of each wafer is presented as well (Graph 26), being possible to observe that the three profiles are relatively similar and no clear change is observed due to the increase in the bubbler temperature.

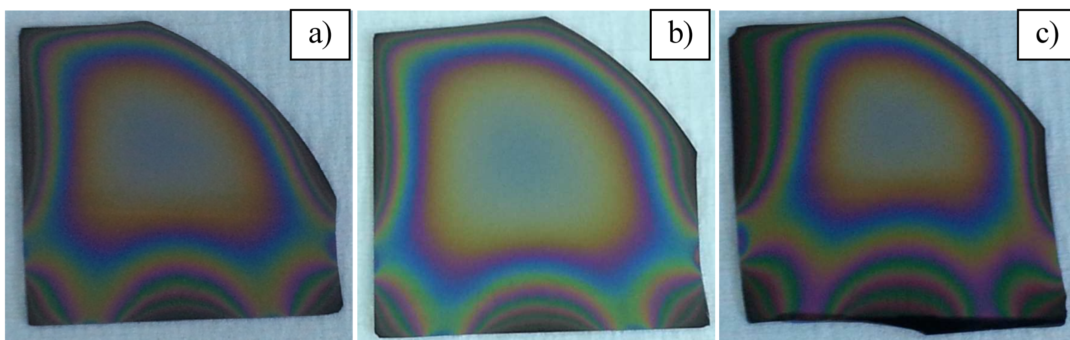

Figure 16 - Oxide coloration after each doping process. For the first two, a) and b), $T_{bubbler}$=25 ºC while for the third, c), $T_{bubbler}$=26 ºC.

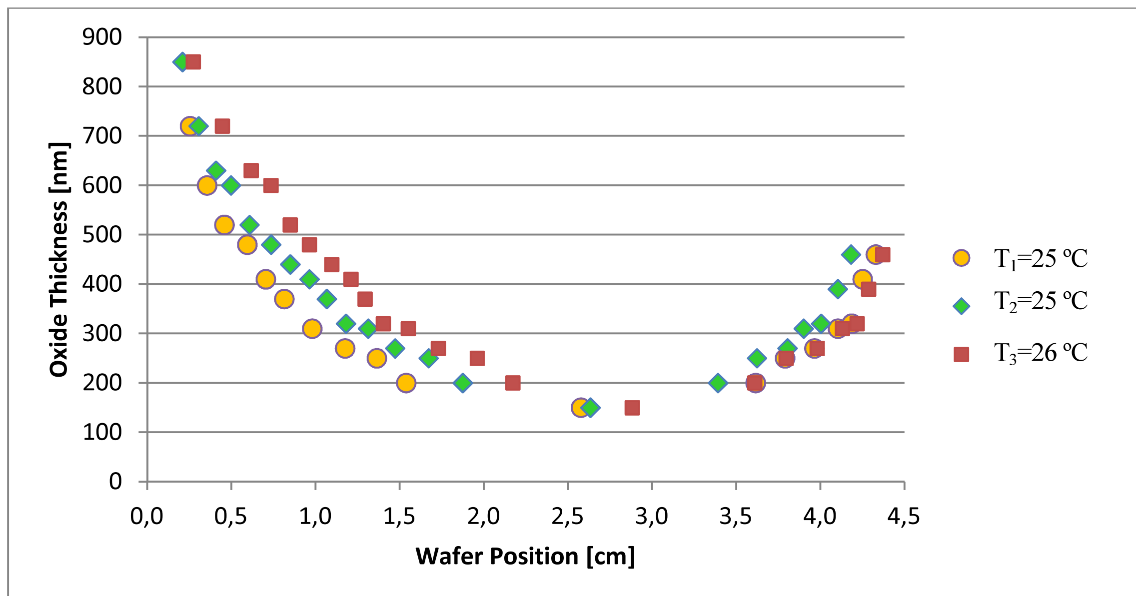

Graph 26 - Oxide thickness profiles, measured in a vertical line that crosses the wafer center.

After an HF dip, in order to remove the superficial BSG, a similar pattern as shown in Figure 17 is visible for all three wafers, where the central region shows to be hydrophobic while the borders are hydrophilic. The wafer respective to Figure 16 b) showed a wider hydrophobic area.

Figure 17 - Doped wafer after an HF dip. It is visible the presence of an hydrophobic behavior in the central region, while the borders are hydrophilic

5.2.2. Sheet resistance

Four probe measurements were made in a vertical line that crossed each wafer's center, measuring five points along such line in order to evaluate the R_{sheet} homogeneity. The values obtained are presented in Graph 27.

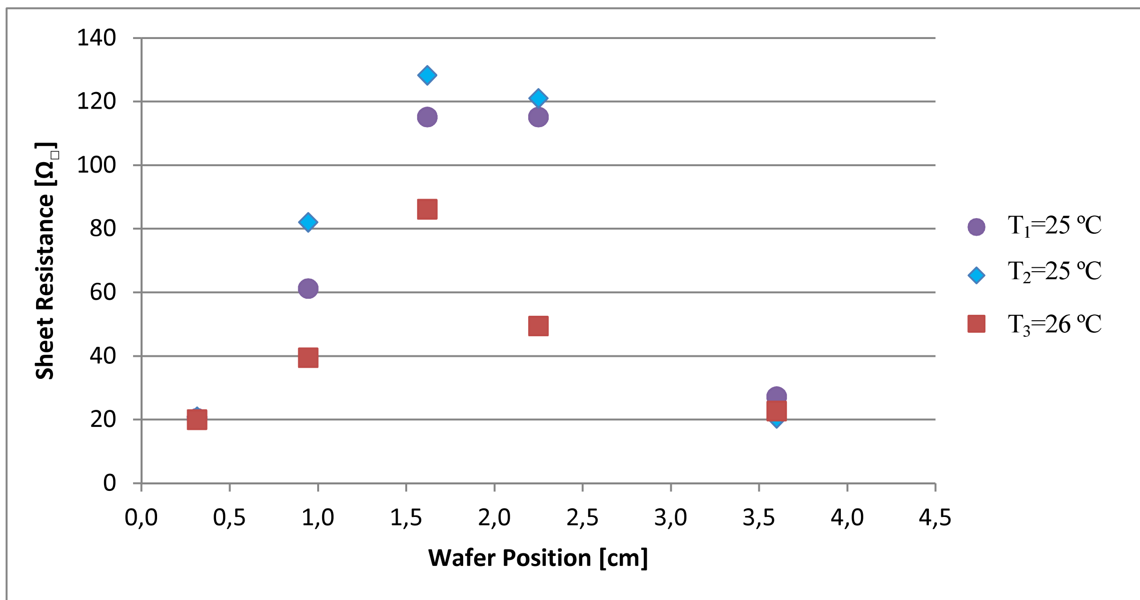

Graph 27 - R_{sheet} measured along a vertical line that crosses the wafer center.

5.2.3. Discussion

In terms of visual inspection, for the two 25 ºC bubbler temperature doped wafers, slight differences could be identified. Such differences can be mainly attributed to the fact that the wafers don't have identical geometries. However, for the 26 ºC doped wafer a smaller white oxide region was observed and it seems that such reduction occurs from the region's lower side.

As the figure displays the wafer as it was placed inside the furnace during the doping process, the fact that such region is the one most apart from the tube center, where a more dense B2O3 cloud was observed, might explain this profile.

From the BRL assessment procedure, it was possible to observe that there was no BRL formation in the wafers' central region. Also these observations seem to correlate with the shape of the thinner white oxide region, as the narrower the white central region of the BSG is the narrower the hydrophobic region is.

From the R_{sheet} measurements it could be observed that, while for the two extreme points (0.32 and 3.6 cm)almost identical R_{sheet} values were obtained, the central points register significant differences in R_{sheet}, especially when the bubbler temperature is higher resulting in a heavier doping. On one hand, the identical points can be related to the significantly thicker oxide that is formed, which may indicate the existence of a higher dopant concentration that could have led to the formation of a BRL. On the other hand, the increase of dopant concentration with the bubbler temperature should be simply due to an increase in boron concentration inside the furnace tube.

It is interesting to note that the impact of changing the bubbler temperature in the R_{sheet} profile is much more evident than the respective oxide thickness profile. This may be explained by the fact that the formed oxide is a mixture of B_2O_3 and SiO_2. While the first is formed from BBr_3 reacting with O_2 and then depositing at the wafer's surface, the second can be formed from the B_2O_3 reacting with the substrate and also from the pure O_2 (that does not react with the BBr_3) reacting with the substrate. By increasing the BBr3 content inside the furnace, it is quite probable that the O_2 that directly reacted with the substrate was then converted into additional B_2O_3, increasing the boron content in the formed oxide and therefore enhancing the wafer doping.

In conclusion, the reasoning that the BRL leads to an enhanced, but also less parameter-dependent, diffusion and therefore SiO_2 formation, as mentioned in State of the Art, seems to be validated. Regarding the bubbler temperature, even though the 26 ºC process lacks repetition in order to validate such results, from Graph 27 it seems that a bubbler temperature of 26 ˚C allows more homogeneous R_{sheet} profiles.

5.3. BBr3-N_2 Gas Flow

Two doping processes with identical parameters except for the BBr_3-N_2 gas flow during the doping process were tested in order to understand the impact of such variation in the resulting R_{sheet} and also to check if a BRL was formed. All processes' parameters are presented in the following table.

Parameters	0.06 slm BBr_3-N_2	0.08 slm BBr_3-N_2
Furnace tube temperature [ºC]	1000	
Bubbler temperature [ºC]	23	
Number of Wafers/Barriers	1/4	
Wafer spacing [mm]	9.0	
Predeposition Time [min]	30	
BBr_3-N_2 flow [slm]	0.06	0.08
N_2/O_2 flow [slm]	1.03/0.37	
BBr_3 content [%]	0.32	0.42

Table 6 - Process conditions, where only the BBr3-N2 flow is varied

5.3.1. Visual inspection

In the process with a BBr_3-N_2 gas flow of 0.06 slm the central region of the wafer acquired a bluish coloration that indicates a thinner oxide, while the borders presented a color pattern similar with the ones obtained in the bubbler temperature study (no record on photograph). On the other hand, the wafer processed with BBr_3-N_2 N_2 gas flow of 0.08 slm had a coloration pattern that indicated that the oxide formed was thicker and that the central region, with a thinner oxide, is more restricted (Figure 18).

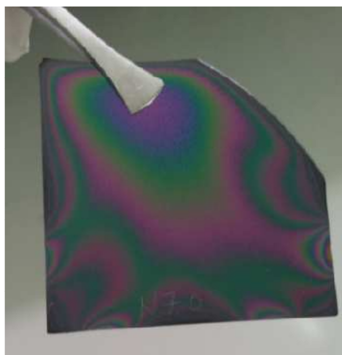

Figure 18 - Resulting oxide coloration pattern for the 0.08 slm BBr3-N_2 gas flow process

After the HF dip, a completely hydrophilic surface was found for the process with the highest BBr3-N_2 gas flow (Figure 19), while for the other process a pattern similar to Figure 17 was observed.

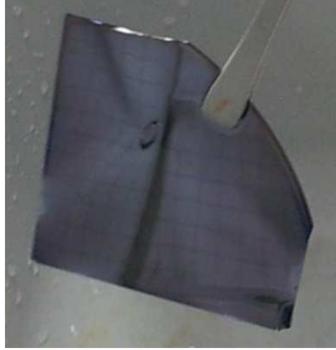

Figure 19 - Doped wafer after an HF dip. The presence of a completely hydrophobic surface is visible

5.3.2. Sheet resistance

Four probe measurements were made in a vertical line that crossed each wafer's center, measuring five points along such line in order to evaluate the R_{sheet} homogeneity. The R_{sheet} values obtained are presented in Graph 28.

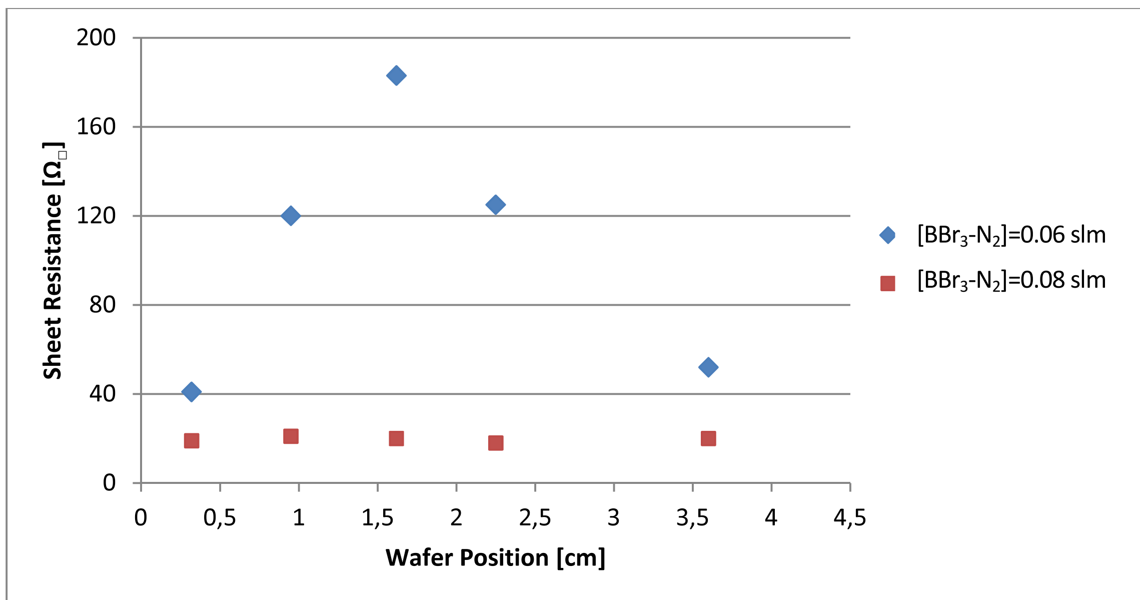

Graph 28 - R_{sheet} along a vertical line that crosses the wafer center for two doping processes where the BBr_3-N_2 is varied

5.3.3. Discussion

Comparing the two processes, it was possible to observe that a considerably less dense B_2O_3 cloud was present inside the furnace during the doping process with 0.06 slm. It was also clear that the variation of the BBr_3-N_2 gas flow had a critical role in the resulting oxide formation even though it is never homogeneous. However, the border regions of the wafer show less significant differences.

From the BRL assessment procedure, it was possible to observe that while the process with lower BBr_3-N_2 gas flow showed a hydrophobic/hydrophilic pattern similar with the ones presented in the previous topic, while the process with higher BBr_3-N_2 gas flow showed a BRL that covered the whole wafer surface.

On the other hand, R_{sheet} measurements seem to agree with the previously mentioned observations. A significantly weaker doping was obtained in the central region of the wafer for the lower BBr_3-N_2 gas flow while near the borders the change is less significant. It is also possible to observe that the wafer with the thicker oxide, despite its thickness inhomogeneity, shows quite a homogeneous R_{sheet} across the wafer. From this observations, it seems that for thicker oxides a BRL is formed and, consequently, the doping process is less sensible to external parameters as the dopant source can be considered infinite.

5.4. Nitrogen Flow

After having obtained a doping process where in the wafer‘s central region no BRL was formed (the process with 4.0 mm wafer spacing, shown in the previous section), three other doping processes with identical parameters except the N_2 flow were tested in order to understand the impact of the variation of the N_2 flow in the BRL area, and in the R_{sheet} throughout the wafer, as the N_2 not only dilutes the doping atmosphere but also leads to a faster gas flow. All processes parameters are presented in the following table.

Parameters	3.52 slm N_2	5.92 slm N_2	8.82 slm N_2
Furnace tube temperature [ºC]	1000		
Bubbler temperature [ºC]	25		
Number of Wafers/Barriers	1/4		
Wafer spacing [mm]	4.0		
Predeposition Time [min]	30		
N_2flow [slm]	3.53	5.92	8.82
BBr_3-N_2/O_2 flow [slm]	0.08/0.16		
BBr_3 content [%]	0.18	0.11	0.07

Table 7 - Doping process conditions, where only the N2 flow was varied

5.4.1. Visual inspection

A clear pattern of the broadening of the central region, where the oxide is thinner, is shown in both a vertical and horizontal direction (Figure 20) as the N_2 flow is increased while for the upper borders of the wafer, similar color patterns can be observed. For the highest N_2 flow tested, even a change of coloration in the central region was observed. The doped wafers' oxide thickness profiles along a vertical line that crosses each wafer's center are presented in Graph 29.

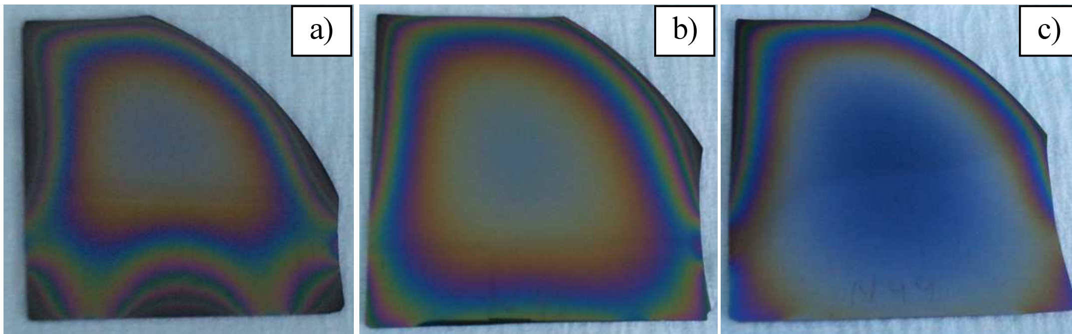

Figure 20 - Obtained oxide coloration after each doping process. The N_2 flows are 3.53, 5.92 and 8.82 slm respectively

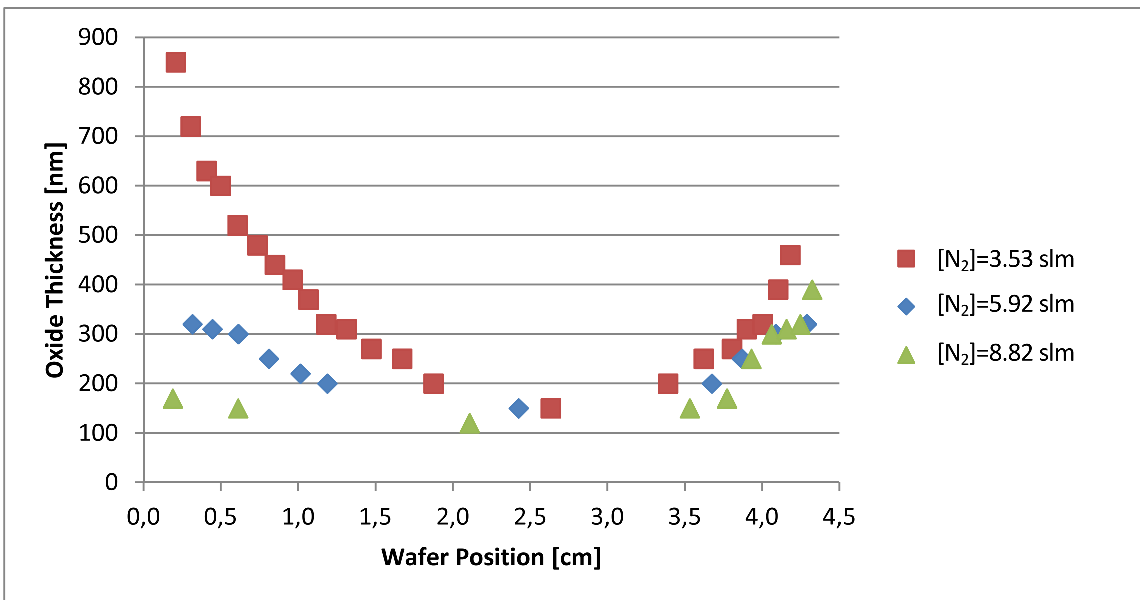

Graph 29 - Visually assessed oxide thickness profiles along a vertical line that crosses the wafer center for different N_2 flows

After an HF dip, in order to remove the superficial BSG, a similar pattern as the one shown in Figure 17 was obtained, where the central region shows to be hydrophobic while the borders are hydrophilic. However, the higher is the N_2 gas flow, the wider is the hydrophobic area, which is mainly extending to the wafer's lower region. On Figure 21 an example of this behavior, respective to the 8.82 slm N_2 gas flow process, can be observed.

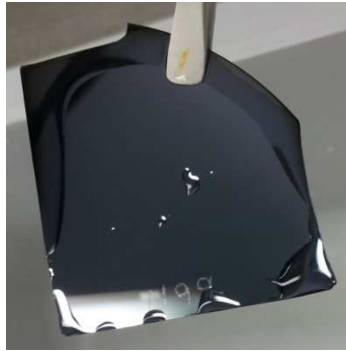

Figure 21 - Doped wafer after an HF dip. The presence of hydrophilic behavior in the center and lower regions is visible, while the borders are hydrophobic.

5.4.2. Sheet resistance

Four probe measurements were made in a vertical line that crossed each wafer's center, measuring five points along such line in order to evaluate the R_{sheet} homogeneity. The R_{sheet} values obtained are presented in Graph 30.

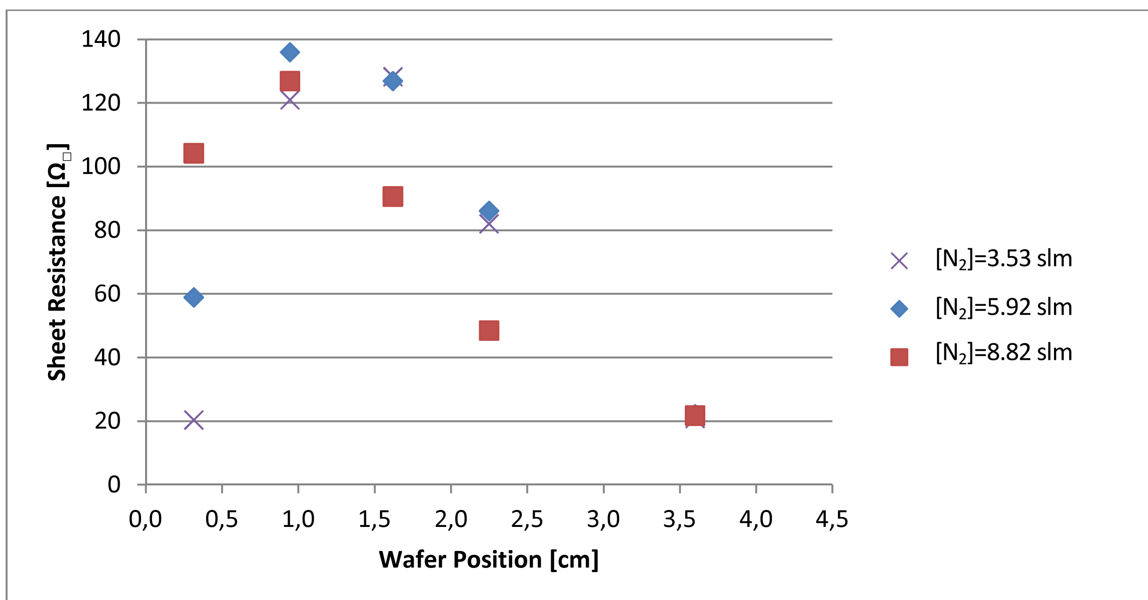

Graph 30 - R_{sheet} measured along a vertical line that crosses the wafer center for the three doping processes where the N_2 flow is varied.

5.4.3. Discussion

In terms of visual inspection, the broadening of the central region and even the change of that region color, indicating a thinner oxide, with the increasing N_2 flow can be attributed to the presence of a more diluted atmosphere both it in terms of dopant source or O_2 (both favor SiO_2 formation). From the previous figures it was also visible that the lower part of the wafer is more affected then the center. Finally, this behavior is also observed in the BRL as the BRL covered area seems to be reduce with the increasing N_2, mainly in the region where the oxide gets thinner.

In terms of R_{sheet} measurements, several things can be inferred from Graph 30. First, the measurements made near the lower border show an increasing R_{sheet}, meaning a decreasing doping, as the N_2 flow increases. These measurements agree with the changes observed in terms of oxide coloration and oxide thickness profiles, as lighter doping levels may originate thinner oxides.

Additionally, near the upper border the measured R_{sheet} is practically identical for all cases, a result that aggres with the low variation in the observed oxide coloration and the thickness profile obtained. The reason for such results may be explained by the fact that the B_2O_3 flow (seen as a white cloud) is centered with the furnace tube while the wafers are positioned in the lower half of tube, meaning that the dopant gas contaminates preferably the upper part of the wafer.

Another trend that can be identified in the measurements made in the central part of the wafers is that the doping level increases with the N_2 flow. As the doping atmosphere is more diluted and the oxide colorations do not seem to indicate this trend, a repetition of these processes should be done and if such trend persists, the use of 4 inch wafers should be considered in order to guarantee that the gas flows homogeneously along the wafer, possibly even allowing a more uniform variation of the different parameters.

5.5. Wafer spacing in the wafer support structure during the doping process

In order to determine the impact of the wafers spacing, three doping processes where only this parameter was varied were tested in order to understand the impact in the R_{sheet} and also in the BRL formation. All processes' parameters are presented in the following table.

Parameters	4.0 mm spacing	6.5 mm spacing	9.0 mm spacing
Furnace tube temperature [˚C]	1000		
Bubbler temperature [˚C]	25		
Number of Wafers/Barriers	1/4		
Wafer spacing [mm]	4.0	6.5	9.0
Predeposition Time [min]	30		
N_2/ BBr_3-N_2/O_2 flow [slm]	3.53/0.08/0.16		
BBr_3 content [%]	0.18		

Table 8 - Doping process conditions, where only the wafer spacing was varied

5.5.1. Visual inspection

All wafers showed significantly different oxide coloration patterns, mainly in the upper central region while the border colors seem to get thicker, as can be seen in Figure 22. The doped wafers oxide thickness' profiles along a vertical line that crosses each wafers center is presented in Graph 31.

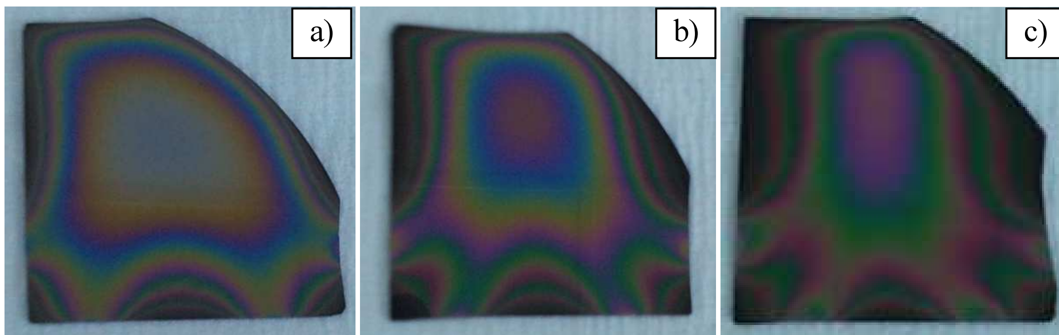

*Figure 22 - Oxide coloration after each doping process.
The wafer spacings are 4.0, 6.5 and 9.0 mm respectively*

After the HF dip, while the first wafer showed a pattern similar to the one presented in Figure 17, the two other processes presented a completely hydrophilic surface such as the one presented in Figure 19.

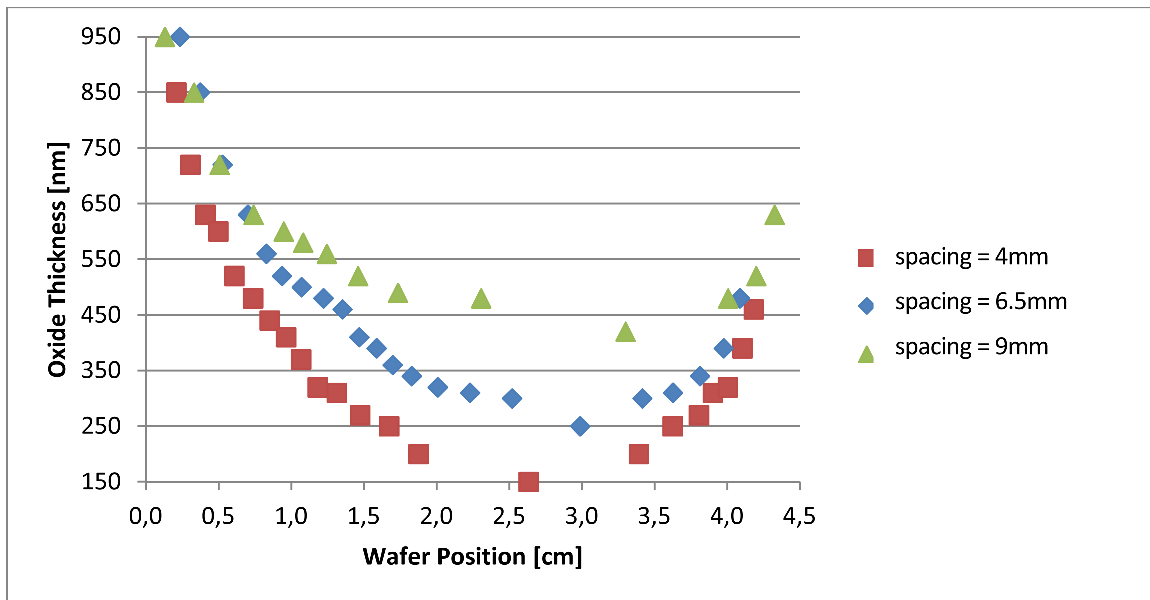

Graph 31 - Visually assessed oxide thickness profiles along a vertical line that crosses the wafer center for different wafer spacings

5.5.2. Sheet resistance

Four probe measurements were made in a vertical line that crossed each wafer's center, measuring five points along such line in order to evaluate the R_{sheet} in different positions. The R_{sheet} values obtained are presented in Graph 32.

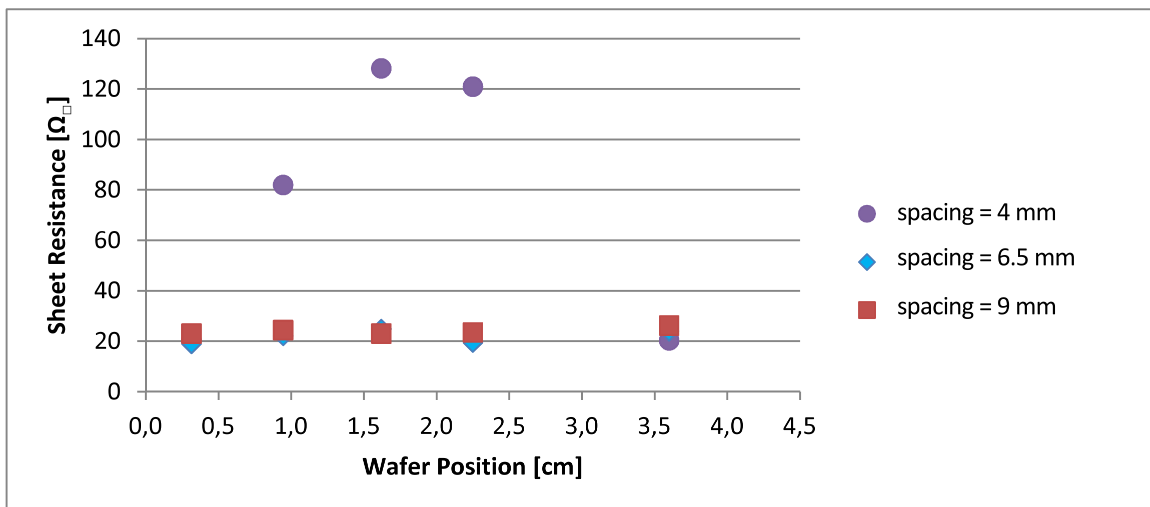

Graph 32 - Measured R_{sheet} along a vertical line that crosses the wafer center for three doping processes where the wafer spacing is varied

5.5.3. Discussion

In terms of visual inspection the increase in the wafers spacing lead to an oxide coloration that indicates the formation of thicker oxides in the wafer central region, while the border regions are similar for all processes. This reasoning is in agreement with the presented oxide thickness profiles. It can also be observed that as the spacing increases not only the thinnest oxide region starts to move to the upper part of the wafer but also gets smaller.

In terms of BRL assessment, the obtained results seem to support the idea that, for similar furnace conditions, the presence of such layer is related to the resulting oxide as it appears to fully cover the wafers' surface when thicker oxides are formed.

From the R_{sheet} measurements it can be observed, that for all three cases the two extreme measured points (0.32 and 3.6 cm) show almost identical R_{sheet} but for more central positions a clear difference can be identified between a 4.5 mm wafer spacing and the remaining spacing values, while those cases show very similar R_{sheet} profiles between 19-26 Ω/□, which possibly can be related to the presence of a BRL, as mentioned in previous topics.

The resemblance between the R_{sheet} curves obtained for a wafer spacing of 6.5 cm and 9 cm suggests that distances between wafers greater or equal to 6.5 cm the distance between wafers do not affect the efficiency of the doping process.

The cases studied show a qualitative correlation between doping level and formed oxide thickness, since only when a wafer has an oxide thickness of at least 250 nm a homogeneous R_{sheet} is obtained.. This fact can be attributed to the formation of a BRL in the whole wafer for the 6.5 cm and 9 cm cases.

These results may be explained by the fact that a reduced spacing between wafers greatly constrains the contamination of its surface by the doping gas, creating "dead zones" on the central region of the furnace. Further, the fact that the wafer borders are less affected by the shielding effect of the other wafers might help explaining the reduced or no impact verified in these regions in terms of resulting oxides and doping levels when wafers' distance is varied.

Another observation that might corroborate this reasoning is that it was found that when a wafer was misplaced in the boat, the wafer surface that is more exposed to the gas flow (or, in other words, that does not face the next wafer) ends up showing thicker oxides.

5.6. Predeposition Time

After having obtained a doping process where in a central region no BRL was formed (with 4.0 mm spacing), another doping process with identical parameters except the predeposition time was tested in order to understand the impact of this parameter. All processes parameters are presented in the following table.

Parameters	15 min	30 min
Furnace tube temperature [ºC]	1000	
Bubbler temperature [ºC]	25	
Number of Wafers/Barriers	1/4	
Wafer spacing [mm]	4.0	
Predeposition Time [min]	15	30
N_2/ BBr_3-N_2/O_2 gas flow [slm]	3.53/0.16/0.08	
BBr_3 content [%]	0.18	

Table 9 - Doping process conditions

5.6.1. Visual inspection

It can be observed in Figure 23 that increasing the predeposition step duration leads to some changes in the oxide coloration. At the first, it is visible that the center acquires a more yellowish coloration indicating a slightly thicker oxide. However, when evaluating the number of color transitions at the wafers' borders it is clear that when the deposition time this number increases, indicating as well the formation of thicker oxides. The oxide thickness profiles along a vertical line that crosses each wafer’s center is presented in Graph 33, making it possible to verify that the main change was at the borders.

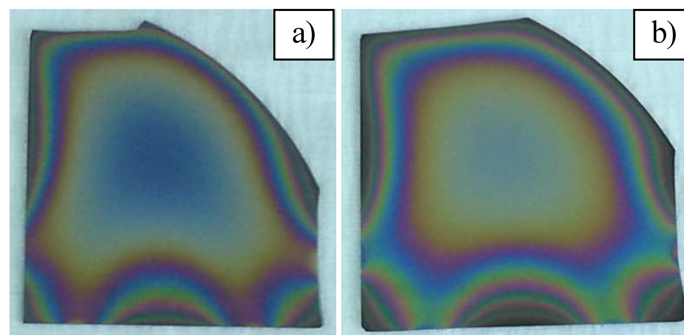

Figure 23 - Oxide coloration after each doping process. The predeposition duration is 15 and 30 min respectively.

After the HF dip, for both cases, a pattern similar to Figure 17 was observed. However, increasing the predeposition time leads to a slightly narrower hydrophobic surface.

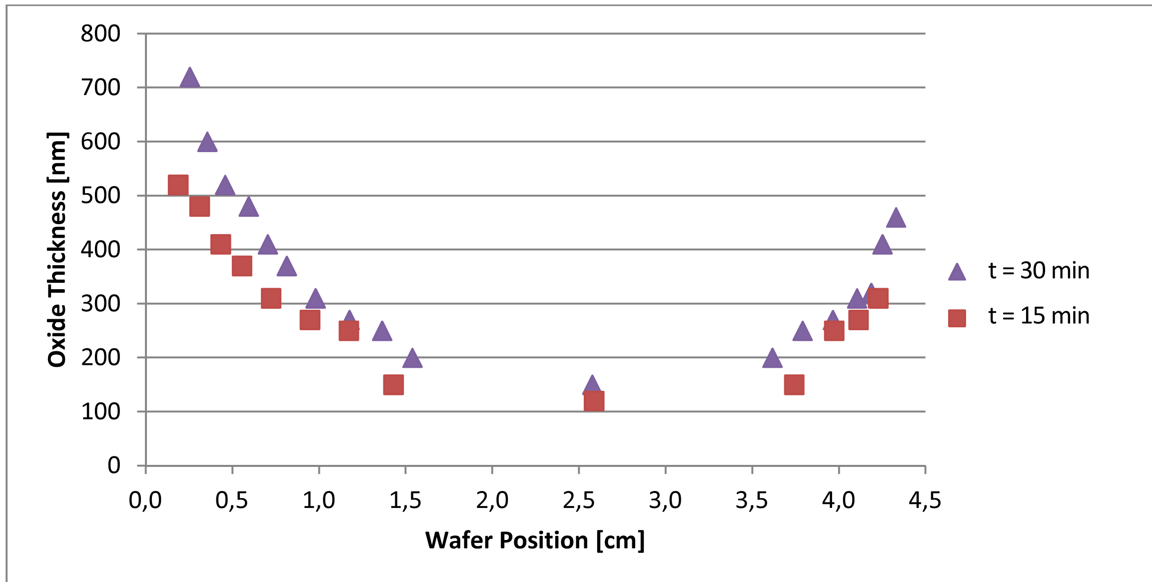

Graph 33 - Visually assessed oxide thickness profiles along a vertical line that crosses the wafer center for different predeposition times.

5.6.2. Sheet resistance

Four probe measurements were made in a vertical line that crossed each wafer's center, measuring five points along such line in order to evaluate the R_{sheet} homogeneity. The R_{sheet} values obtained are presented in Graph 34.

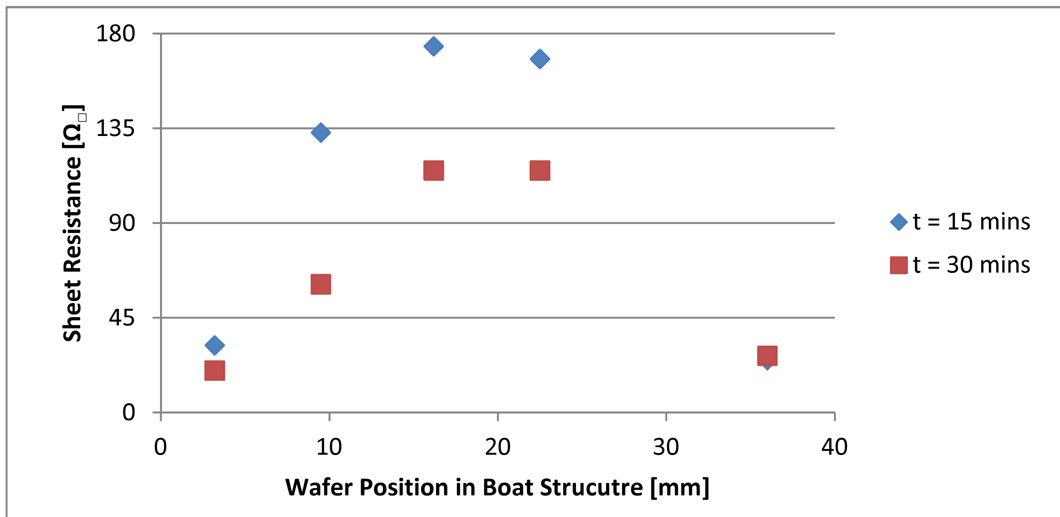

Graph 34 - R_{sheet} measured along a vertical line that crosses the wafer center for two doping processes analyzed

5.6.3. Discussion

In terms of visual inspection, the center coloration of both wafers , as expected, showed that a longer predeposition time leads to a thicker central region oxide; for 15 minutes a minimum oxide thickness of 120 nm was obtained, while for 30 minutes the minimum was 150 nm. However, doubling the predeposition step duration led in general to a small impact in terms of oxide thickening, being the lower border of the wafer the exception for which the thickness increased 26%.

In State of the Art it is mentioned that during a predeposition step the BSG/BRL growth is homogeneous up to a certain point until the process starts to be sensible to the external parameters. Considering that, in terms of BRL coverage, doubling the predeposition time did not have significant consequences (only a slight increase of the thickness), it would be interesting to reduce the furnace temperature in order to get a better understanding of the BRL formation and its consequences on the oxide/doping homogeneity.

In terms of R_{sheet} measurements, several observations can be made from Graph 34. First, and in accordance with the visual observation, the central regions' showed a considerably lower R_{sheet}, signal of a heavier doping level, when the predeposition time was increased, while the border regions showed no significant change in terms of measured R_{sheet}.

One possible explanation for the distinct behavior in the border regions is that after 15 minutes the solid solubility limit could have already been achieved and therefore no further dopant incorporation would have occurred after that period.

5.7. Batch Process Homogeneity

After testing the different processes mentioned in section 3.7.2.3, the one with the highest N_2 flow (Table 10, Figure 24 and Graph 35) was tested in batch conditions; doping several wafers in a single process.

Parameters	Single-wafer process
Furnace tube temperature [˚C]	1000
Bubbler temperature [˚C]	25
Number of Wafers/Barriers	1/4
Wafer spacing [mm]	4.0
Predeposition Time [min]	30
N_2/ BBr_3-N_2/O_2 flow [slm]	8.82/0.08/0.16
BBr_3 content [%]	0.07

Table 10 - Doping process conditions of the single-wafer process selected to be tested in batch conditions

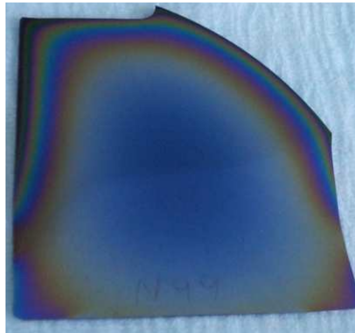

Figure 24 - Reference single-wafer process, with a N_2 flow of 8.82 slm identical to Figure 20 c)

This process was defined as a reference because it led to the formation of a wider white/bluish region, where the oxide thickness was homogeneous and no BRL was formed (avoiding the need for a BRL removal step on the fabrication chain), and a lightly doped emitter was obtained. Therefore all the conditions shown in Table 10 were maintained except the number of wafers used which increased from 1 to 7.

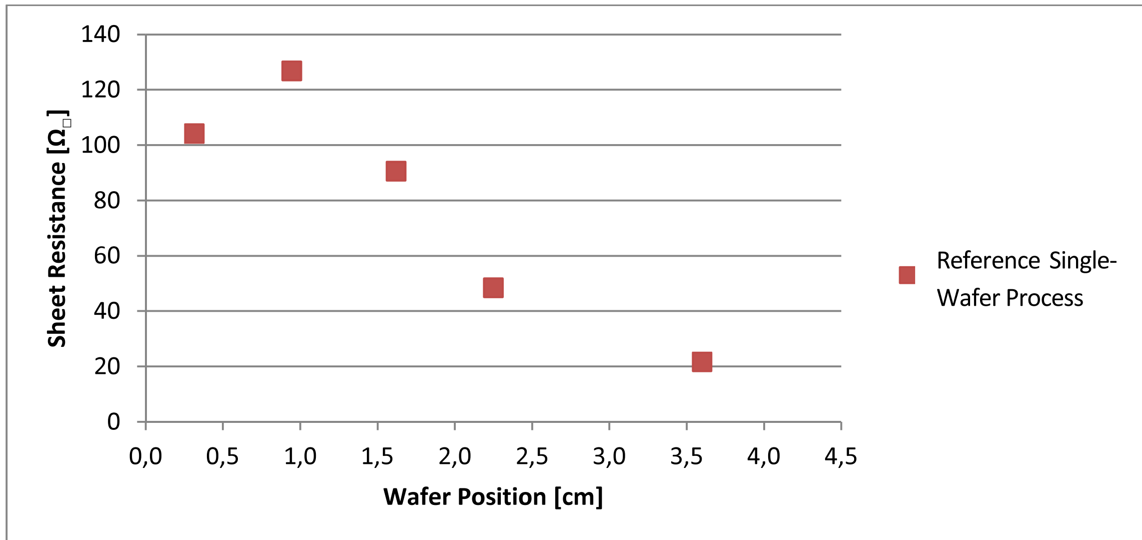

Graph 35 - R_{sheet} measured along a vertical line that crosses the wafer center for the defined single-wafer reference process

5.7.1. Visual inspection

From Figures Figure 25 and Figure 26, which represent both sides of all the wafers doped in the process, it can be observed that not only the resulting oxide coloration is not similar to the one obtained in the single-wafer process but also practically no coloration is shown in the central regions of the wafers except for the first and the last one. Finally, in the case of the first wafer its front shows a stronger coloration than its back while for the last wafer the reverse applies. It should be noted that there is one less wafer in the second photograph as between experiments one of the center wafers got damaged.

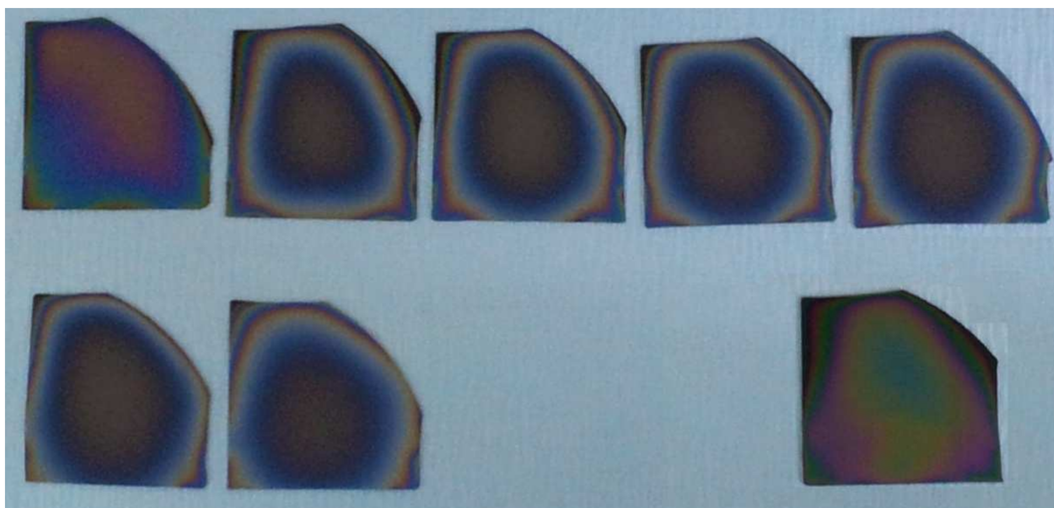

Figure 25 - Oxide coloration, on the side turned to the gas inlet,.

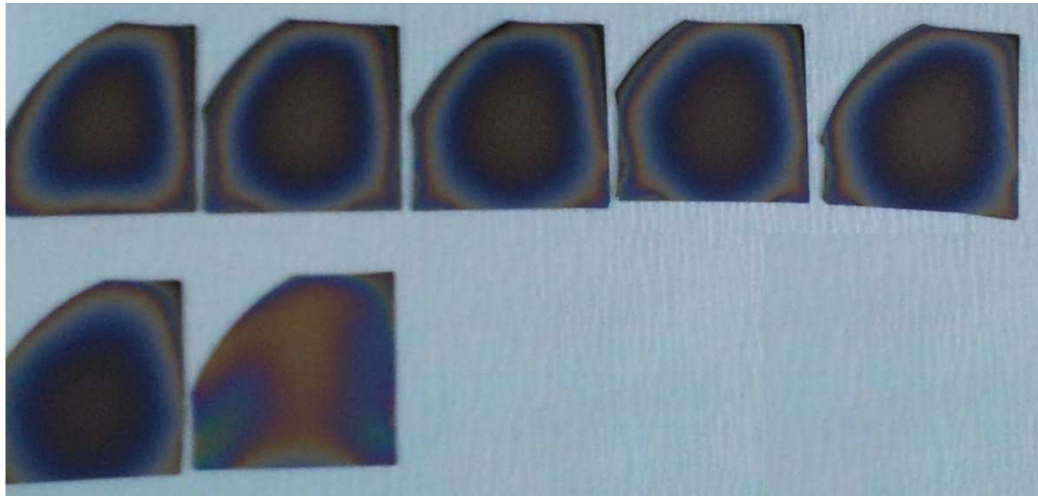

Figure 26 - Oxide coloration, on the side turned to the furnace exit

After the HF dip, for the single-process case a pattern similar to Figure 21 where the area covered by the BRL was reduced and was mostly placed on the upper region borders, while in the batch process case the first and last wafers showed a surface fully covered by BRL and all the other wafers had a residual area near the borders covered by a BRL.

5.7.2. Sheet Resistance

As the batch process resulted in an inhomogeneous wafer to wafer oxide formation, four probe measurements were only made in the center of each wafer. The R_{sheet} values obtained are presented in Graph 36.

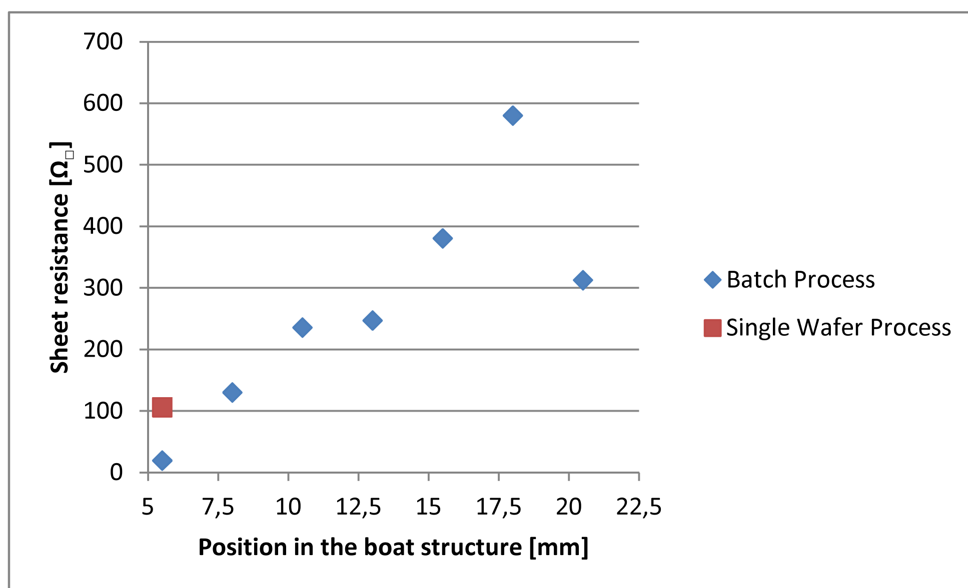

Graph 36 - R_{sheet} measured at each wafer's center

5.7.3. Discussion

From the visual inspection, it is clear that the results obtained in the single wafer process are not valid for a batch process made in similar conditions. Additionally, as only the first and last wafers (the ones nearer to the barriers) showed significant coloration in their central regions (signal of the presence of oxide), it is quite probable that the use of overdoped wafers as barriers had only a local impact in the doping process.

The R_{sheet} measurements not only indicate that the gaseous doping source was insufficient for that many wafers as the doping decreases as the distance to the gas inlet increases. In respect to the overdoped barriers, these measurements clearly support their exclusively local impact as the Rsheet keeps increasing (meaning less doping) as the distance between the wafer and the first barrier increases until a sudden decrease was verified for the wafer that was closest to the last barrier. Nevertheless, it important to mention that neither the first or last wafers showed a similar R_{sheet} as in the single wafer process, suggesting that the flow dynamics is very different for the two experiments.

From these results several conclusions can be drawn: while the use of such barriers is common in doping processes, as it is considered to contribute to the creation of a generally saturated doping atmosphere, for the tested process a very local effect was observed; single wafer experiments results are not valid references for batch processes made in conditions, at least when overdoped barriers are used. The use of an alternating pair undoped/overdoped barrier is a possible way to improve the homogeneity of this doping process.

5.8. Overdoped Barriers Removal

In order to better understand the role of the overdoped barriers on the doping process, a single wafer process where the overdoped barriers were replaced by undoped ones was tested. However, the process conditions were chosen so that a thicker oxide layer would be formed in the wafer borders and the usual thinner oxide in the center.

Parameters	Overdoped barriers	Undoped barriers
Furnace tube temperature [˚C]	1000	
Bubbler temperature [˚C]	25	
Type of barriers	Overdoped	Undoped
Wafer spacing [mm]	4.0	
Predeposition Time [min]	30	
N_2/ BBr_3-N_2/O_2 flow [slm]	3.53/0.08/0.16	
BBr_3 content [%]	0.18	

Table 11 - Doping process conditions, for the processes under test

5.8.1. Visual inspection

From Figure 27 it becomes clear that the use of overdoped barriers greatly influences the doping process. While with the wafer doped with the overdoped barriers shows the typical pattern of a thick oxide in the borders, when using undoped barriers a slight coloration in the upper region and almost no coloration in the center and lower regions of the wafer can be observed.

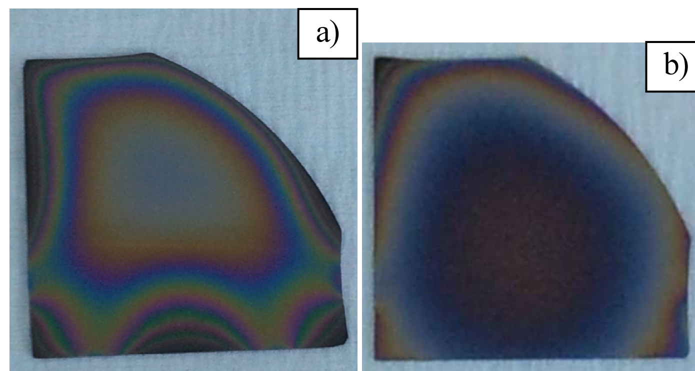

Figure 27 - Oxide coloration after the doping process. A overdoped and undoped barriers are used, respectively

After an HF dip, while the first case presented a considerable area covered by a BRL, the process with undoped barriers showed a residual BRL coverage and mostly on the upper region borders.

5.8.2. Sheet Resistance

Four probe measurements were made in a vertical line that crossed each wafer's center, measuring five points along such line in order to evaluate the R_{sheet} homogeneity. The R_{sheet} values obtained are presented in Graph 37.

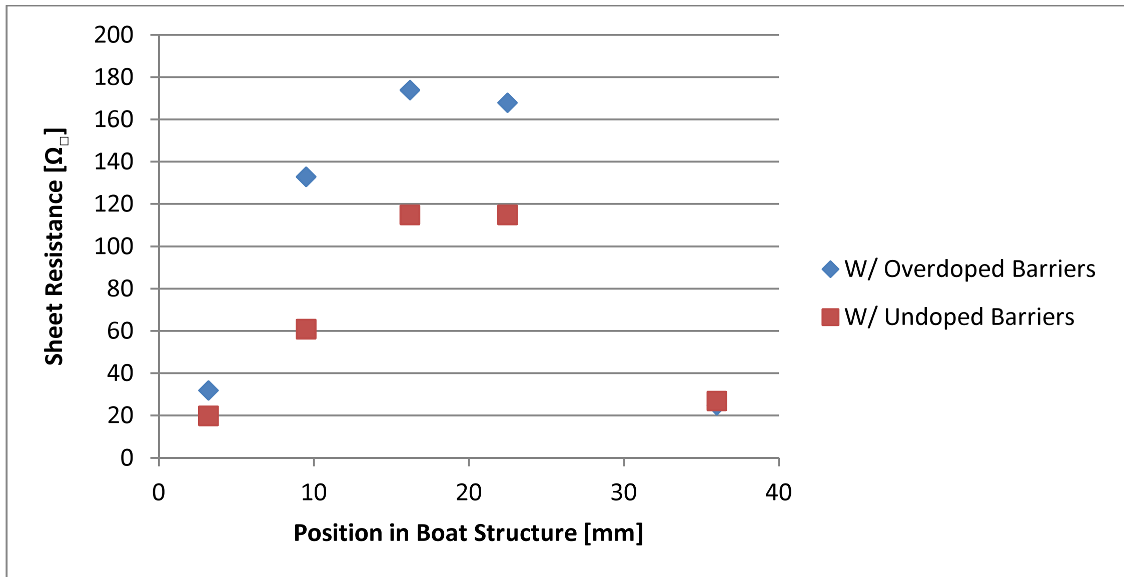

Graph 37 - R_{sheet} measured along a vertical line that crosses the wafer center for the two doping processes analyzed.

5.8.3. Discussion

From the visual inspection and the R_{sheet} measurements it seems clear that the presence of overdoped barriers influences both oxide formation and wafer doping, which are strongly correlated. It can also be observed that the center region is the most affected, possibly due to the fact that the B_2O_3 gas flow is centered with the furnace tube axis, while the wafers are in the lower part of the tube. Resulting from this that the contribution of the overdoped barriers is more crucial to the doping level in the center of the wafer than on the borders.

5.9. Batch Process Optimization

After the removal of the overdoped barriers, several processes were tested in order to obtain a homogeneous batch (wafer to wafer) doping. The inhomogeneous batch process presented previously is considered as a starting situation. The conditions used in the different processes are presented in the following table.

Parameters	Overdoped barriers	Undoped barriers and higher spacing	Undoped barriers + low N_2 + high $T_{bubbler}$
Furnace tube temperature [ºC]	1000		
Bubbler temperature [ºC]	25		32
Type of barriers	Overdoped	Undoped	
Wafer spacing [mm]	4.0	6.5	
Predeposition Time [min]	30		
N_2/ BBr_3-N_2/O_2 flow [slm]	8.83/0.08/0.16		3.53/0.08/0.16
BBr_3 content [%]	0.07		0.25

Table 12 - Doping processing conditions, where an homogeneous batch process was sought

5.9.1. Visual inspection

From Figure 28 and Figure 29, it can be observed that when the spacing between wafers is increased and the barriers are removed a stronger coloration appears in the border regions. However, even though the overdoped barriers had been replaced by undoped wafers, a different and less homogeneous pattern appeared in the first and last wafers. For all these wafers, a bigger BRL coverage was obtained at least at the wafers borders, while for the first wafer a fully covering BRL was obtained.

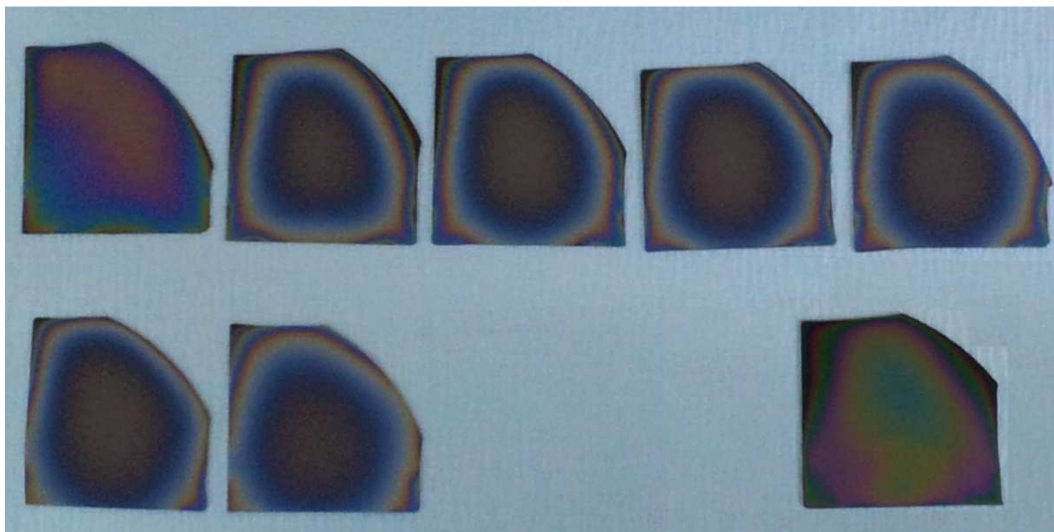

Figure 28 - Oxide coloration for the reference batch process

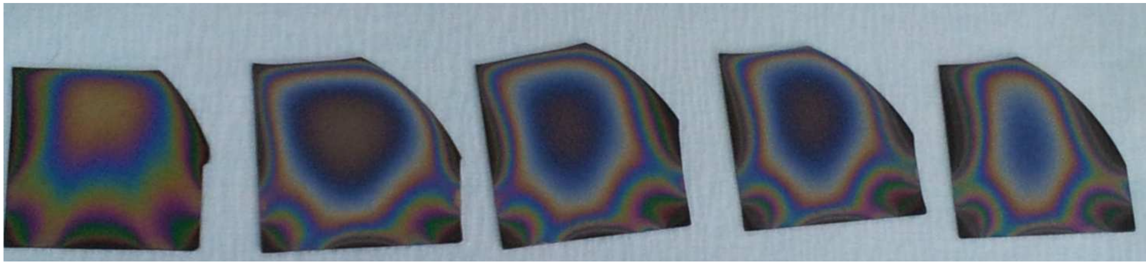

Figure 29 - Oxide coloration with higher spacing and undoped barriers

For the second test, in order to create a more saturated doping atmosphere the bubbler temperature was increased to 32°C as the BBr_3-N_2 gas flow is already at its limit, and the N_2 flow was reduced. From Figure 30, it is clear that a thicker oxide was formed although the wafer to wafer homogeneity is modest. For all these wafers a full coverage of the surface by the BRL was obtained.

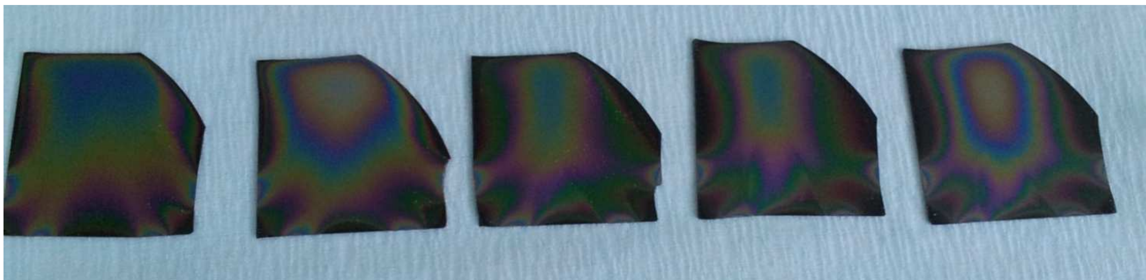

Figure 30 - Oxide coloration with higher bubbler temperature and lower N_2 flux

5.9.2. Sheet Resistance

Since the main priority was to obtain an efficient doping process with a good wafer to wafer homogeneity, the R_{sheet} was only measured at the wafers' center. The measured values obtained for the various processes are presented in Graph 38.

The intended wafer to wafer R_{sheet} homogeneity seems to be achieved for the last process, nevertheless it can be seen that the first wafer shows a R_{sheet} 192% higher than the remaining wafers. Therefore, that wafer should be ignored and possibly replaced by a barrier. More four probe measurements were done to three sequential wafers of the last process in order to also evaluate the homogeneity in each wafer. Similarly to previous experiments, the measurements were done in a vertical line that crossed each wafer's center, measuring five points along such line. The obtained values are presented in Graph 39.

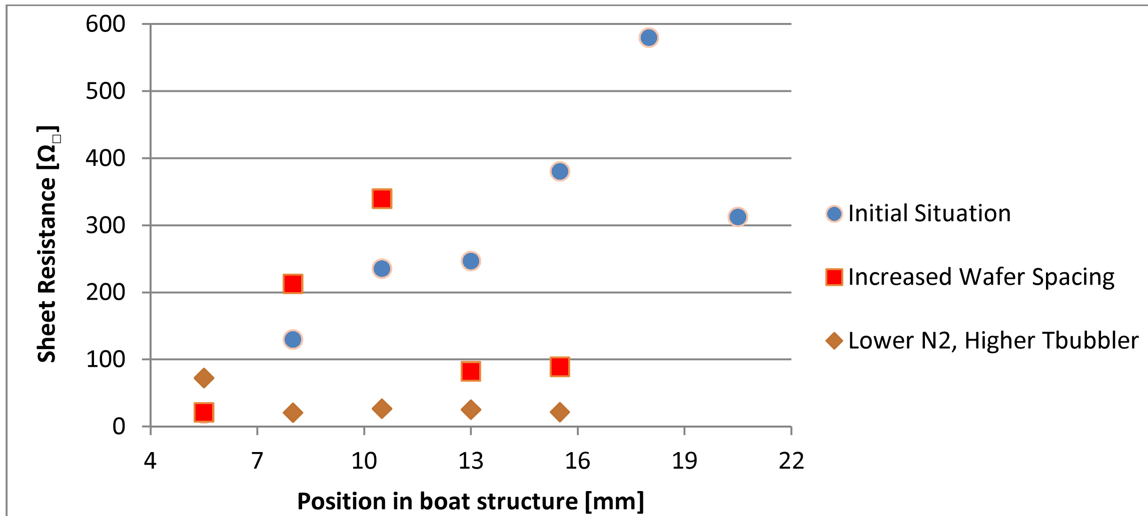

Graph 38 - R_{sheet} measured at each wafer's center for the three tested processes

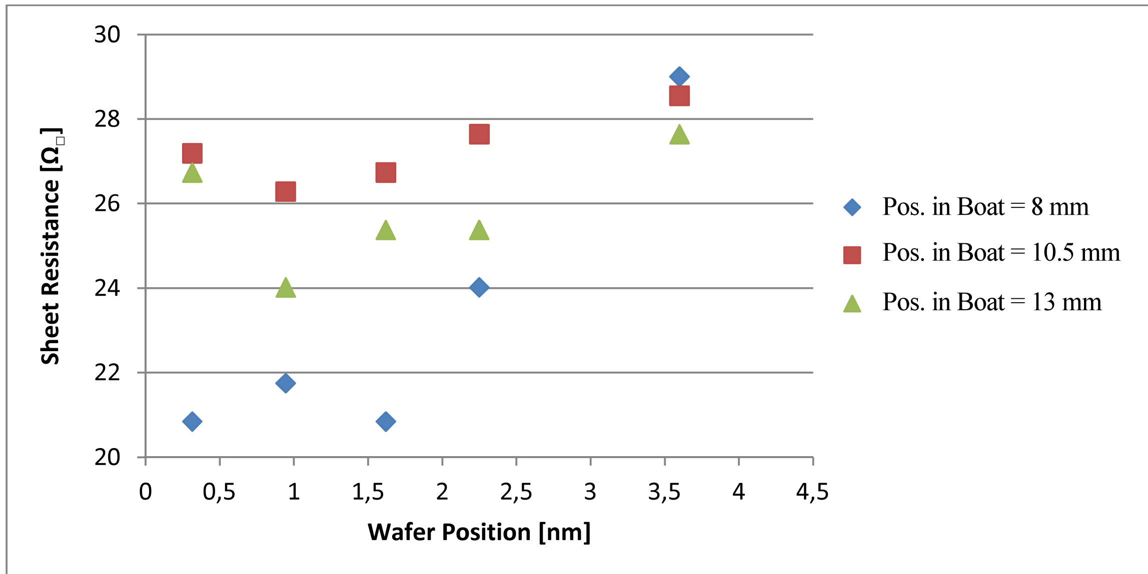

Graph 39 -R_{sheet} measured along a vertical line that crosses the wafer's center for three wafers doped in the optimized batch process

5.9.3. Discussion

From the visual inspection it can be observed that in order to obtain a considerable oxide coloration (that corresponds to a significant oxide thickness) the gas flow circulation was augmented by increasing the wafer spacing; and the dopant concentration on the furnace atmosphere was increased, by reducing the N_2 flow and increasing the bubbler temperature.

R_{sheet} measurements showed that even though the wafer to wafer (and in each wafer) oxide coloration homogeneity is moderate, with the exception of the first wafer the wafer to wafer doping level homogeneity is remarkable, which is mostly due to the presence of a fully covering BRL. Therefore, the replacement of the first wafer by a barrier and testing a batch process with a higher number of wafers, while maintaining their spacing, should be considered.

5.10. Predeposition + Thermal Dry Oxidation Process

A doping process consisting in a predeposition step followed by an in-situ oxidation was tested in order to inspect the presence of a BRL and evaluate the resulting doping level. The process parameters are presented in the following table.

Parameters	No Oxidation	Oxidation with "high N_2" + O_2	Oxidation with "low N_2" + O_2	Oxidation with O_2
Furnace tube temperature [˚C]	1000			
Bubbler temperature [˚C]	23			
Number of Wafers/Barriers	1/4			
Wafer spacing [mm]	9.0			
Predeposition Time [min]	30			
N_2/ BBr_3-N_2/O_2 flow [slm]	1.03/0.08/0.16			
BBr_3 content [%]	0.49			
Dry Oxidation Time [min]	No oxidation	20		
N_2 flow [slm]		10.50	1.03	0
O_2 flow [slm]		1.01	2.04	

Table 13 - Doping process conditions for different processes tested.

5.10.1. Visual Inspection

Despite not having the wafers photos for these processes, no changes were verified for the oxidation with a flux of 10.50 slm of N_2 when compared with a "no oxidation" process. When the N_2 flow was decreased and the O_2 introduced, even though the doped wafers showed the same color pattern, a slight darkening of the surface was observed. In terms of BRL for the first two cases, after HF dip, the whole wafer was covered by a BRL, while in the last two the BRL was only partially removed, mostly on the wafer's center, being a more complete removal observed for the last process.

5.10.2. Sheet Resistance

Four probe measurements were made in a vertical line that crossed each wafer's center, measuring five points along such line in order to evaluate the R_{sheet} homogeneity. The R_{sheet} values obtained are presented in Graph 16.

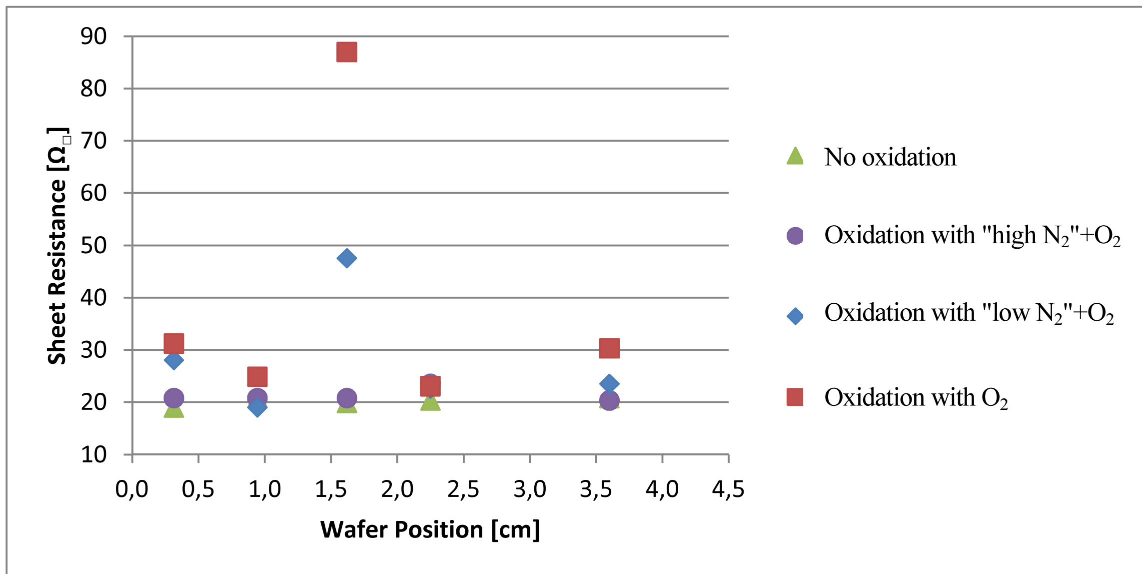

Graph 40 - R_{sheet} measured along a vertical line that crosses the wafer center for different doping processes tested.

5.10.3. Discussion

From the visual inspection the darkening of the wafers surface coloration can be associated with a stronger oxidation as it only appeared when the N_2 was decreased and the O_2 increased. On the other hand, it is possible that the process with a N_2 flux of 10.5 slm during the oxidation step resulted in an insufficient oxidation.

The R_{sheet} measurements are in agreement with the visual inspection, as no changes were observed when the oxidation step was applied. A probable cause is that the O_2 is too diluted, which can be even more relevant as an already thick oxide is formed during the predeposition step.

For the remaining processes it can be observed that reducing the N_2 and increasing the O_2 leads to an increase in R_{sheet}. This can be both due to the oxidation of a layer with a high concentration of boron or due to the segregation of boron to the oxide. However, this increase in R_{sheet} is highly inhomogeneous as a significantly increase can be observed in the wafers center, where no BRL was found, while the border regions showed only a slight increase. This might be explained by the presence of a BRL between the wafer's surface and a BSG layer, that is thicker in the borders than at the wafer’s center, which would imply that near the borders the O_2 molecules have to cross a thicker region, slowing down the oxidation process in that region.

This does not necessarily imply that the oxidation step in itself is inhomogeneous, as the predeposition step results in thicker oxides in the borders, which surely also affects the BRL

thickness. Therefore, a possible conclusion is that in order to apply an in-situ thermal oxidation a homogeneous predeposition step must be first implemented.

5.11. Predeposition + Chemical Oxidation Process

A doped wafer obtained using the processes whose parameters are presented in the following table, was tested for BRL removal with a weak chemical etch by dipping in an "etch-back" solution.

Parameters	Value
Furnace tube temperature [ºC]	1000
Bubbler temperature [ºC]	32
Number of Wafers/Barriers	5/4
Wafer spacing [mm]	6.5
Predeposition Time [min]	30
N_2/ BBr_3-N_2/O_2 flow [slm]	3.53/0.08/0.16
BBr_3 content [%]	0.25

Table 14 - Doping process conditions

5.11.1. Visual Inspection

Photographs were taken after the doping process and the chemical etching (Figure 31). In the first case even after a long dip in a weak chemical etch it was not possible to remove the BRL entirely as only the upper left and right borders showed an hydrophobic behavior after the etch. Additionally, these regions are clearly visible in the wafer surface.

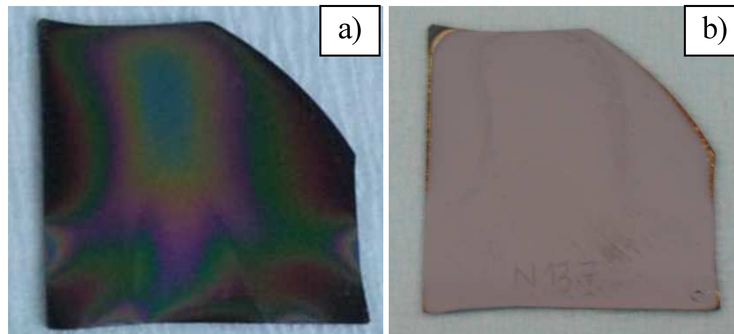

Figure 31 - Surface coloration after the doping process (left) and an etch-back (right)

5.11.2. Discussion

The wafers surface behavior when in contact with water showed that for certain regions the chemical etch is ineffective as only the upper lateral borders of the surface had the BRL removed. This fact helps to sustain the idea that the BRL had a non-uniform thickness along the wafer area and can indicate that the non-homogeneity obtained in the thermal oxidation experiment should be due to the inhomogeneous oxide that is formed in the predeposition step and not due to the oxidation step. Additionally, this experiment settles the BRL thickness non-uniformity as a possible reason for the ineffective BRL removal after an in-situ thermal oxidation.

5.12. Oxide Thickness Visual Assessment Method Validation

Oxide thickness measured with spectroscopic ellipsometry from different processes and different regions of the wafer (center, top and bottom) were compared with the thicknesses assessed with visual observation and comparison to an oxide thickness color chart. These comparisons are presented in Graph 17, where the correlation between both measurements is clearly verified, as a correlation factor of 0.97 was obtained.

While Kessler et al. [48] reported a constant overestimation no bigger than 20% when comparing visually assessed oxide thicknesses with SEM measurements, for the present work both underestimations and overestimations not bigger 13% were found.

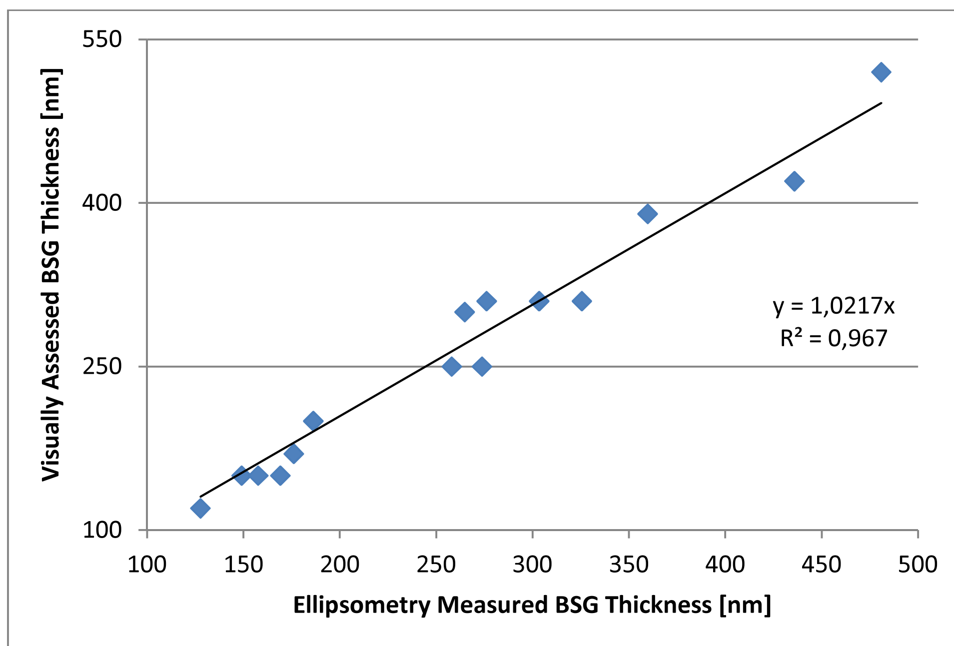

Graph 41 - Comparison between BSG thicknesses visually assessed and measured with spectroscopic ellipsometry

6. Conclusions and Future Work Lines

The present work had the objective of developing a boron emitter fabrication process for n-type Si wafers, as it is considered one of the main challenges in the development and deployment of high efficiency solar cells based in this material.

Several parameters respective to the doping process were studied. First of all, it was observed that the bubbler temperature is a crucial parameter as it is strongly related to the quantity of boron carried by the N_2 that goes through the BBr_3 liquid source and therefore in the doping environment inside the furnace tube. While a doping process with a bubbler temperature of 4 ºC showed no signs of doping (nor oxide coloration nor significant boron incorporation),by only increasing the temperature to 20 ºC, certain regions then showed not only some coloration but also Rsheet values as low as 72 Ω/□. It is however important to bear in mind that, for safety reasons, the bubbler should be kept at temperatures under 40 ºC, in accordance to Schumacher's, the bubbler manufacturer, indications.

In a different experiment, three processes were tested where two of them had a bubbler temperature of 25 ºC and the third had 26 ºC, while maintaining all other parameters, in order to evaluate the process repeatability and its sensibility to this parameter. While the two identical processes only showed slight differences in the dopant incorporation, the increase of 1 ºC resulted in a clear increase of the doping level. In all three cases a considerably heavier doping and thicker oxides, followed by the presence of a BRL, were found at the wafers borders. Possible reasons for this are: the use of wafers of small dimension, when compared to the furnace tube; the spacing between wafers and the doping gas flow dynamics which might favor a more efficient contamination of the wafer borders than its center.

Increasing the N_2 gas flow led to a lighter doping and the formation of thinner oxides. This result was quite predictable as the doping environment becomes more diluted. However, what was not foreseen was that this result was mostly verified at the wafer's lower region, which might also be explained by the wafers dimension.

On the other hand, it was verified that in respect to the N_2 carrying BBr_3, below a certain gas flow the doping process shows to be ineffective and this evolution is quit quite visible as for low N_2 carrier gas flows a less dense B_2O_3 cloud was observed inside the furnace. The doping gas quantity can be adjusted either by control of the N_2 carrier gas flow or of the bubbler temperature. However, considering that it is advised to work the bubbler at temperatures under 40˚C an adequate control of the N_2 flow is required.

The results obtained in the present work seem to be in agreement with the idea that for BSG thicknesses over a certain value, the BSG starts acquiring a significant inhomogeneity. When the duration of a deposition process was reduced from 30 to 15 minutes, a more homogeneous oxide was formed and a BRL was already present. Additionally, in the border regions no change in the Rsheet was verified which could possibly indicate that the boron has already reached its solid solubility limit inside the Si substrate.

Therefore, it is quite possible that shorter predeposition steps might result in a more homogenous oxide growth and should thus be tested. As an alternative, the furnace temperature can be reduced, resulting in a wider range of process durations to be tested and, consequently, a potently higher control in respect to the oxide growth.

When the removal of the BRL was tried through an in-situ thermal oxidation, only a partial removal was achieved. A considerable R_{sheet} increase in the regions stripped of its BRL was observed, possibly due to the boron segregating into the oxide. The oxidation conditions were excluded as possible causes to explain why the BRL removal was only partial as a weak chemical etching, preceded by a HF dip for oxide removal, also resulted in a partial removal. These results combined with the fact that, in almost all experiments an inhomogeneous oxide was formed during the predeposition step, led to the conclusion that the development of a predeposition step that allows the formation of a homogenous oxide, is of crucial importance for the success of doping process as it conditions all the following steps.

The spacing between the wafers in the boat structure showed to have a significant impact in the resulting doping level as it was observed that the closer the wafers are from each other, the thinner and more homogeneous the oxides formed are. When the spacing was varied from 9 to 4 mm, no BRL was formed in the central region of the wafer and a lower doping level was obtained, as consequence the sheet resistance changed from 20 to 120 Ω/□. This type of emitter might be of interest if a light doping is intended, adding the advantage that no BRL is formed.. However, this was only achievable due to the use of overdoped wafers as barriers.

These barriers started out as regular undoped wafers placed in the start and end of the boat structure but after several experiments, these barriers started to accumulate B_2O_3 and gained a very dark coloration. These overdoped wafers proved to be efficient as secondary dopants sources on single doping processes.

However, when batch processes, with several wafers, were tested, the overdoped barriers showed to have a very local effect, as only the nearest wafers showed thicker oxide layers and higher doping levels, which led to their replacement by undoped barriers. However while it was possible to establish a doping process for a batch of wafers, using a wide wafer spacing, when using narrow wafer spacing's the process proved to be strongly dependent of the use the overdoped wafers and therefore was not viable as a batch process. It is therefore considered that a batch consisting in alternating pairs of undoped wafer-overdoped barrier should be tested in the future.

Finally, the visual assessment of the BSG thickness proposed by the literature was validated, as a comparison between those measurements and ellipsometry ones led to a correlation factor of 0.97 with a relative error of less than 13%. Meaning that a photography made in a perpendicular position in respect to the wafer surface avoids the need of specific methods like spectroscopic ellipsometry or SEM.

As guidelines on how to continue the present work in order to achieve a fully working and optimized BBr_3 doping process for high efficiency n-type solar cells, the following topics are proposed as future lines of work:

- achieve a BBr_3 doping process which results in an homogeneous BSG and R_{sheet};

- measure doping profiles as a complement to the R_{sheet} measurements and in order to better study the BRL and evaluate possible boron segregation;

- completely remove the BRL with either a chemical or a thermal oxidation;

- evaluate the impact of the parameters studied in this work but now in respect to the wafer's gettering and bulk lifetime.

7. Attachments

7.1. Attachment 1: Color Char for Thermally Grown SiO2

Film Thickness (Å)	Color of Film (those shown are only indicative)
500	Tan
700	Brown
1000	dark violet to red violet
1200	royal blue
1500	light blue to metallic blue
1700	metallic to very light yellow-green
2000	light gold or yellow - slightly metallic
2200	gold with slight yellow-orange
2500	orange to melon
2700	red-violet
3000	blue to violet-blue
3100	Blue
3200	blue to blue-green
3400	light green
3500	green to yellow-green
3600	yellow-green
3700	green-yellow
3900	Yellow
4100	light orange
4200	carnation pink
4400	violet-red
4600	red-violet
4700	Violet
4800	blue-violet
4900	Blue
5000	blue-green
5200	Green
5400	yellow-green
5600	green-yellow
5700	yellow to “yellowish” (at times appears light gray or metallic)
5800	light orange or yellow to pink
6000	carnation pink

6300	violet-red
6800	“bluish” (appears between violet-red and blue-green - overall looks grayish)
7200	blue-green to green
7700	“yellowish”
8000	Orange
8200	Salmon
8500	dull light red-violet
8600	Violet
8700	blue-violet
8900	Blue
9200	blue-green
9500	dull yellow-green

8. Bibliography

[1] U. Gangopadhyay, S. Das, S. Jana and P. Ghosh, "Feasibility of n-type crystalline silicon wafer for fabricating Industrial Silicon Solar Cell with significant acceptable efficiency in near future," 2014.

[2] J. Cotter, J. Guo, P. Cousins, M. Abbott, F. Chen and K. Fisher, "P-Type Versus n-Type Silicon Wafers: Prospects for High-Efficiency Commercial Silicon Solar Cells," 2006.

[3] J. Schimdt and R. Hezel, "Light-induced degradation in Cz Silicon solar cells: fundamental understanding and strategies for its avoidance," 2002.

[4] B. Sopori, P. Basnyat, S. Shet, V. Mehta, J. Binns and J. Appel, "Understanding Light-Induced Degradation of c-Si solar cells," 2012.

[5] S. W. Glunz, S. Rein, W. Warta, J. Knobloch and W. Wttling, "On the degradation of Cz-silicon solar cells," 1998.

[6] D. M. Chapin, C. S. Fuller and G. L. Pearson, "A New Silicon p-n Junction Photocell for Converting Solar Radiation into Electrical Power," 1954.

[7] V. Mihailetchi, Y. Komatsu and L. Geerligs, "Nitric acid pretreatment for the passivation of boron emitters for n-type base silicon solar cells," 2008.

[8] K. Smith, H. Gummel, J. Bode, D. Cuttriss, R. Nielsen and W. Rosenzweig, "The solar cells and their mounting," 1963.

[9] D. MacDonald, "The emergence of n-type silicon for solar cell manufacture," 2012.

[10] H. Kerp, S. Kim, R. Lago, F. Recart, I. Freire, L. Pérez and K. Albertsen, "Development of Screen printable Contacts for P+ Emitters in Bifacial Solar Cells," 2006.

[11] J. Silva, M. Gauthier, C. Boulord, C. Oliver, A. Kaminski, B. Semmache and M. Lemiti, "Progress in the metallisation of n-type multicrystalline silicon solar cells," 2011.

[12] A. Edler, V. Mihailetchi and C. Comparotto, "Metal induced losses in bifacial n-type silicon solar cells: Metal induced losses in bifacial n-type silicon solar cells:," 2014.

[13] R. Bonilla and P. Wilshaw, "A technique for field effect surface passivation for silicon solar cells," 2014.

[14] J. Libal, R. Petres, T. Buck, R. Kopecek, G. Hahn, R. Ferre, M. Vetter, I. Martín, K. Wambach, I. Röver and P. Fath, "N-type Multicrystalline Silicon Solar Cells: BBr3-Diffusion and Passivation of p+-Diffused Silicon Surfaces," 2005.

[15] J. Benick, B. Hoex, O. Schultz and S. Glunz, "Surface Passivation of Boron Diffused Emitters for High-Efficiency Solar Cells," 2008.

[16] B. Hoex, J. Schmidt, R. Bock, P. Altermatt, M. van de Sanden and W. Kessels, "Excellent passivation of highly doped p-type Si surfaces by the negative-charge-dielectric Al2O3," 2007.

[17] J. Benick, O. Schultz, J. Schön and S. Glunz, "Passivation of Boron Emitters by Local Overcompensation With Phosphorus," 2008.

[18] S. Phang and D. Macdonald, "Effect of Boron Codoping and Phosphorus Concentration on Phosphorus Diffusion Gettering," 2014.

[19] P. Altermatt, H. Plagwitz, R. Bock, J. Schmidt, R. Brendel, M. Kerr and A. Cuevas, "The surface recombination velocity at boron-doped emitters: comparison between various passivation techniques," 2006.

[20] F. Chen, T. Li and J. Cotter, "PECVD Silicon Nitride Surface Passivation For High-Efficiency n-type Silicon Solar Cells," 2006.

[21] F. Chen, I. Romijn, A. Weeber, J. Tan, B. Hallam and J. Cotter, "Relation Between PECVD Silicon Nitride Film Composition and Surface and Edge Passivation," 2007.

[22] K. Ryu, A. Upadhyaya, H. Song, C. Choi, A. Rohatgi and Y. Ok, "Chemical etching of boron-rich layer and its impact on high efficiency n-type silicon solar cells," 2012.

[23] S. Duttagupta, F. Ma, B. Hoex and A. Aberle, "Excellent surface passivation of heavily doped p+- silicon by low-temperature plasma-deposited SiOx/SiNy dielectric stacks with optimised antireflective performance for solar cell application," 2014.

[24] T. Joge, I. Araki, T. Uematsu, T. Warabisako, N. Hiroshi and K. Matsukuma, "Low-Temperature Boron Gettering for Improving the Carrier Lifetime in Fe-Contaminated Bifacial Silicon Solar Cells with n+pp+ Back-Surface-Field Structure," 2003.

[25] T. Terakawa, D. Wang and H. Nakashima, " (2006). Role of Heavily B-doped Layer on Low-Temperature Fe Gettering in Bifacial Si Solar Cell Fabrication.," 2006.

[26] S. Tobe, Y. Hayamizu and Y. Kitagawara, "Equilibrium constant of segregation-induced Fe gettered by heavy boron doping in Si," 1998.

[27] S. Phang and D. Macdonald, "Boron, phosphorus and aluminum gettering of iron in crystalline silicon: experiments and modelling," 2010.

[28] T. Weber, C. Zechner, D. Macdonald and P. Altermatt, "Numerical Simulation of Gettering and Recombination," 2006.

[29] C. Reichel, M. Bivour, F. Granek, M. Hermle and S. Glunz, "Improved diffusion profiles in back-contacted back-junction Si solar cells with an overcompensated boron-doped emitter," 2011.

[30] R. Gereth and G. Schwuttke, "Localized enhanced diffusion in npn silicon," 1966.

[31] S. Hu and T. H. Yeh, "Approximate theory of emitter-push effect," 1969.

[32] J. Lawrence, "Cooperative diffusion effect," 1966.

[33] A. Slade, Boron Tribromide Sourced Boron Diffusions for Silicon Solar Cells, 2003.

[34] P. Lölgen, C. Leguijt, J. Eikelboom and R. Steeman, "Aluminium Back-Surface Fields Doping Profiles with Surface Recombination Velocities Below 200 cm/s," 1993.

[35] G. Vick and K. Whittle, "Solid solubility and diffusion coefficients of boron in silicon," 1969.

[36] V. Popovich, M. van Maris, M. Janssen, I. Bennett and M. Richardson, "Understanding the Properties of Silicon Solar Cells Aluminium Contact Layers and Its Effect on Mechanical Stability," 2013.

[37] A. Kaminski, B. Vandelle, A. Fave, J. Boyeaux, L. Q. Ma, R. Monna, D. Sarti and A. Laugier, "Aluminium BSF in silicon solar cells," 2002.

[38] T. van Amstel, V. Popovich, P. de Jong and I. Romijn, "Modeling Mechanical Aspects of the Aspire Cell," 2008.

[39] M. Köntges, I. Kunze, S. Kajari-Schröder, X. Breitenmoser and B. Bjørneklett, "The risk of power loss in crystalline silicon based photovoltaic modules due to micro-cracks," 2011.

[40] M. M. Hilali, J. M. Gee and P. Hacke, "Bow in screen-printed back-contact industrial silicon solar cells," 2007.

[41] F. Huster, "Investigation of the Alloying Process of Screen Printing Aluminum Pastes for the BSF Formation on Silicon Solar Cells," 2005.

[42] F. Huster, "Aluminum-back surface field: bow investigation and elimination," 2005.

[43] S. Kim, S. Sridharan and C. a. S. A. Khadilkar, "Aluminum paste (Lead-Free/Low Bow) for thin wafers," 2004.

[44] R. Kopecek, T. Buck, A. Kränzl, J. Libal, K. Peter, A. Schneider, P. Sánchez-Friera, I. Röver, K. Wambach, E. Wefringhaus and P. Fath, "Module Interconnection With Alternate p- and n- type Si Solar cells.," 2006.

[45] A. Moehlecke, F. Febras and I. Zanesco, "Electrical performance analysis of PV modules with bifacial silicon," 2013.

[46] K. Wijekoon, H. Mungekar, M. Stewart, P. Kumar, J. Franklin, M. Agrawal, K. Rapolu, F. Yan, Y. Zheng, A. Chan, M. Vellaikal, X. Lu, D. Kochhar, L. Zhang, D. Tanner, V. Dabeer and H. Ponnekanti, "Development of high eficiency mono-crystalline Silicon Solar Cells: Optimization of rear local contacts formation on dielectrically passivated surfaces," 2012.

[47] Air Products and Chemicals, Inc., "Process guidelines for using boron tribromide (BBr3)".

[48] M. Kessler, T. Ohrdes, B. Wolpensinger, R. Bock and N. Harder, "Characterization and implications of the boron rich layer resulting from open-tube liquid source BBr3 boron diffusion processes," 2009.

[49] C. Zhou, Y. Tang, W. Wang, S. Zhou, L. Zhao, H. Li and H. Diao, "Preparation of p+-layers using water vapor as oxidant in BBr3 diffusion for silicon solar cells," 2013.

[50] A. Das, K. D.S., K. Nakayashiki, B. Rounsaville, V. Meemongkolkiat and A. Rohatgi, "Boron diffusion with boric acid for high efficiency silicon solar cells," 2010.

[51] R. F. Lever and H. M. Demsky, "Water vapor as an oxidant in BBr3 open-tube silicon diffusion systems," 1974.

[52] J. Zuckerman, Inorganic reactions and methods: Formation of ceramics, Volume 18, 2007.

[53] E. Arai, H. Nakamura and Y. Terunuma, "Interface reactions of B2O3-Si system and boron diffusion into silicon," 1973.

[54] E. Dominguez, E. Lora-Tamayo, B. Blanchard and J. Bellanato, "Analytic Study of the Si-B Phase When B2O3 is Diffused in Si," 1978.

[55] G. Pignatel and G. Queirolo, "Further Insight on Boron Diffusion in Silicon Obtained with Auger Electron Spectroscopy," 1979.

[56] T. Aselage, "The coexistence of silicon borides with boron-saturated silicon: Metastability of SiB3," 1997.

[57] J. Rapp and N. Nofziger, "The effect of oxygen on boron silicide formation at 950°C. Techramics, Ltd., Production Note 103.".

[58] C. Kim, S. Park, Y. Kim, H. Park, S. Kim and H. Kim, "Properties of boron-rich layer formed by boron diffusion in n-type silicon," 2014.

[59] S. Prussin, "Generation and distribution of dislocations by solute diffusion," 1961.

[60] X. Ning, "Distribution of residual stress in boron doped p+ silicon films.," 1996.

[61] P. Cousins and J. Cotter, "The influence of diffusion-induced dislocations on high efficiency silicon solar cells," 2006.

[62] Y. Schiele, S. Fahr, S. Joos, B. Hahn and B. Terheiden, "Study on Boron emitter formation by BBR3 diffusion for n-type Si solar cell applications," 2013.

[63] S. Ghandi, "VLSI Fabrication Principles: Silicon and Gallium Arsenide," 1994.

[64] K. Busen, W. FitzGibbons and W. Tsang, "Ellipsometric Investigations of Boron-Rich Layers on Silicon," 1968.

[65] T. Buck, R. Kopecek, J. Libal, R. Petres, K. Peter, I. Röver, K. Wambach, L. Geerligs, E. Wefringhaus and P. Fath, "Large area screen printed n-type mc-Si solar cells with B-emitter: efficiencies close to 15% and innovative module interconnection," 2006.

[66] E. O. Sveinbjörnsson and O. Engström, "Phosphorus diffusion gettering of gold in silicon: The reversibility of the gettering process," 1993.

[67] B. Cui, *Material from the course "NE 343: Microfabrication and thin film technology", University of Waterloo,* lective year 2013/14.

[68] Schumacher, "Boron tribromide as a p-type silicon dopant," 2003.

[69] "American Laboratory," [Online]. Available: http://www.americanlaboratory.com/914-Application-Notes/138874-Spectroscopic-Ellipsometry-Characterization-of-Thin-Films-Used-in-the-Food-Packaging-Industry/.

[70] D. Schroder, "Semiconductor material and device characterization," 1998.

[71] A. Shimamoto, K. Yamashita, H. Inoue, S. Yang, M. Iwata and N. Ike, "A Nondestructive Evaluation Method: Measuring the Fixed Strength of Spot-Welded Joint Points by Surface Electrical Resistivity," 2013.

[72] R. Hull, "Properties of Crystalline Silicon," 1999.

[73] "PV Education," [Online]. Available: http://pveducation.org/pvcdrom.

[74] H. Simchi, "Using variance analysis to set up a BBr3 pre-deposition process".

[75] H. Shimidzi, "Using variance analysis to set up a BBr3 pre-deposition process".